One-Dimensional Metal-Oxide Nanostructures: Recent Developments in Synthesis, Characterization, and Applications

*Rupesh S. Devan, Ranjit A. Patil, Jin-Han Lin, and Yuan-Ron Ma**

1D metal-oxide nanostructures have attracted much attention because metal oxides are the most fascinating functional materials. The 1D morphologies can easily enhance the unique properties of the metal-oxide nanostructures, which make them suitable for a wide variety of applications, including gas sensors, electrochromic devices, light-emitting diodes, field emitters, supercapacitors, nanoelectronics, and nanogenerators. Therefore, much effort has been made to synthesize and characterize 1D metal-oxide nanostructures in the forms of nanorods, nanowires, nanotubes, nanobelts, etc. Various physical and chemical deposition techniques and growth mechanisms are exploited and developed to control the morphology, identical shape, uniform size, perfect crystalline structure, defects, and homogenous stoichiometry of the 1D metal-oxide nanostructures. Here a comprehensive review of recent developments in novel synthesis, exceptional characteristics, and prominent applications of one-dimensional nanostructures of tungsten oxides, molybdenum oxides, tantalum oxides, vanadium oxides, niobium oxides, titanium oxides, nickel oxides, zinc oxides, bismuth oxides, and tin oxides is provided.

1. Introduction

Over the past few decades, researchers have become increasingly engrossed in the study of metal-oxides. Metal-oxides are ionic compounds that are made up of positive metallic and negative oxygen ions. The electrostatic interactions between the positive metallic and negative oxygen ions result in firm and solid ionic bonds. The s-shells of metal-oxides are completely filled, so that most of the metal-oxides have good thermal and chemical stability.[1,2] However, their d-shells may be not completely filled, giving them a variety of unique properties that make them potentially of great use in electronic devices. These unique properties include wide bandgaps,[3,4] high dielectric constants,[5–7] reactive electronic transitions,[8,9] and good electrical,[10,11] optical,[12,13] and electrochromic characteristics,[14,15] as well as superconductivity.[16,17] Therefore, metal-oxides are considered to be some of the most fascinating functional materials and have been widely exploited in various technological applications.

Currently, the rapid development of nanoscience and nanotechnology has greatly motivated the scientific community and industry to explore new features of both typical and novel materials at the nanoscale level. Materials at a nanoscale level are known as the nanomaterials. In general nanomaterials can be categorized as having three different morphologies or nanostructures: 0D, 1D, and 2D nanostructures. It should be noted that when the size and dimensionality are reduced, the electronic structures of the nanomaterials are different from those of the bulk material.[18,19] These differences in the electronic structures can cause a variety of changes in both chemical[20] and physical properties.[21] Hence, nanomaterials with at least one dimension between 1 and 100 nm are treated as new materials. Among all nanomaterials, 1D nanostructures are more applicable to nanoelectronics and nanodevices because all of them have a 1D morphology. Namely, the widths and thickess of the 1D nanostructures are confined to the nanoscale range between 1 and 100 nm, but the lengths can be a few millimeters long or more. The millimeter length scale allows the 1D nanostructures to contact the macroscopic world for many physical measurements. Therefore, the 1D morphology is more suitable for the fabrication of building blocks,[22–24] making electrical measurement with two terminals easier.[25,26]

Enormous efforts have so far been made to synthesize and characterize 1D metal-oxide nanostructures in the forms of rods,[27–31] wires,[32–34] needles,[35,36] tubes,[37,38] belts,[39–41] hooks,[42] cables (i.e., coaxial wires),[43,44] ribbons,[45,46] fibers,[47] tips,[48] helices (or spirals),[49,50] and zigzags.[50] The 1D forms can enhance the unique properties of the material, making them suitable for a wide variety of applications such as biosensors,[51,52] gas sensors,[53–55] smart windows,[56–58] solar cells,[59–63] supercapacitors,[64,65] photodetectors,[66–68] light-emitting diodes,[69] field emissions,[70,71] and field-effect transistors.[72–75] These 1D metal-oxide nanostructures have triggered a lot of excitement and allowed breakthrough achievements in all areas of electronics. However, the 1D metal-oxide nanostructures do still have drawbacks. For example, in comparison with the bulk materials, the low dimension and small size make the melting

Dr. R. S. Devan, R. A. Patil, J.-H. Lin, Prof. Y.-R. Ma
Department of Physics
National Dong Hwa University
Hualien 97401, Taiwan, Republic of China
E-mail: ronma@mail.ndhu.edu.tw

DOI: 10.1002/adfm.201201008

point lower but the resistivity higher, so the thermal and chemical stability of the 1D metal-oxide nanostructures may be weakened. In other words, overheating caused by the passage of high currents through the nanodevices or nanoelectronics can easily burn the 1D metal-oxide nanostructures causing them to break. Ideally the 1D metal-oxide nanostructures used for the nanodevices or nanoelectronics are expected to be identical in shape, uniform in size, perfect in crystalline structure, and easy in taking apart, and have no morphological defects and a consistent chemical composition. However, control of the morphology, shape, size, crystalline structure, and chemical composition of the 1D metal-oxide nanostructures remains a challenge in the development of 1D controllable synthesis methods.

A number of physical and chemical methods have been use to achieve the goals of identical shape, uniform size, perfect crystals, no defects, and homogenous stoichiometry in the synthesis of ideal 1D metal-oxide nanostructures. In Section 2, we introduce some of the synthesis techniques for the production of various 1D metal-oxide nanostructures, covering the theoretical and experimental aspects of recent developments, such as 1D nanostructure design, processing, modeling, and fabrication. In Section 3, we present several growth mechanisms for the growth of 1D metal-oxide nanostructures. Since such 1D nanostructures possess a highly anisotropic morphology, they preferentially grow along one particular crystalline direction to form the 1D morphology. This anisotropic growth is strongly dominated by internal and external stresses, such as easy-growth lattice-planes and template confinement, respectively. In Section 4, we provide a comprehensive review of a variety of 1D metal-oxide nanostructures, including tungsten oxides, molybdenum oxides, tantalum oxides, vanadium oxides, niobium oxides, titanium oxides, nickel oxides, zinc oxides, bismuth oxides, tin oxides, etc. These 1D metal-oxide nanostructures are characterized using various microscopic analytic techniques. The microscopic results demonstrate that the physical, chemical, electronic, optical, and magnetic properties are unique and different from the bulk materials. In Section 5, we introduce the reader to recent applications that take advantage of 1D metal-oxide nanostructures. The applications include gas sensors, electrochromic devices, LEDs, field emitters, supercapacitors, nanoelectronics, and nanogenerators. In Section 6, some concluding remarks and perspectives on the 1D metal-oxides nanostructure are offered. We hope this article can provide the readers with snapshots of the recent development and future challenges.

2. Synthesis Techniques

A variety of synthesis techniques have been developed to synthesize 1D metal-oxide nanostructures. These synthesis techniques can be categorized into two methods: i) direct physical deposition techniques and ii) direct chemical deposition techniques. Each method has its own advantages and strategy for the synthesis of 1D metal-oxide nanostructures. For example, physical deposition methods, such as lithographic techniques, are good for the ''top-down'' approach, while chemical deposition methods are usually used for the "bottom-up" approach. In this section, we briefly describe various physical and chemical deposition techniques for 1D metal-oxide nanostructures.

Rupesh Devan received his PhD (2007) in Physics from Shivaji University, Kolhapur, India. In 2007, he joined Prof. Yuan-Ron Ma's group as a postdoctoral fellow at National Dong Hwa University, Taiwan. His research interests include fabrication and characterization of 1D metal-oxide nanostructures and applications in optoelectronics and electrochromism. He also works on magnetic and magnetoelectric composite materials.

Yuan-Ron Ma received his PhD in Physics from the University of Nottingham, UK in 1998 and joined the Academia Sinica, Taiwan for a postdoctoral fellowship in the same year. Currently, he is a Professor and an excellent research fellow at the National Dong Hwa University, Taiwan. His research interests include nanosciences, nanotechnology, materials sciences, and surface sciences and his current work concentrates on the synthesis, characterization, and applications of various metal and metal-oxide nanostructures.

2.1. Direct Physical Deposition Techniques

The direct physical deposition techniques include thermal evaporation, molecular beam epitaxial, sputtering, laser ablation, confinement growth, lithography, etc. When atoms and molecules of the metal-oxides or compounds grow in a preferential direction with or without external physical forces, the 1D morphology is naturally formed. Although the as-synthesized nanostructures are metal-oxides or compounds, the physical deposition techniques basically involve no chemical reactions during the synthesis of 1D metal-oxide nanostructures.

2.1.1. Physical Vapor Deposition (PVD)

Thermal evaporation, namely physical vapor deposition (PVD), is one of the most important techniques. A tube furnace,[39,76,77] as shown in **Figure 1**, is typically used for thermal evaporation. Massive 1D metal-oxide nanobelts can be synthesized in tube furnaces. Bulk metal-oxides are placed in the tube furnace and annealed at high temperatures in high vacuum environments or ambient inert gases. The heat causes the atoms or molecules to escape from the surface of the bulk metal-oxide material. That is to say, the surface atoms or molecules sublimate into metal-oxide

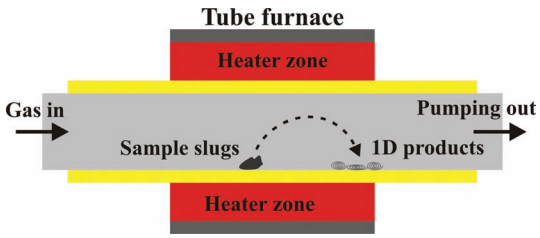

Figure 1. Schematic diagram of tube furnace for synthesis of 1D nanostructures.

vapor. When the metal-oxide vapor encounters a substrate, it condenses into 1D metal-oxide nanostructures. Molecular beam epitaxy, sputtering, and laser ablation are also types of PVD techniques. The high-energy electrons and photons of the molecular beam epitaxial and laser ablation techniques cause the surface atoms or molecules of the metal-oxide to sublimate in their gas phases, while with the sputtering techniques the surface of the bulk metal-oxide is bombarded with argon ions to generate small clusters. Sputtering[78] and laser ablation[79] techniques can be used to synthesize colossal 1D metal-oxide nanostructures. However, the molecular beam epitaxial technique[80,81] is mostly used to synthesize 1D nanostructures of III-V compounds, not metal-oxides. The PVD techniques mainly involve vapor-solid growth without metallic catalysts. The growth mechanism of the PVD will be discussed in Section 3.

2.1.2. Confinement Growth

Confinement growth includes template-based and capping-reagent synthesis. Template-based synthesis has become the most common technique for the fabrication of 1D nanostructures. In comparison with the template free synthesis, template-based synthesis offers an easy way to fabricate metal-oxides into 1D nanostructures. Various template-based syntheses models[82–84] have been reviewed for 1D metal-oxide nanostructures. Templates are used to assist in the formation of 1D nanostructures in nanomaterials because the templates can confine nanomaterial growth in the 1D freedom nanoscale space. For example, porous anodic aluminum oxide (AAO) plates form a very good template to synthesize various 1D nanostructures of metal and metal-oxides.[82–86] The scanning electron microscopy (SEM) images in **Figure 2**a,b show the top and cross-sectional views of a porous AAO template, The AAO template provides straight 1D long-distance porous channels, as displayed in the schematic diagram in Figure 2c. The channels can be a few hundred nanometers long and less than 100 nm in diameter. The straight porous channels only allow the 1D nanostructures to grow vertically and upwards. The walls constrain the horizontal growth in the other two dimensions. The arrows in Figure 2c indicate the growth directions of the 1D nanostructures. It is not only porous channels that can be used as templates to confine 1D nanomaterial growth, capping-reagents,[87] and viruses[88] can also be used in this way. The schematic diagram in Figure 2d shows how the capping reagent constrains the growth of 1D nanostructures. Capping-reagents and viruses possess self-assembly properties and they can accomplish the purpose of confinement growth.

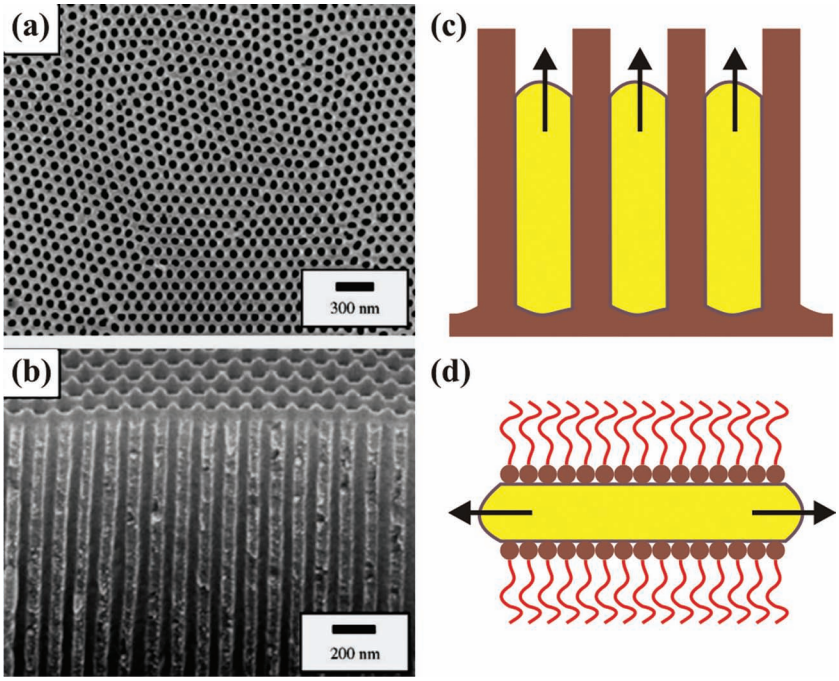

Figure 2. a,b) SEM images showing the top and cross-sectional views of an AAO template. Reproduced with permission.[85] Copyright 2006, Elsevier. The AAO template has straight 1D porous channels: c,d) 1D nanostructures constrained to grow in the straight porous channels and a capping reagent. The arrows indicate the growth directions of the 1D nanostructures.

2.1.3. Lithographic Techniques

The lithographic techniques include electron-beam lithography, focused-ion-beam lithography, and dip-pen nanolithography. These techniques have made great contributions to the growth of 1D nanostructures, but the high cost and low throughput for large-scale 1D nanostructures are still challenges. The lithographic techniques have inherent advantages for the synthesis of 1D nanostructures, such as making possible the fabrication of large-scale and well-aligned arrays, and are therefore exploited in order to fabricate various designed-geometry patterns on solid substrates. **Figure 3**a shows a schematic representation of the lithographic processes for fabricating various designed-geometry patterns. For details of the parameters of the lithographic processes see ref. [89]. Normally the designed geometric patterns can possess complicated micro- or nanostructures, as shown in Figure 3b,c. Figure 3b,c show SEM images of the designed-geometry lithographic patterns (top and side views). The lithographic patterns can be used as templates for growth of the 1D nanostructures in the designed geometry. For example, 1D nanostructures can grow on preferential sites, such as shadow sites,[89,90] V-grooves,[89,90] cleaved edges,[91] and step edges[92] during the PVD process, especially during glancing angle deposition (GLAD).[50] The GLAD technique will be described in

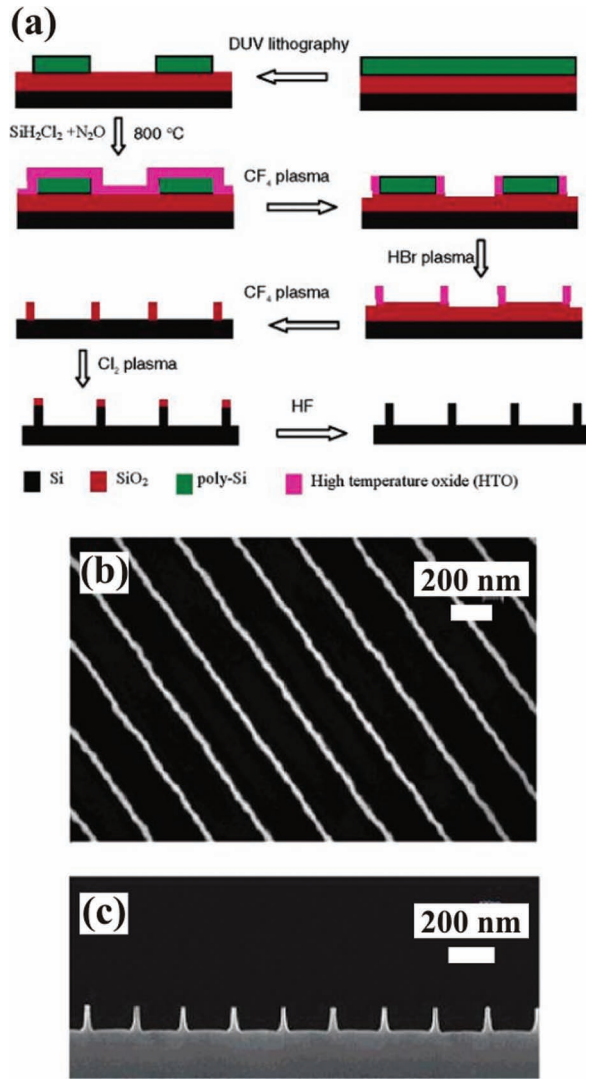

Figure 3. a) Schematic diagram of the lithographic processes. All details of the lithographic processes have been described in ref. [89]. b,c) SEM images showing the top and side views of the designed geometric lithographic patterns. Reproduced with permission.[89] Copyright 2005, American Chemical Society.

Section 2.1.4. The lithographic techniques are a type of top-down approach that is widely used in the semiconductor industry at the present time. They can produce 1D nanostructures with very uniform bodies. However, the physical limits of the top-down approaches will soon be reached. The physical limits are related to the electron transport when the sizes of the 1D metal nanostructures are smaller than the mean free paths of the electrons. The electron transport in very small 1D metal nanostructures will be different from the electron drift in the bulk material, which has also motivated global efforts to seek new strategies to meet the demands for increased computational performance speed.

2.1.4. Glancing Angle Deposition

Glancing angle deposition (GLAD) is one of the direct physical deposition techniques that can be used to fabricate large-area ordered arrays of 1D metal-oxide nanostructures, especially nanohelices and nanozigzags.[50] The schematic diagram in **Figure 4**a shows the GLAD setup.[93] A flowing vapor flux of atoms or molecules is incident to the substrate at an angle α with respect to the surface's normal direction in a vacuum. Some island seeds form first and are randomly distributed on the substrate surface, as shown in the upper panel of Figure 4b.[94] As the vapor flux continues to impinge on the substrate surfaces, the island seeds become 1D nanostructures, as shown in the lower panel of Figure 4b. The GLAD technique is utilized in order to control the incident angle, namely by manipulating the shadow edges or the tilt of the 1D nanostructures. When the substrate is rotated around the surface's normal direction, the morphology of the 1D nanostructures will be dramatically changed.[50,93,94] This is because the growth directions of the 1D nanostructures are strongly dependant on the incidence of

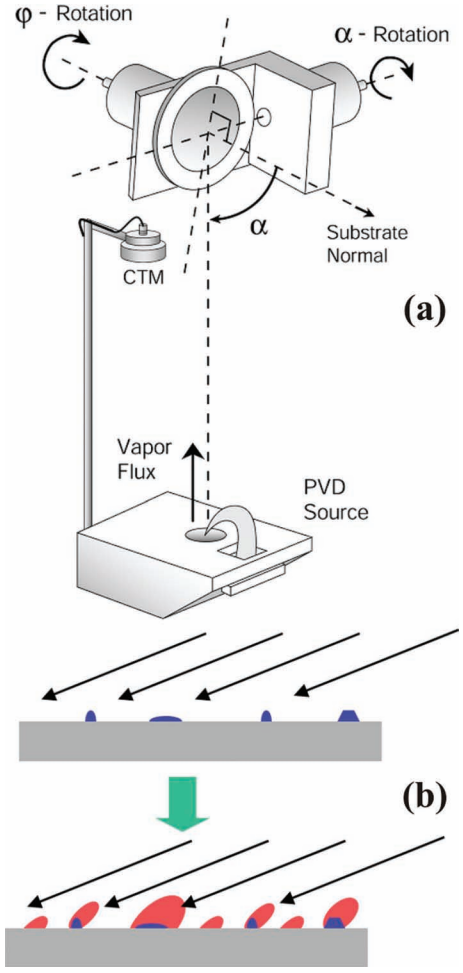

Figure 4. a) Schematic diagram showing the GLAD setup. Reproduced with permission.[93] Copyright 2004, The Optical Society. PVD-generated vapor flux is incident on a substrate with a large angle α with respect to the surface normal direction. b) The GLAD process. Reproduced with permission.[94] Copyright 2003, SPIE. The substrate continuously receives vapor flux from the incident direction. First, some island seeds are randomly distributed on the substrate surface, as shown in the upper panel. They then become 1D nanostructures, as shown in the lower panel.

vapor flux. The 1D morphology of nanohelices, nanospirals, and nanozigzags can be easily controlled by varying the angle and speed of the substrate rotation. Therefore, utilizing GLAD, it is furthermore possible to synthesize multifaceted 1D nanostructures that are expected to enhance the multifarious functionality for nanodevices or nanoelectronics.

2.2. Direct Chemical Deposition Techniques

There are obviously more direct chemical deposition techniques than direct physical deposition techniques. These synthesis methods include chemical vapor deposition (CVD), hot-filament metal-oxide vapor deposition (HFMOVD), thermal oxidation, solvothermal, sol-gel syntheses, etc. Direct chemical deposition techniques involve chemical reactions during the synthesis of 1D metal-oxide nanostructures. Oxygen gas plays an important role in the synthesis of 1D metal-oxide nanostructures.

2.2.1. Chemical Vapor Deposition

The semiconductor industry often uses different CVD techniques to produce compounds because of their advantages over PVD techniques. The CVD techniques include atmospheric-pressure, hot-filament, thermal-active, metal-organic, microwave-plasma, plasma-enhanced, low-temperature, and photo-assisted types. These various techniques essentially involve the chemical reactions and dissociations of reactive gases and volatile precursors at different pressures with specific flow rates so as to produce resultant compounds on the substrates. **Figure 5** shows schematic representations of the microwave-plasma (a) and hot-filament (b) CVD techniques. For the microwave-plasma CVD technique, the reactive gases absorb microwaves to produce plasma in the quartz tube. Plasma is composed of excited gases containing dissociated and reactive gases leading to the synthesis of 1D nanoproducts on the sample holder. In the hot-filament CVD technique, the reactive gases are associated and the associated gases also react with the hot filaments. Metal-oxides are one of the resultant compounds meaning that 1D metal-oxide nanostructures can be easily synthesized using the CVD techniques.[95] For example, nanoscale metallic catalysts are used in the CVD techniques to grow 1D metal-oxide nanostructures.[96,97] The diameters or widths of the 1D metal-oxide nanostructures strongly depend on the sizes of the nanoscale metallic catalysts. In fact, the structural morphology of 1D metal-oxide nanostructures is associated with the substrate temperature, molecule surface-diffusion rate, and concentrations of metal and oxygen vapors.

To take greater advantage of the CVD techniques for synthesizing 1D metal-oxide nanostructures, more attention is needed to overcome the disadvantages of the process, which include: i) precursor volatility at near room-temperature, ii) high deposition temperatures, iii) slow deposition rates, iv) chemical contamination, and v) difficulty in depositing multicomponent materials (mixed metal-oxides) using multisource precursors because different precursors have different vaporization rates. Basically, the high deposition temperatures of the CVD processes restrict their usage for the synthesis of 1D nanostructure because the high temperatures easily ruin the 1D morphology

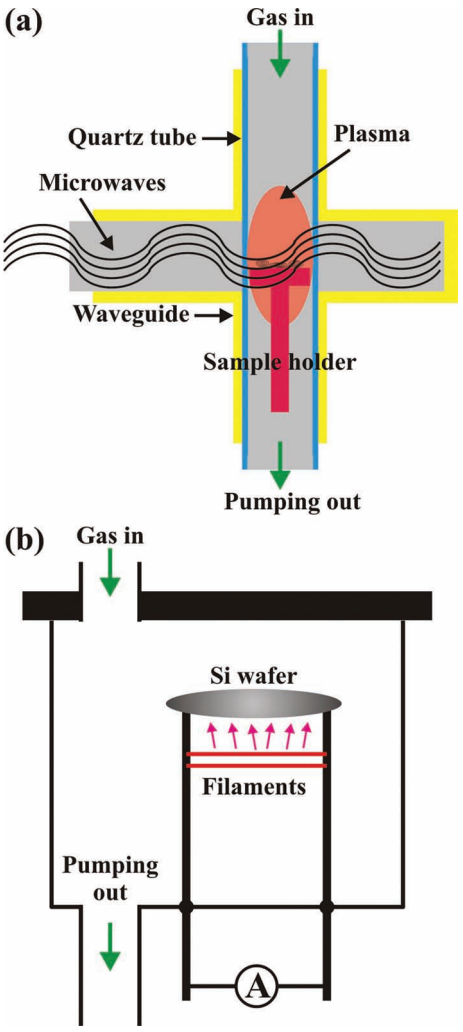

Figure 5. Schematic diagram of the a) microwave-plasma and b) hot-filament CVD techniques.

while promoting thin-film growth. However, 1D metal-oxide nanostructures can be grown at high deposition temperatures, because of their good thermal and chemical stability.[1,2] In Section 2.2.2, we introduce several 1D metal-oxide nanostructures grown at high deposition temperatures using the hot-filament metal-oxide vapor deposition (HFMOVD) technique. In contrast to the CVD techniques mentioned above, and apart from the low-temperature CVD technique, metal-organic chemical vapor deposition (MOCVD) techniques can reduce deposition temperatures so they can be utilized for the growth of 1D metal-oxide nanostructures.[98] The MOCVD technique offers the advantages of thickness control, accurate doping, large area deposition, and morphological variety. Most of the CVD synthesis techniques offer self-catalytic or layer-by-layer growth of 1D metal-oxide nanostructures.

2.2.2. Hot-Filament Metal-Oxide Vapor Deposition

HFMOVD[28–31,42,99–101] can be classified as one of the CVD techniques because of its similarity to conventional hot-filament

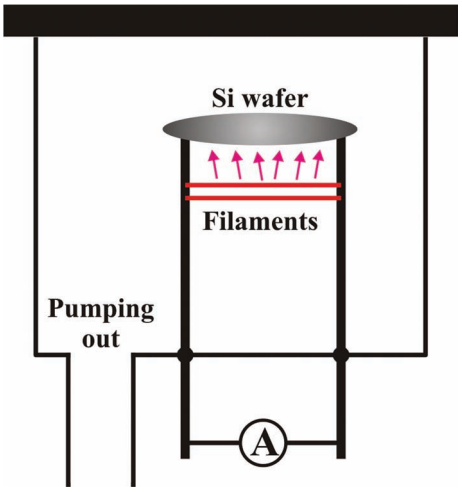

Figure 6. Schematic diagram of the HFMOVD technique.

chemical vapor deposition (HFCVD) techniques. However, the hot-filaments in the HFMOVD not only play an assistant role during deposition, but also become metal-vapor sources at high temperatures. When the metal filaments are heated to temperatures just higher than half of their melting point, the surface metals of the hot-filaments sublimate into the gas phase. The HFMOVD technique does not require the inlet of reactive gases for the synthesis of 1D metal-oxide nanostructures because the metal vapor can react with the residual oxygen gas in the chamber. Note that the chamber is pumped down to 1×10^{-2} Torr so very small amounts of oxygen and nitrogen gas still remain in the chamber. HFMOVD is a simple and cost-effective technique. A schematic diagram of the HFMOVD technique is shown in **Figure 6**. High current is passed through metal filaments mounted on the two electrodes in order to generate metal vapor. The HFMOVD technique involves three growth processes: i) thermal sublimation from the hot metal filament, ii) chemical vapor reaction of the sublimated metal-vapor with residual oxygen gas, and iii) condensation of the metal-oxide vapor to form 1D nanostructures. The three growth processes allow the HFMOVD technique to provide the catalyst-free vapor-solid (VS) growth for the synthesis of 1D metal-oxide nanostructures.

2.2.3. Sol-Gel Technique

The sol-gel technique is a wet-chemical process widely used in the fields of glass and ceramics, which involves the evolution of integrated inorganic networks through colloidal solutions (sol) and gelatinized colloidal solutions (gel) in liquid phases. The colloidal solution (sol) acts as the precursor for the integrated inorganic network (gel). Namely, when the liquid is removed from the sol, the sol becomes a gel. The sol-gel technique can be used to synthesize 1D metal-oxide nanostructures.[85,102] Typically, the precursors are alkali metal oxides or metal salts (such as chlorides, nitrates and acetates), usually surrounded by various reactive ligands. Hence, the precursors can undergo various processes of hydrolysis and condensation reactions. The starting material in the sol is processed to form dispersive metal oxides in contact with liquid water or diluted acid. Removal of the liquid water or diluted acid from the sol yields a gel, and the sol/gel transitions control the particle size and shape. For example, the calcination of the gel produces metal oxides. Schematic diagrams of the sol-gel technique for the synthesis of 1D metal-oxide nanostructures are shown in **Figure 7**. Figure 7a shows how the colloidal suspension (sol) of alkali metal oxides or metal salts is dissolved in solvents. Hydrolysis and condensation take place in the sol that is poured on the spinning substrates. As the sol is spun, the hydrolysis and condensation proceed continuously. As the sol gradually becomes a gel, the colloidal suspension coalesces to form 1D nanostructures due to the self-assembly effect, as shown in Figure 7b. The gel can be heated to completely remove the liquid water or dilute acid in the formation of the 1D metal-oxide nanostructures, as shown Figure 7c.

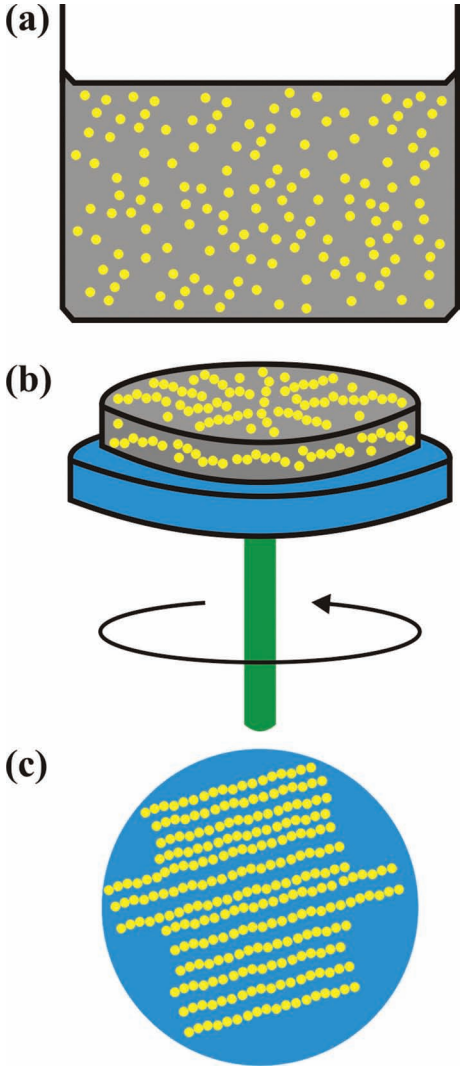

Figure 7. Schematic diagrams of the sol-gel technique: a) the colloidal suspension in the sol is represented by yellow spots; b) sol is spun to form a gel; and c) after the heat treatment 1D metal-oxide nanostructures grow on the substrate.

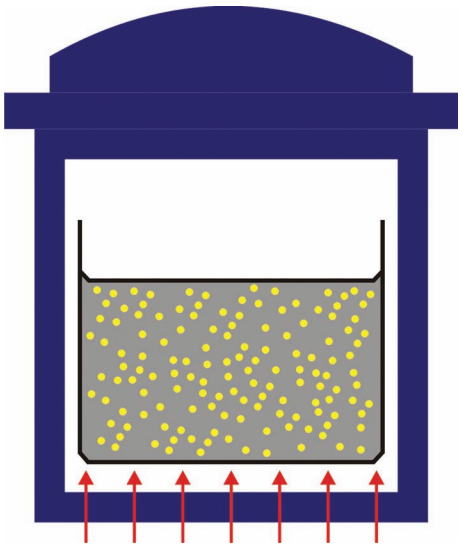

Figure 8. Schematic diagram of the solvothermal technique. The red arrows represent the external heating.

2.2.4. Solvothermal Technique

The solvothermal technique is a simple and universal synthesis method that utilizes solvents at moderate temperatures and high pressures for growing chemical compounds. It is very similar to the hydrothermal technique, the difference between the two techniques being in the precursor solutions. Namely, aqueous and non-aqueous precursor solutions are used for the hydrothermal and solvothermal techniques, respectively. The solvothermal technique is illustrated schematically in **Figure 8**. Appropriate metal-organic precursors and feasible reagents (e.g., glycine) are added to the solvent. The chemical reactions take place at critical temperatures and pressures in a stainless steel autoclave. The red arrows represent the external heating. Most of the metallic materials used to facilitate the growth of 1D metal-oxide nanostructures, such as CeO_2 nanorods[103] and WO_3 nanowires, are soluble in appropriate solvents.[104] The solvothermal technique can be used with the sol-gel technique. The size distribution, shape, and crystallinity of the 1D metal-oxide nanostructures can be precisely controlled by using appropriate parameters, such as the working temperature, reaction time, solvents, surfactants, and precursors.

3. Growth Mechanisms of 1D Metal-Oxide Nanostructures

As mentioned in Section 2, a large number of physical and chemical synthesis techniques have been used to grow a variety of 1D metal-oxide nanostructures. This section discusses the growth mechanisms of the 1D metal-oxide nanostructures for these techniques. The growth mechanisms basically involve physical or chemical reactions, nucleation, assemblies, and crystallization. The physical or chemical reactions of atoms, molecules, and ions primarily depend on the experimental setup and parameters so the reactions can strongly affect the nucleation. During this process the nuclei play an important role because they formed seeds for the growth of the 1D metal-oxide nanostructures. Their sizes, numbers, and morphology have a tremendous influence on the assembly of the atoms, molecules, and ions. In fact, the assemblies following nucleation decide the crystallization. Namely, the crystalline structures and morphology of the 1D metal-oxide nanostructures can be determined by the assemblies. Therefore, based on the reactions, nucleation, assemblies, and crystallization, we generally categorize the growth mechanisms into three types: vapor-liquid-solid (VLS), vapor-solid (VS), and solution-liquid-solid (SLS) growth mechanisms.

3.1. Vapor-Liquid-Solid (VLS) Growth Mechanism

Since the VLS growth mechanism was first reported for the growth of Si single crystals in 1964,[105] it has been widely applied for the growth of a variety of 1D metal-oxide nanostructures.[106,107] **Figure 9** show a schematic representation of the VLS growth mechanism. Catalysis plays an important role in the VLS growth mechanism. Metallic particles are used as catalytic seeds for the synthesis of crystalline 1D nanostructures, as shown in Figure 9a. The metallic particles become liquid eutectic alloys with reactive vapors at a certain temperature and the reactive vapors act as solutes, dissolving into metallic particles, as shown in Figure 9b. As the reactive vapor is continuously provided, the solutes in the liquid eutectic alloys are eventually saturate. The solutes then precipitate to form crystalline solid phases on the outside of the liquid eutectic alloys, as shown in Figure 9c. For a period of time, the crystalline solid phases grow as 1D nanostructures, as shown in Figure 9d. Obviously, the sizes and shapes of the 1D nanostructures that form during the VLS growth process are strongly dependent on the liquid eutectic alloys,[106] so selecting catalytic metals for the growth of 1D metal-oxide nanostructures is the major challenge.

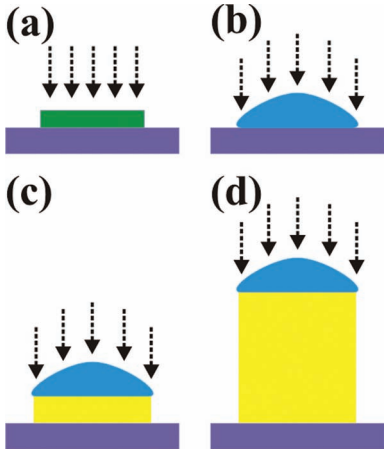

Figure 9. Schematic diagrams showing the VLS growth mechanism. The metallic particles (highlighted in green) used as catalytic seeds become liquid eutectic alloys (highlighted in blue) when reactive vapor (represented by dashed arrows) is continuously supplied. The 1D nanostructure (highlighted in yellow) grows during solute saturations.

3.2. Vapor-Solid Growth Mechanism

The VS growth mechanism is different from the VLS growth mechanism because no catalytic liquid metal is needed to assist in the growth of the 1D metal-oxide nanostructures. Only vapor and solid phases are involved in the VS growth mechanism. Self-catalysis is one of main factors. Since there are no catalytic liquid metals, the crystalline solids gain material directly from the heavy active vapors. As a consequence of the VS growth mechanism, materials anisotropically gain along the preferential axis to form the 1D morphology. There are three processes involved in the VS growth mechanism for the synthesis of 1D metal-oxide nanostructures by the HFMOVD technique:[28–31,42,99–101] i) thermal sublimation from the hot metal filament, ii) chemical vapor reaction of the sublimated heavy metal vapor with ambient oxygen gas, and iii) condensation of the heavy metal-oxide vapor into 1D nanostructures.

A schematic representation of the VS growth mechanism is shown in **Figure 10**. For the case where a heavy tantalum vapor sublimates from a hot tantalum filament at 1700 °C and the chamber pressure is 1×10^{-2} Torr,[30,100,101] we have the formula

$$2\mathrm{Ta}(s) \rightarrow 2\mathrm{Ta}(g) \quad (1)$$

The hot sublimated tantalum vapor collides and reacts with the leaking air or residual oxygen gas (see Figure 10a) to form TaO_x vapor (see Figure 10b), as follows:

$$2\mathrm{Ta}(g) + 2n\mathrm{O}_2(g) \rightarrow 2\mathrm{TaO}_x(g) + 2m\mathrm{O}_2(g) \quad (2)$$

where n, m, and x are arbitrary positive real numbers and $x \leq 2.5$. When the TaO_x vapor meets the substrate, it condenses into small droplets (see Figure 10c). Finally, the small droplets are converted into 1D crystalline $\mathrm{Ta_2O_5}$ nanorods (see Figure 10d), as in the formula below:

$$2\mathrm{TaO}_x(g) \rightarrow \mathrm{Ta_2O_5}(s) + [2(n-m) - (5/2)]\mathrm{O}_2(g) \quad (3)$$

Actually, the $2\mathrm{TaO}_x$ vapor is a pure $\mathrm{Ta_2O_5}$ gas, so Equation (2) can be rewritten as

$$2\mathrm{Ta}(g) + (5/2)\mathrm{O}_2(g) \rightarrow \mathrm{Ta_2O_5}(g) \quad (4)$$

Also, Equation (3) can be replaced by

$$2\mathrm{Ta_2O_5}(g) \rightarrow \mathrm{Ta_2O_5}(s) \quad (5)$$

so $x = 5/2$, $n = 5/4$ and $m = 0$. As can be seen in the discussion, heavy active vapors play a significant role for the growth of the as-synthesized 1D metal-oxide nanostructures. Chemical vapor reactions also help the VS growth. In addition, the growth factors leading to anisotropy and defects can enhance the effect of the VS growth mechanism for 1D metal-oxide nanostructures.

3.3. Solution-Liquid-Solid Growth Mechanism

The SLS growth mechanism, which was first reported in 1995,[108] has now become a promising approach for the mass production of semiconductors and metal-oxide nanomaterials with excellent control and high reproducibility in terms of both morphology and composition. The SLS growth mechanism is analogous to the VLS growth mechanism, while the SLS growth system is entirely immersed in an active solution. **Figure 11** shows schematic diagrams of the SLS growth mechanism. Catalysis still plays a vital role. Metallic particles are also

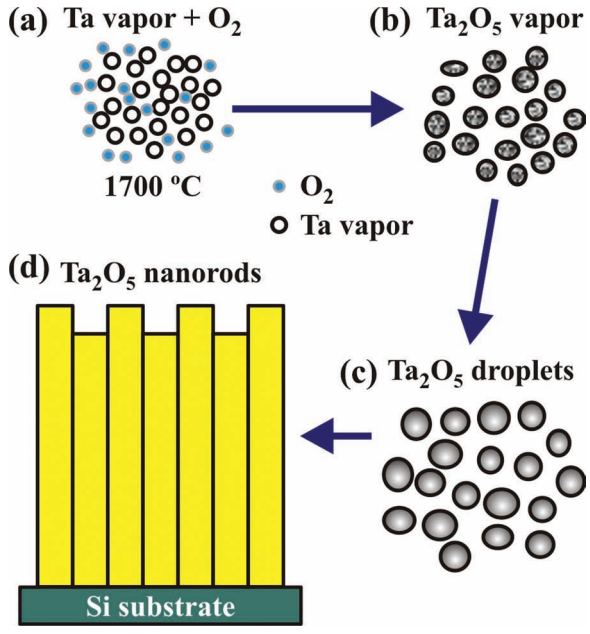

Figure 10. Schematic diagrams of the VS growth mechanism for 1D $\mathrm{Ta_2O_5}$ nanorods. Reproduced with permission.[101] Copyright 2010, International Union of Crystallography.

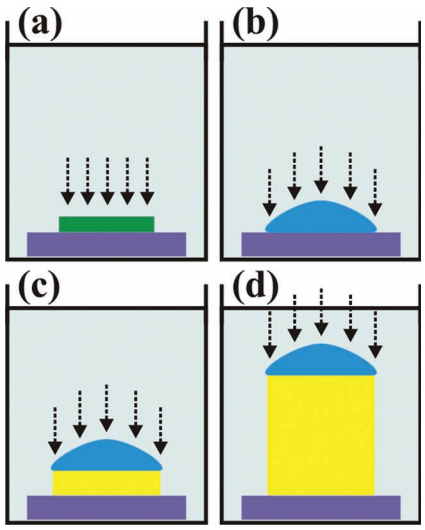

Figure 11. Schematic diagrams of the SLS growth mechanism, which is analogous to the VLS growth mechanism. The SLS growth system is immersed in an active solution (highlighted in light indigo). The metallic particles (highlighted in green) are used as catalytic seeds to become liquid eutectic alloys (highlighted in blue), when the active solution (represented by dashed arrows) is continuously supplied. The 1D nanostructure (highlighted in yellow) grows during the solute saturations

used as catalytic seeds to synthesize crystalline 1D nanostructures, as shown in Figure 11a. Organometallic precursors in the solution are used to supply the desired elements for the formation of 1D nanostructures. The metallic particles become liquid eutectic alloys in the active solution at a certain temperature because the organometallic precursors as solutes are dissolved into the metallic particles, as shown in Figure 11b. The solutes are eventually saturated by the liquid eutectic alloys. Then the solutes precipitate into the crystalline solid phases at the outside of the liquid eutectic alloys, as shown in Figure 11c. For a period of time, the crystalline solid phases continue to grow as 1D nanostructures until the precursors are depleted, as shown in Figure 11d. Similar to the VLS growth mechanism, the diameters of the 1D nanostructures depend on the liquid eutectic alloys. Homogeneous liquid eutectic alloys can be used to grow homogeneous 1D nanostructures. The catalytic activity, solubility, concentration, and temperature also strongly affect the morphology and crystalline structure of the as-synthesized 1D nanostructures.

The growth of the 1D Mn_3O_4 nanorods follows the SLS growth mechanism,[109] but does not require any catalytic metal as seed. In fact the catalytic metal seed is replaced by the liquid surfactant of the solution so the growth process can be described as a self-catalyzed SLS growth mechanism. 1D Cr_2O_3[110] and TiO_2[111] nanowires can be synthesized by the sol-gel technique which involves six processes: i) surface treatment of the substrates; ii) metal-oxide nucleation on the substrates; iii) formation of liquid eutectic alloys; iv) catalysis; v) gelation and crystallization; and vi) calcination and 1D growth. Hence, the growth process in the sol-gel technique is considered to be the SLS growth mechanism.

4. 1D Anisotropic Crystalline Nanostructures

Over the past decade, researchers have become increasingly engrossed in the study of 1D metal-oxide nanostructures. These 1D metal-oxide nanostructures are composed of only metal and oxygen elements. The metal elements are categorized as those with high melting-points: e.g., tungsten (W), molybdenum (Mo), tantalum (Ta), vanadium (V), niobium (Nb), titanium (Ti), and nickel (Ni), or low melting-points: e.g., zinc (Zn), bismuth (Bi), and tin (Sn). Various techniques can be used to synthesize 1D tungsten-, molybdenum-, tantalum-, vanadium-, niobium-, titanium-, nickel-, zinc-, bismuth-, and tin-oxide nanostructures. The synthesis and characterization of such nanostructures are discussed in this section, accompanied by the display of images of the as-synthesized 1D metal-oxide nanostructures by scanning electron microscopy (SEM), field-emission scanning electron microscopy (FESEM), and transmission electron microscopy (TEM).

4.1. Tungsten Oxide Nanostructures

Tungsten oxides are composed of a network of WO_6 octahedra with shared oxygen at the corners. Furthermore they can be composed not only of stoichiometric WO_2,[28] and WO_3,[112] but also non-stoichiometric WO_x ($2 < x < 3$), for example W_2O_5,[113] $W_{18}O_{49}$,[113–115] W_3O_8,[116] W_5O_{14},[117] and $WO_{2.9}$.[118] Tungsten oxides have varying crystalline phases, such as monoclinic, triclinic, orthorhombic, and tetragonal crystals with various transition temperatures.[112,119] Of the metal-oxides, tungsten oxides are commonly known to be one of the most fascinating and promising functional materials owing to their physical and chemical properties. For the purpose of obtaining a 1D morphology, tungsten oxides can be synthesized using varying techniques to form nanotubes,[113,120] nanobelts,[121,122] nanorods,[28,115] nanowires,[115] nanotips,[123] etc. The surface area of the 1D tungsten oxides is greatly increased as a consequence of a reduction in their size and dimensionality. Their electrochemical properties can be effectively enhanced, which makes the 1D tungsten oxide nanostructures more suitable for use in electrochromic smart windows,[57,116,124] catalysts[120,121], gas sensors,[125] and batteries.[126] In addition, the 1D tungsten-oxide nanostructures also possess good photoluminescent,[127] superparamagnetic[29] and thermochromic[128] properties, which make them more useful in nanodevices.

Well-crystalline and stoichiometric 1D metal-oxide nanostructures can still be synthesized in oxygen-poor environments. For example, 1D WO_2 nanorods[28] can be prepared using the HFMOVD technique. The FESEM image in **Figure 12**a shows discrete 1D WO_2 nanorods, ≈30 nm wide and a few micrometers long; the low-magnification TEM image inset to Figure 12a displays a single 1D WO_2 nanorod. The TEM image in Figure 12b shows a portion of the 1D WO_2 nanorod, illustrating that the 1D WO_2 nanorods possess a long straight body with a neat surface appearance and a flattened top. The selected-area electron diffraction (SAED) pattern inset to Figure 12b verifies that the 1D WO_2 nanorods have a monoclinic crystalline structure. Note that the selected area taken from the edge highlighted by a square box. Note that the incident electron beam is parallel to the $[\bar{1}00]$ direction. The SAED pattern also confirms that the 1D WO_2 nanorods consist of {011} planes that grow preferentially along the $[0\bar{1}1]$ direction. The high-magnification TEM image in Figure 12c illustrates a portion of the (011) lattice plane of a single 1D WO_2 nanorod in atomic resolution. The portion is also taken from the selected area. Two sets of parallel fringes are shown with a *d*-spacing of 0.37 nm located normal to each other.

In addition to the nanowires and nanorods, other hierarchical WO_3 nanostructures, such as nanoribbon/nanobelts,[122] can be synthesized using a simple hydrothermal method. The SEM and TEM images in **Figure 13**a show the 1D WO_3 nanoribbons to be a few micrometers long and ≈10 to 25 nm thick. It can be seen in the SAED pattern shown in the inset to Figure 13a that the 1D WO_3 nanoribbons grow preferentially along the [001] direction. In addition, a porous nanostructure of 1D $W_{18}O_{49}$ nanowires[129] can be prepared using the porous anodic alumina template based method. The FESEM images in the left-hand panel of Figure 13b show a bunch of hundred-nanometer-long 1D $W_{18}O_{49}$ porous nanowires. The TEM image in the right-hand panel of Figure 13b shows porous nanowires, 40–50 nm wide, arrayed in parallel. The 1D $W_{18}O_{49}$ porous nanowires have lacuna-like pores throughout their whole body, which may make them suitable for use in sensing and electrochromic nanodevices. This occurs because of the enhancement in the surface area of the 1D $W_{18}O_{49}$ porous nanowires as their size and

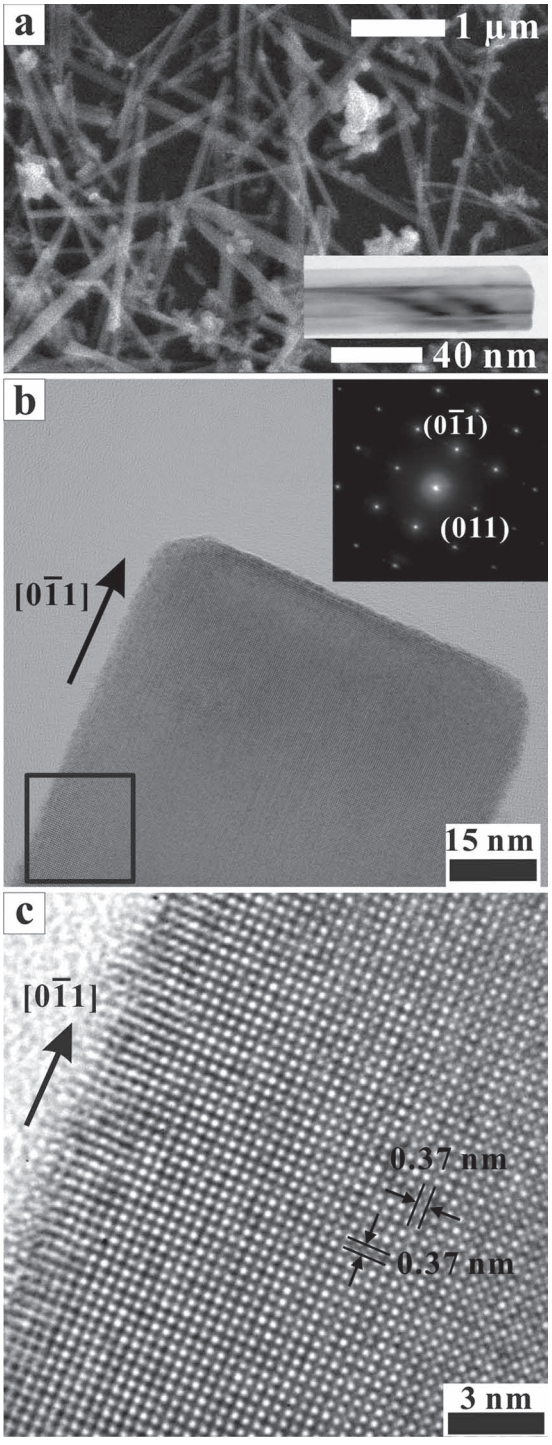

Figure 12. a) FESEM image showing 1D WO_2 nanorods. The inset to (a) shows a low-magnification TEM image of a single 1D WO_2 nanorod. b) TEM image displaying a portion of the single 1D WO_2 nanorod. The inset shows the SAED pattern for an area selected from the edge region highlighted within the square box. The 1D WO_2 nanorod consists of {011} planes with the growth axis in the [0$\bar{1}$1] direction. c) High-magnification TEM image of the selected area of the atomic-resolution [011] plane. Two sets of parallel fringes are shown having a d-spacing of 0.37 nm. Reproduced with permission.[28] Copyright 2005, American Institute of Physics.

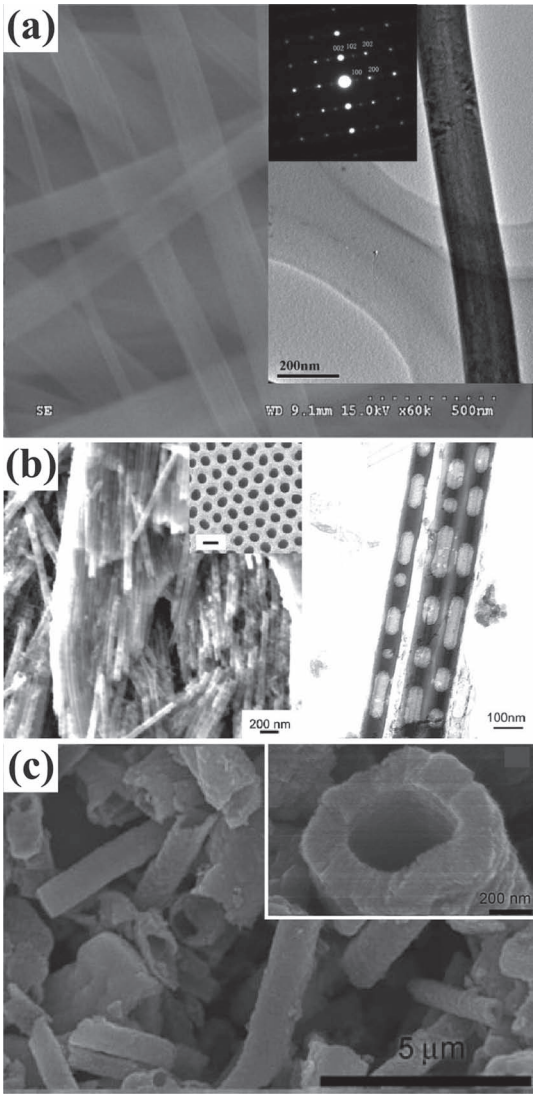

Figure 13. a) SEM and TEM images showing the 1D WO_3 nanoribbons. The SAED pattern in the inset shows how the 1D WO_3 nanoribbons grow preferentially along the [001] direction. Reproduced with permission.[122] Copyright 2006, American Chemical Society. b) The FESEM images in the panel on the left show a bunch of the 1D $W_{18}O_{49}$ porous nanowires. The TEM image in the right-hand panel shows the porous nanowires to be arrayed in parallel. Reproduced with permission.[129] Copyright 2005, Institute of Physics. c) The SEM image shows the nanoporous-walled WO_3 nanotubes with a high-magnification SEM image of a single nanotube shown in the inset. Reproduced with permission.[120] Copyright 2008.

dimensionality are reduced. However, 1D tubular structures may give even more surface area, which would make them useful for many applications. The nanoporous-walled WO_3 nanotubes are synthesized utilizing the solvothermal reaction.[120] The SEM images in Figure 13c show the nanoporous-walled WO_3 nanotubes to be 2–20 μm long and 300–1000 nm in diameter. The surfaces of the nanoporous-walled WO_3 nanotubes are not smooth, and their average inner diameter is ≈250 nm, as shown in the inset to Figure 13c. The rough inner and outer surfaces of the nanoporous-walled WO_3 nanotubes provide greater surface area, so that higher photocatalytic activity is presented.

4.2. Molybdenum Oxide Nanostructures

Molybdenum oxides consist of a network of MoO_6 octahedra or MoO_4 tetrahrdra[130] with shared oxygen atoms at the corners. They can not only be composed of stoichiometric MoO_3,[131] and MoO_2,[31,132] but also non-stoichiometric MoO_x ($2 < x < 3$), such as Mo_4O_{11},[133,134] Mo_8O_{23},[133,135] and $Mo_{18}O_{52}$.[133,135] Molybdenum oxides can have a variety of crystalline phases including cubic, orthorhombic, monoclinic, triclinic, and hexagonal crystals. Among the metal-oxides, the molybdenum oxides are one of the most attractive functional materials due to their unique physical and chemical properties. In quest of a 1D morphology, molybdenum oxides are prepared by various synthesis techniques to form nanorods,[29,31,136] nanowires,[92,132] nanobelts,[131,137,138], nanofibers,[137], nanoribbons,[139,140] nanotubes,[141–143] etc. Recently, 1D molybdenum oxide nanostructures have attracted a lot of scientific attention due to their multifarious uses in electrochromic devices.[143] as photocatalyst,[144] for electrode materials for Li-on batteries,[131] as supercapacitors,[145] in gas sensors,[146] in field emission devices,[132] etc. Many techniques have been developed to synthesize varying 1D molybdenum oxide nanostructures and to control their structural, physical, and chemical properties for applications in nanodevices.

Orthorhombic MoO_3 nanorods (≈50 nm thick, 150–300 nm wide and a few tens of micrometers long) with excellent morphological homogeneity can be synthesized utilizing a hydrothermal method[136] with varying acidification treatments of ammonium heptamolybdate tetrahydrate at 140–200 °C. Large-area arrays of molybdenum oxide nanowires or nanorods can be easily synthesized by the HFMOVD technique.[29,31,132] The MoO_2 nanowires have good field emission behavior.[132] Also, 1D nanobranched structures[31] are easily formed at a high pressure of 600 Torr. The morphology of the 1D nanobranched structures has a forked trunk and straight shoots, as shown in **Figure 14**a,b, respectively. This HFMOVD technique raises the question as to why the 1D nanorods of molybdenum oxides are preferentially MoO_2 rather than MoO_3. Molybdenum oxides exist with either a tetrahedral MoO_4 or octahedral MoO_6 symmetry. MoO_2 is usually a monoclinic crystal that has a highly anisotropic and distorted rutile structure with strong Mo–Mo bonds, while MoO_3 is typically an orthorhombic crystal that possesses a layered structure with two layers of weak chains of MoO_4 tetrahedra along the *c*-axis. When there is a lack of oxygen, the molybdenum oxide vapor is preferential to the MoO_2 vapor so the vapor condenses to form MoO_2 nanostructures rather than MoO_3 nanostructures. In addition, two distinct MoO_2 and MoO_3 structures are deposited above their melting points of 1100 and 795 °C, respectively. Using the HFMOVD technique, 1D MoO_2 nanorods can be obtained at filament temperatures greater than 1200 °C, also indicating that the MoO_2 vapor condenses preferentially to form MoO_2 nanostructures, rather than MoO_3 nanostructures.

1D molybdenum-oxide nanobelts or nanoribbons[131,137–140,144] of several micrometers in length can be synthesized by hydrothermal and template synthesis methods. The SEM image in **Figure 15**a shows a very special lamellar structure of the 1D MoO_3 nanobelts.[137] The nanobelts are several tenths of micrometers long and 200–600 nm wide, which is significantly wider and longer than most of the 1D metal-oxide nanobelts. Large self-standing films are displayed in the photograph in Figure 15b.[139] The SEM image in the inset to Figure 15b shows large self-standing films consisting of 1D MoO_3 nanoribbons with rectangular features 5–10 μm long, 90-–300 nm wide, and 30–50 nm thick. 1D molybdenum-oxide nanotubes[141–143] several micrometers in length can be synthesized by infrared-irradiation heating, hydrothermal, and combustion-flame synthesis methods. The SEM images in Figure 15c show the 1D rectangular MoO_2 nanotubes.[143] The outer diameter and length of the rectangular nanotubes are ≈2 and ≈100 μm, respectively. Although they should not actually be called nanotubes, however, since the walls are only ≈100 nm thick, as shown in the inset to Figure 15c, we still call them nanotubes. In addition, single-wall MoO_3 nanotubes, such as single-wall carbon nanotubes, can be synthesized by a thiol-assisted hydrothermal method.[142] The SEM images in Figure 15d show that all of the single-walled MoO_3 nanotubes several hundred nanometers in length are almost uniform in diameter and most of them are open in the ends. As shown in the inset to Figure 15d, the diameters are around 6 nm, so the thickness of the single-wall is only a few angstroms. The nanotubes are hypothesized to have unique electrical and optical properties for nanodevices.

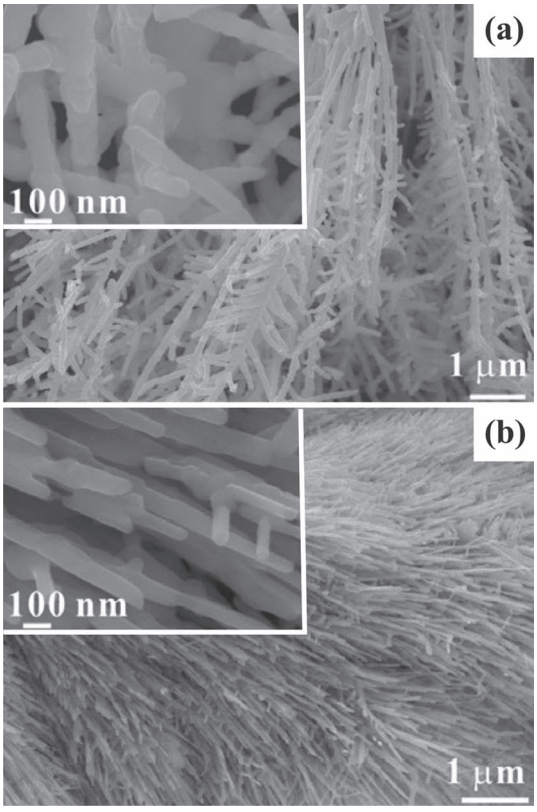

Figure 14. FESEM images of two distinct nanobranched structures: a) fork-trunk and b) straight-shoot 1D MoO_2 nanorods. The insets show the high-magnification FESEM images. Reproduced with permission.[31] Copyright 2007, Institute of Physics.

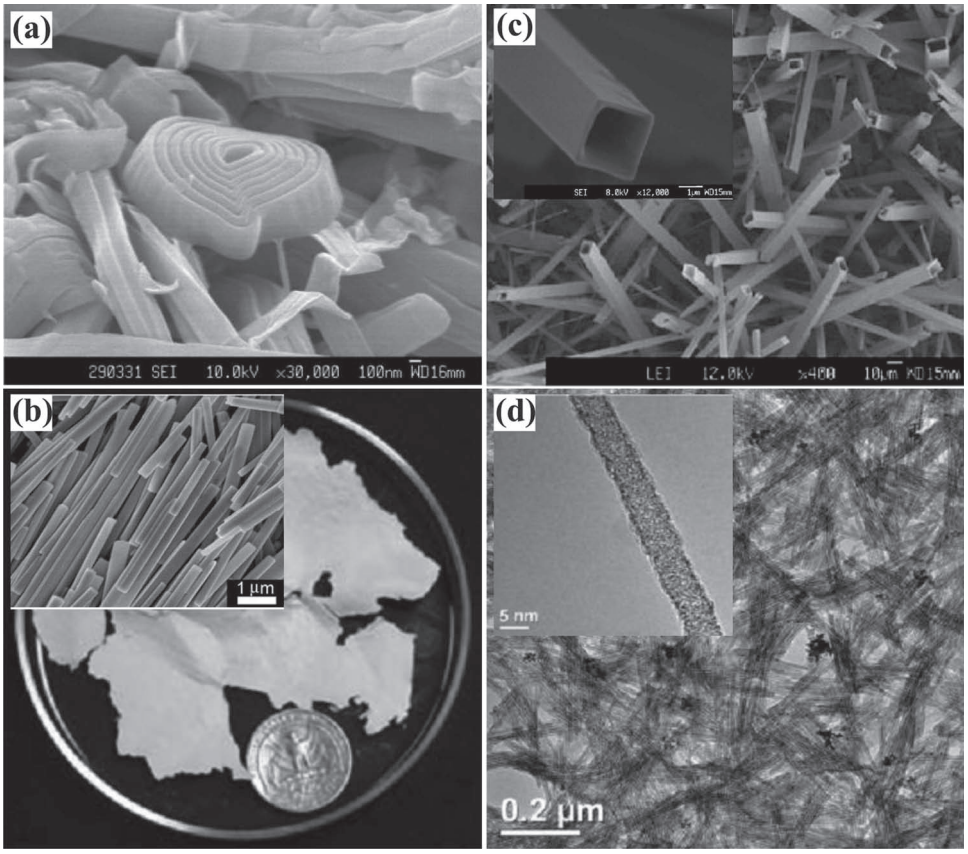

Figure 15. a) SEM image of the lamellar-structure 1DMoO_3 nanobelts. Reproduced with permission.[137] Copyright 2005, American Chemical Society. b) Photograph of large self-standing films of nanoribbons. The SEM image in the inset shows the 1D MoO_3 nanoribbons. Reproduced with permission.[139] Copyright 2006, Springer. c) SEM images showing the rectangular 1D MoO_2 nanotubes. Reproduced with permission.[143] Copyright 2010, Springer. d) TEM images of single-walled MoO_3 nanotubes. Reproduced with permission.[142] Copyright 2008, American Chemical Society.

4.3. Tantalum Oxide Nanostructures

Tantalum oxides are composed of a network of TaO_6 octahedra and TaO_7 pentagonal bipyramids with shared oxygen atoms and in addition to Ta_2O_5[30,58,100,101,147–153] they can also be TaO_x ($x < 2.5$), such as TaO_2,[152,153] TaO_3,[153,154] TaO,[153] Ta_2O,[155] and Ta_3O.[156] Tantalum oxides have various crystalline phases including tetragonal, hexagonal, orthorhombic, triclinic, monoclinic, and cubic crystals, although there are discrepancies in several phase transitions at various temperatures.[30,100,101] In the quest for a 1D morphology, tantalum oxides have been synthesized using various techniques to form nanorods,[30,58,100,101,147,149,150] nanoblocks,[150] nanowires,[157] nanotubes,[148,157] nanofibers,[158] etc. Among the known metal-oxides, the tantalum oxides have received considerable attention due to their unique properties such as large ion-diffusion coefficient and high electrochromic reversibility,[58] high dielectric constant (90–110),[159] high refractive index (≈2.125 at 500 nm),[160] and large band gap (≈4.4 eV).[149] The 1D tantalum oxide nanostructures are expected to have more unique properties than the bulk tantalum oxides. However, in contrast to the synthesis of tantalum oxide thin films, there have been only a few attempts to make 1D tantalum oxide nanostructures. The sol-gel method was the first method used to produce 1D Ta_2O_5 nanorods,[147] but these nanorods were non-uniform. Soon after this, a variety of chemical deposition techniques were developed to synthesize large-scale, high-density arrays of 1D Ta_2O_5 nanorods,[30,100,101] nanoblocks,[150] nanowires,[157] nanotubes,[148,157] and nanofibers.[158]

The HFMOVD technique was used to synthesize 1D Ta_2O_5 nanorods and nanoblocks arranged in a large-scale and high density array,[30,149,150] as shown in **Figure 16**. The FESEM images in Figure 16a,b illustrate the top and side views of a portion of the large-area high-density 1D Ta_2O_5 nanorod array synthesized on a Si substrate. The 1D Ta_2O_5 nanorod array is very compact, but its textural boundaries are clearly visible. The array contains ≈1675 Ta_2O_5 nanorods per square micrometer. In Figure 16b, it can be seen that the 1D Ta_2O_5 nanorods are on average ≈500 nm long. The high-magnification FESEM image in the inset to Figure 16a shows the single Ta_2O_5 nanorods separated from the large-area high-density array to be 20–25 nm wide and ≈500 nm long. They are roughly straight and their diameters are approximately uniform throughout the entire rod body. In addition, the FESEM image in Figure 16c shows the surface morphology of the Ta_2O_5 nanoblocks, which are randomly arranged in large-area stacks. The Ta_2O_5 nanoblock stacks are very compact, but the textural boundaries are clearly visible. The stacks contain ≈1630 nanoblocks per square micrometer, with various widths, all smaller than 34 nm.

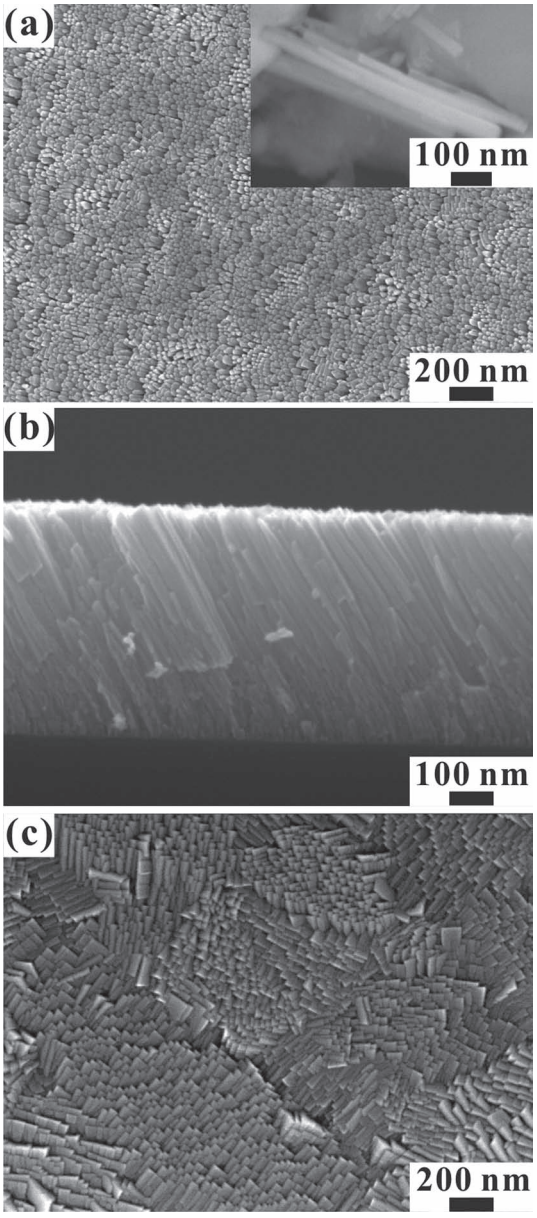

Figure 16. FESEM images showing the top (a) and side (b) views of a large-area and high-density array of 1D Ta_2O_5 nanorods on a Si substrate. The high-magnification FESEM image in the inset to (a) shows single 1D Ta_2O_5 nanorods separated from the array. Reproduced with permission.[30] Copyright 2008, American Chemical Society. c) The FESEM image displays large-area Ta_2O_5 nanoblock stacks on a Si substrate. Reproduced with permission.[150] Copyright 2011, Royal Society of Chemistry.

The as-synthesized large-scale high-density array of the 1D Ta_2O_5 nanorods or nanoblocks has good thermochromic,[30] electrochromic,[58] and photoluminescent (PL)[149,150] properties. In fact, the array contains ≈93.5% of the orthorhombic (β) phase and ≈6.5% of the tetragonal (α) phase. The thermochromic phase transformations of the 1D Ta_2O_5 nanorods can be analyzed at elevated temperatures ranging from 80 to 750 K. The XRD results of the thermochromic phase transformations indicate five possible phase transformations: i) α to α (α-α); ii) α to β (α-β); iii) β to β (β-β); iv) β to α (β-α); and v) α to α to β (α-α-β). In contrast to the Ta_2O_5 thin films, the 1D Ta_2O_5 nanorods are the most suitable for electrochromic applications because they can offer the advantages of larger surface areas and more capillary pathways for the ion intercalation and deintercalation.[58] The shared oxygen located at the in-plane and cap sites of the Ta_2O_5 nanostructures can be easily volatilized to yield many oxygen vacancies, the most prominent type of defects in Ta_2O_5. Each oxygen vacancy provides a reduction of two electrons at two dangling bonds. The dangling bonds can give rise to trap levels within the bandgap of Ta_2O_5, which are able to trap excited electrons. When the excited electrons drop from the trap levels to the ground state, visible light is emitted.[149,150] In other words, the presence of oxygen vacancies makes Ta_2O_5 nanostructures an n-type semiconductor, playing a key role in the PL emissions of Ta_2O_5.

High-aspect-ratio 1D Ta_2O_5 nanotube arrays can be electrochemically synthesized by the one-step anodization of Ta foil.[161,162] First, ordered nanodimples with a pore diameter of 40–55 nm, as shown in **Figure 17**a, are formed on the surfaces of Ta foil immersed in an aqueous electrolyte containing HF:H_2SO_4 in volumetric ratios of 1:9 and 2:8 at applied voltages ranging 10–20 V. Then, the high-aspect-ratio 1D Ta_2O_5 nanotube arrays, as shown in Figure 17b, can be acquired after the addition of 5–10% of either ethylene glycol (EG) or dimethyl sulfoxide (DMSO) to the HF and H_2SO_4 aqueous electrolytes. The resultant dimpled Ta is the stable surface morphology that occurs after the first few seconds. Then the large-area, high-density, and fully vertically aligned Ta_2O_5 nanotubes grow, as shown in Figure 17c. There is rapid and robust growth of self-ordered arrays of Ta_2O_5 nanotubes with independent control over the diameter, wall thickness, length, and crystallinity. The diameter and length can be tuned and increased over a factor of four in size (from 35–200 nm) and up to 50%, respectively.[148] In addition, the growth rates and wall thicknesses can be controlled by varying the special experimental parameters. However, the Ta_2O_5 nanotubes have a patchy morphology, which restricts the applications because they cannot be controllably detached as templates or membranes. The development of a controllable process for the fabrication of non-patchy, stable, high-aspect-ratio Ta_2O_5 nanotubes is important for use in templates or membranes. The electrochemical anodization conditions can be tuned to remove the intact Ta_2O_5 nanotubular films to form free-standing, nanotubular templates or membranes, which can be applied for use as a dielectric material in electrolytic capacitors.[163]

4.4. Vanadium Oxide Nanostructures

Vanadium oxides consist of VO_5 square pyramids or distorted VO_6 octahedra with shared oxygen atoms and can appear in various chemical forms such as V_2O_5,[164–166] VO_2,[167–170] V_2O_3,[170,171] V_3O_5,[171] V_3O_7,[172] V_4O_7,[171] V_5O_9,[173] V_6O_{11},[173] and V_6O_{13}.[170,171] These forms of vanadium oxides form crystals, including orthorhombic, cubic, triclinic, tetragonal, monoclinic, and rhombohedral phases. In fact, vanadium oxides are employed in various scientific and technological applications owing to their versatile redox-dependent physical and chemical

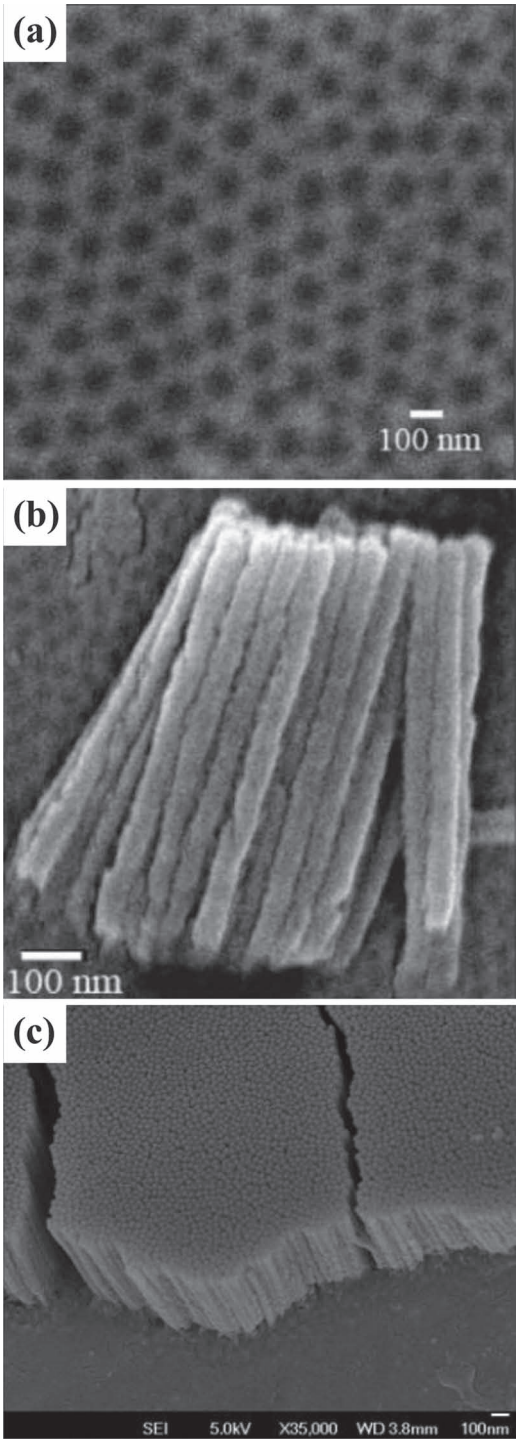

Figure 17. FESEM images of () the ordered nanodimples with pore diameters of 40–55 nm that formed on the surface of the tantalum foil, b) the high-aspect-ratio 1D Ta_2O_5 nanotubes, and c) the large-area, high-density, fully vertically aligned Ta_2O_5 nanotubes. Reproduced with permission.[161] Copyright 2008, American Chemical Society.

properties. The 1D morphology are useful for many applications and therefore a variety of deposition methods, including thermal evaporation, surfactant-assisted solution, and hydrothermal/solvothermal synthesis, have been developed to synthesize 1D vanadium oxide nanostructures. These 1D vanadium oxide nanostructures can be grown in the forms of nanorods,[164] nanowires,[165,166,174] nanobelts,[169,175–178] nanorolls,[176] nanotubes,[179–182] etc.

Unlike the other 1D metal-oxide nanostructures, vanadium-oxide nanotubes are more easily synthesized than the other 1D nanostructures. Among the 1D nanostructure morphologies, the tubular morphology basically possesses the most interesting properties, with more effective surface areas than the others. Mixed-valence vanadium oxide nanotubes can be straightforwardly mass produced by a low-temperature, soft chemistry synthesis method.[180] This method allows for a high yield, meaning that vanadium oxide nanotubes can be grown in gram quantities with the alignment of parallel oriented nanotubes several hundred micrometers long. The TEM images in **Figure 18** show the side and top (cross-sectional) views of vanadium oxide nanotubes. The vanadium oxide nanotubes obviously consist of multiwalls, as shown in Figure 18a. The inset to Figure 18a displays a single multiwalled vanadium oxide nanotube that is composed of four distinct topological regions, including the tube opening, outer surface, inner surface, and interstitial region. The TEM images in Figure 18b,c show top or cross-sectional views of the vanadium oxide nanotubes, revealing them to be the scroll-like and concentrically circular possessing open ends and multiwalls. The elemental maps in Figure 18d,e illustrate vanadium oxide nanotubes (Figure 18c) with vanadium and carbon distributions, respectively, confirming the vanadium oxide nanotubes to be the concentric circular cylinders with two vanadium oxide walls.

Of the 1D nanostructures, nanobelts, with their rectangular cross-section, are expected to display a unique potential for use in nanodevices because they are very thin and flexible. An environmentally friendly chemical route can be use to synthesize large-scale orthorhombic V_2O_5 nanobelts in a H_2O_2 aqueous solution.[177] The FESEM and TEM images in **Figure 19** show 1D V_2O_5 single-crystalline nanobelts synthesized at 180 °C for 48 h.[177] Figure 19a displays 1D V_2O_5 single-crystalline nanobelts with lengths of up to tens of micrometers. The inset to Figure 19a clearly shows rectangular cross-sections of the 1D V_2O_5 nanobelts, which are 100–300 nm wide and 30–40 nm thick. Figure 19b,c show 1D V_2O_5 nanobelts that have been cleaved as indicated by the arrows. The TEM image in Figure 19d shows one single 1D V_2O_5 nanobelt that has grown along the [010] direction. The SAED pattern in the inset to Figure 19d, taken from the single nanobelts, verifies that the 1D V_2O_5 nanobelts are comprised of orthorhombic crystals of V_2O_5 with a preferential growth direction along the [010] direction. The HRTEM image in Figure 19e shows two clear interplanar spacings (d_{020} = 1.78 and d_{200} = 5.75 Å), confirming the crystalline structure of the 1D V_2O_5 nanobelts.

4.5. Niobium Oxide Nanostructures

Niobium oxides are composed of NbO_4 tetrahedrons and NbO_6 octahedrons with shared oxygen atoms[183] and they come in varying forms of stoichiometric Nb_2O_5,[184–188] NbO,[183] NbO_2,[189] $Nb_{10}O_{25}$,[190] and non-stoichiometric $Nb_{12}O_{29}$,[191,192] and $Nb_{22}O_{54}$.[190,192] Niobium oxides have a variety of crystalline

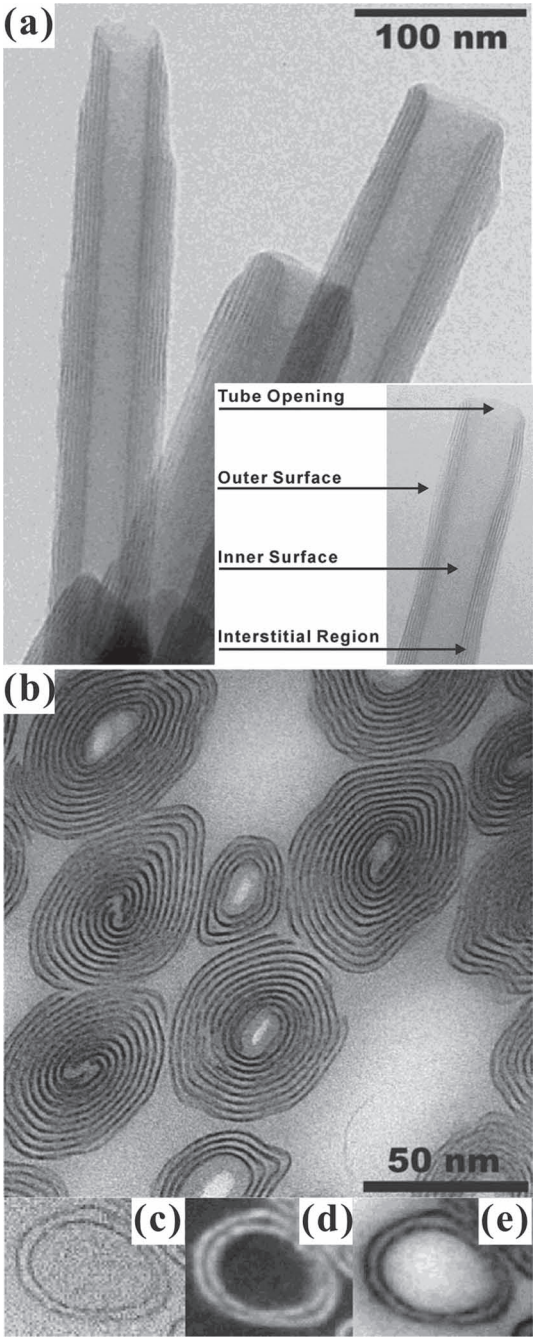

Figure 18. a) TEM images of vanadium-oxide multiwalled nanotubes (template: docosylamine). The inset to (a) shows the four distinct topological regions of the tube opening, outer surface, inner surface and interstitial region. b,c) TEM images of cross-sections of vanadium-oxide multiwall nanotubes. d,e) Elemental maps of vanadium-oxide multiwalled nanotubes with vanadium and carbon distributions. Reproduced with permission.[180] Copyright 2000.

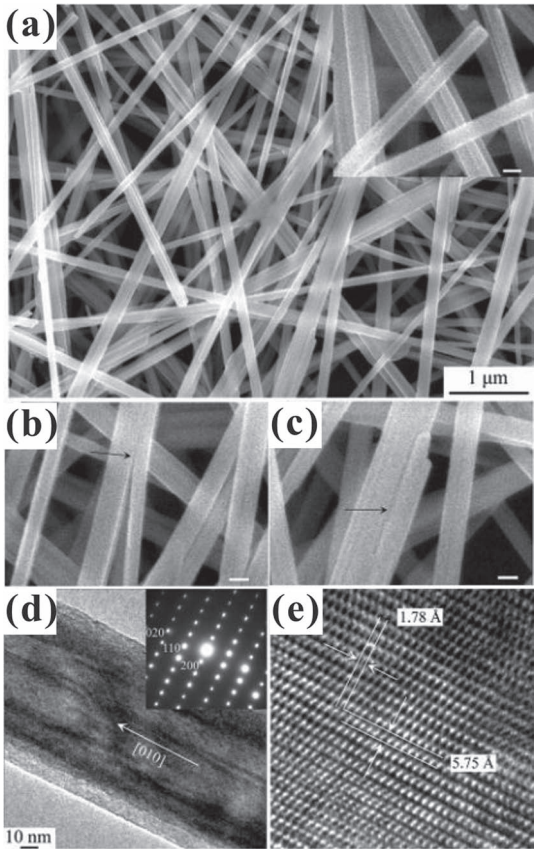

Figure 19. a–c) FESEM images of the 1D V_2O_5 nanobelts. d) TEM images and SAED patterns of single 1D V_2O_5 nanobelts. e) High-magnification TEM images of single 1D V_2O_5 nanobelts. Reproduced with permission.[177] Copyright 2006, American Chemical Society.

phases, including orthorhombic, tetragonal, monoclinic, cubic, and hexagonal crystals, and their many advantageous properties make them useful for various scientific and technological applications, such as catalysis,[184] field emission,[185] photovoltaic,[186] and electrochromic effects.[188] A variety of deposition methods have been developed for the synthesis of 1D niobium oxide nanostructures in a quest for a 1D morphology. These 1D niobium oxide nanostructures can be grown in the forms of nanorods,[188] nanowires,[185,193–195] nanobelts,[186] nanotubes,[196] etc.

Three typical 1D nanostructures, nanowires, nanobelts, and nanorods, are shown in **Figure 20**. The SEM images in Figure 20a show bundles of 1D Nb_2O_5 nanowires about 50 nm wide and with lengths smaller than the millimeter scale. These 1D Nb_2O_5 nanowires are grown using rapid low-temperature synthesis in the temperature range from 50 to 300 °C.[193] The rapid low-temperature synthesis method is based upon controlling the exposure of niobium foils to low-pressure, weakly ionized, fully dissociated, and cold oxygen plasma. The plasma is generated by an electrical current passing through oxygen gas. The oxygen molecules in the oxygen plasma are rapidly ionized, dissociated, and excited by inelastic collisions with the electrons so they became extremely reactive and easily oxidize on the niobium foil to grow the 1D Nb_2O_5 nanowires. The SEM images in Figure 20b display large-scale 1D Nb_2O_5 nanobelts, which are ≈60 nm wide and smaller than the millimeter scale in length. The 1D Nb_2O_5 nanobelts are synthesized using a simple ambient synthetic route.[186] First, layered structure $NH_4Nb_3O_8$ nanobelts are prepared from layered $K_4Nb_6O_{17}$ and then as-prepared $NH_4Nb_3O_8$ nanobelts are converted to

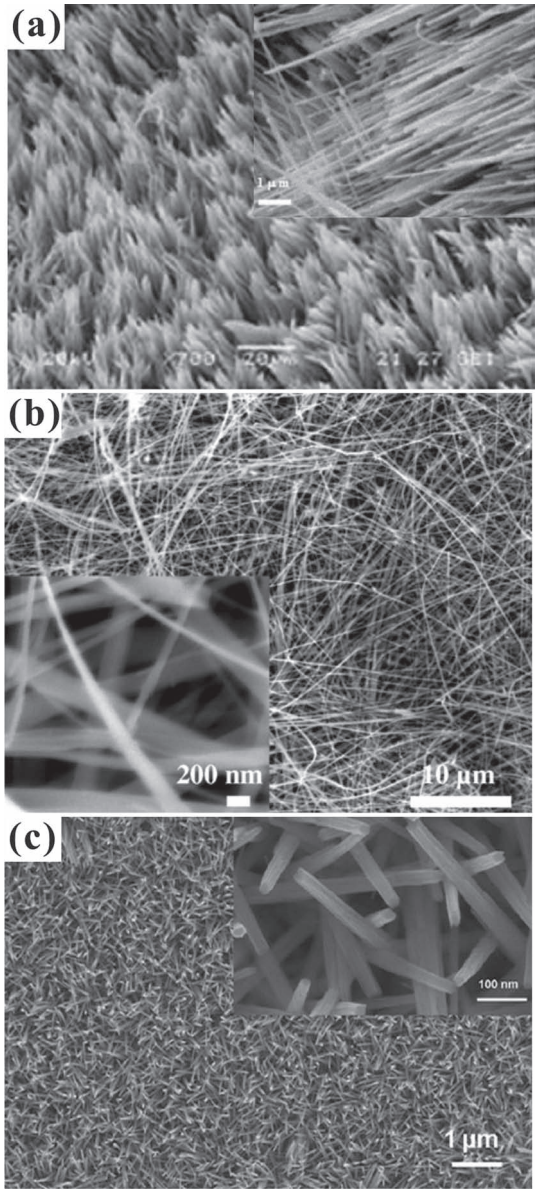

Figure 20. a) SEM images of bundles of 1D Nb_2O_5 nanowires grown by a rapid low-temperature synthesis. Reproduced with permission.[193] Copyright 2005. b) SEM images of large-scale 1D Nb_2O_5 nanobelts synthesized by a simple ambient synthetic route. Reproduced with permission.[186] Copyright 2008, Elsevier. c) FESEM images of large-scale arrays of 1D Nb_2O_5 nanowires grown by a facile hydrothermal process. Reproduced with permission.[188] Copyright 2011, Elsevier.

single-crystal Nb_2O_5 nanobelts by thermal treatment in air. The FESEM images in Figure 20c show large-scale arrays of 1D Nb_2O_5 nanorods, which are ≈50 wide and micrometers long. The 1D Nb_2O_5 nanorod arrays can be grown by a facile hydrothermal process.[188] Niobium foil is placed into an aqueous ammonium fluoride (NH_4F) solution, then annealed at 150 °C in a teflon lined autoclave for 96 h to obtain the large-scale 1D Nb_2O_5 nanorod arrays.

Tubular nanostructures are of great interest to scientists. The simple ambient synthetic route[186] can be used to grow not only nanobelts but also nanotubes of Nb_2O_5. The layered-structure $K_4Nb_6O_{17}$ can be chemically exfoliated to become uniform lamellar colloids which are easy to rearrange and roll into tubular morphologies. The TEM images in **Figure 21**a,b show 1D Nb_2O_5 nanotubes that are ≈30 nm wide and a few hundred nanometers long. The 1D Nb_2O_5 nanotubes can also be synthesized by a simple ambient synthetic route.[196] First, $K_4Nb_6O_{17}$ nanotubes with a layered structure are chemically exfoliated by aqueous tetra-(n-butyl)ammonium hydroxide (TBAOH) to form $H_4Nb_6O_{17}{\bullet}nH_2O$ lamellar colloids which are then scrolled into tubular nanostructures. The as-prepared $H_4Nb_6O_{17}{\bullet}nH_2O$ nanoscrolls can be converted to 1D Nb_2O_5 nanobelts by thermal treatment at 400–425 °C for 30–180 min. The SAED pattern in the inset to Figure 21b reveals the 1D Nb_2O_5 nanotubes to be polycrystals. The high-magnification TEM images in Figure 21c show the single 1D Nb_2O_5 nanotube to be a single crystal. The lattice fringes are parallel to the nanotube walls, indicating the 1D Nb_2O_5 nanotubes grow along the [100] direction. The SAED pattern inset to Figure 21c reveals that points A and B correspond to the (001) and (180) planes with *d*-spacings of 3.93 and 3.14 Å, respectively.

4.6. Titanium Oxide Nanostructures

As is the case for the other metal oxides mentioned above, titanium oxides also have various chemical forms that can be categorized into the typical TiO_2[197–202] and Ti_nO_{2n-1} forms, such as TiO,[203] Ti_2O_3,[204] Ti_3O_5,[205] Ti_4O_7,[206] Ti_5O_9,[207] Ti_7O_{13},[208] and Ti_9O_{17}.[207] Titanium oxides possess varying crystalline phases, including tetragonal, orthorhombic, monoclinic, hexagonal, triclinic, and rhombohedral crystals, but titanium dioxides (TiO_2) can mainly be sorted into three crystalline structures of rutile (tetragonal structure), anatase (tetragonal structure), and brookite (orthorhombic structure). The TiO_2 structures are composed of octahedra with shared oxygen atoms. The neighboring rutile octahedra share corners along the [110] direction, while the anatase form share corners along the (001) planes. The titanium oxides have received considerable attention due to their important functional properties in photovoltaic[199,200] and photocatalytic devices,[209] for gas sensing,[210] and in electrochromic devices,[211,212] The incorporation of 1D nanostructures may enhance the functional properties for practical applications. In the quest for 1D nanostructures, various synthesis techniques have been used to form the nanorods,[213] nanowires,[214,215] nanofibers,[214,215] nanobelts,[215] and nanotubes,[197,198,201,210,213–215] of TiO_2.

Of the 1D titanium oxide nanostructures, TiO_2 nanotubes are easy to synthesize. It is known that the tubular nanostructures possess more effective surface areas than the other nanostructures because of their very unique properties. Large-scale highly ordered TiO_2 nanotubes can be mass produced by the potentiostatic anodization of a titanium film in a fluoride containing electrolyte.[200] The FESEM images in **Figure 22**a show large-scale highly ordered TiO_2 nanotube arrays. The TiO_2 nanotubes are a few micrometers long. The pore diameters of the back and front sides are ≈110 and ≈46 nm, and the wall thicknesses are 20 and 17 nm. The typical TiO_2 nanotubes grown by anodic synthesis methods usually have irregular and rough side

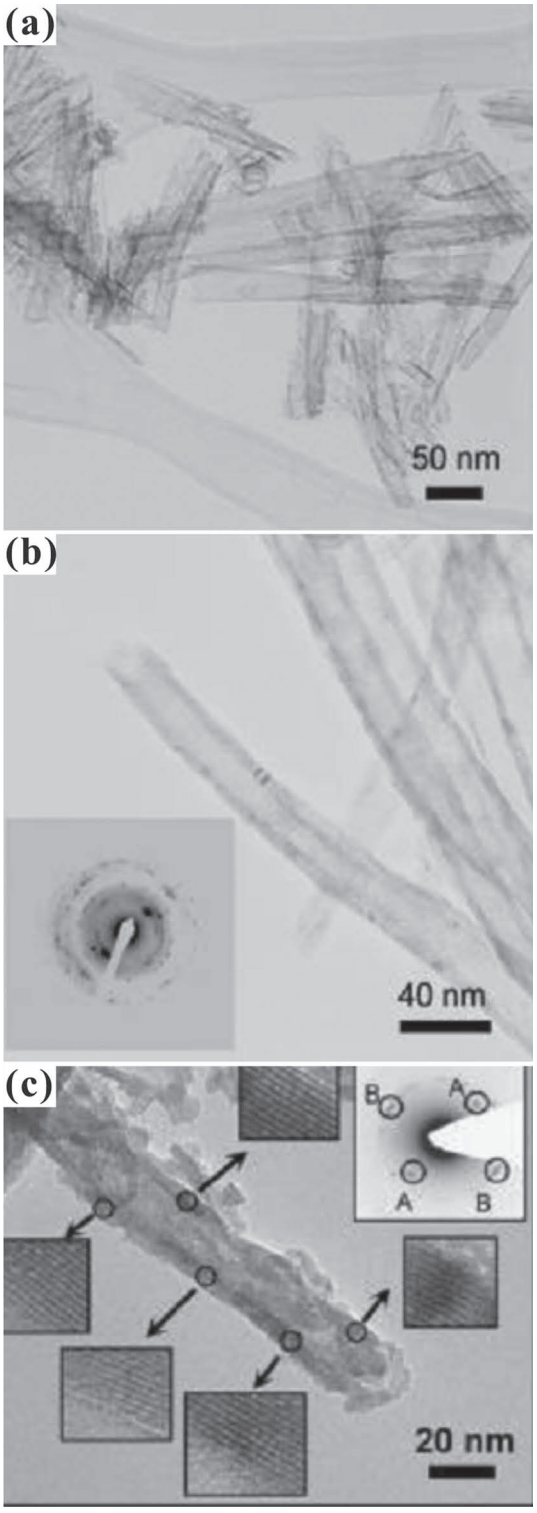

Figure 21. a–c) TEM images of 1D Nb_2O_5 nanotubes fabricated using a simple ambient synthetic route. The SAED and high-magnification TEM images are inset to (b) and (c). Reproduced with permission.[196] Copyright 2007, American Chemical Society.

walls, with aspect ratios of length to diameter of ≈50. Homogenous smooth side-wall TiO_2 nanotubes in large-scale arrays can be synthesized by suppressing local concentration fluctuations

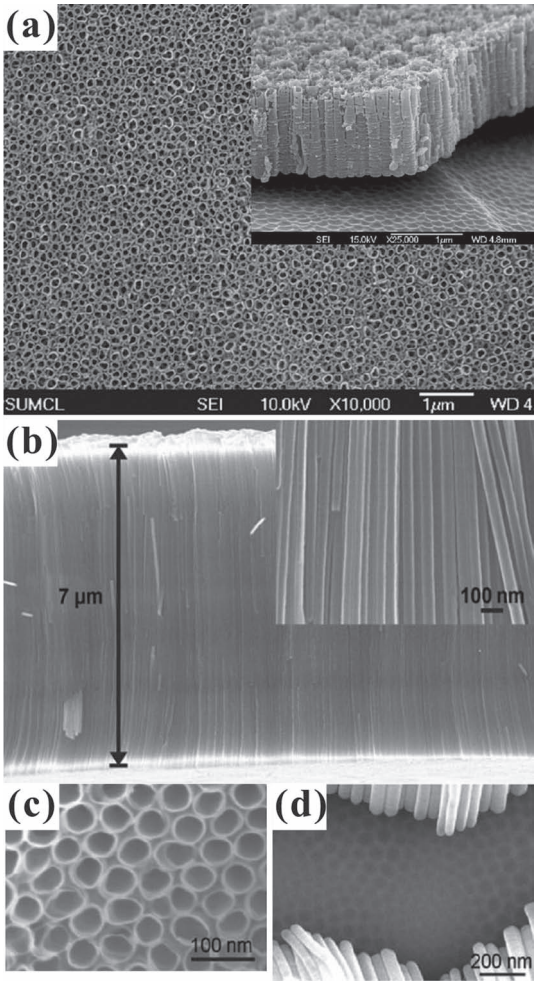

Figure 22. a) FESEM images showing the top and side views of large-scale arrays of highly-ordered TiO_2 nanotubes with irregular and rough side walls. Reproduced with permission.[200] Copyright 2006, Institute of Physics. b,c) FESEM images displaying the top and side views of large-scale arrays of highly ordered TiO_2 nanotubes with homogenous smooth side walls. d) FESEM image showing the convex and concave interface between the TiO_2 nanotubes and the underlying Ti substrate. Panels (b–d) reproduced with permission.[198] Copyright 2005.

and pH bursts during anodization by using a highly viscous glycerol electrolyte, so the aspect ratios of length to diameter increase to ≈175.[98] The FESEM images in Figure 22b,c also display the side and top views of highly ordered TiO_2 nanotubes arranged in the large-scale arrays with homogenous smooth side walls. The smooth side-wall TiO_2 nanotubes are ≈7 μm long and they are grown in very tight bundles that are not connected with another. The inner diameters of the TiO_2 nanotubes are mostly ≈40 nm. The FESEM image in Figure 22d demonstrates the interface between the TiO_2 nanotubes and the underlying Ti substrate.[198] The interface has many convex and concave markings on the surface. The growth of the TiO_2 nanotubes is strongly dependant on the convex areas. The side walls of the TiO_2 nanotubes grown on the convex areas.

The mechanisms for the growth of various TiO_2 nanotubes or tubular nanostructures are generally categorized into three kinds,[197] including the helical scrolling or wrapping of

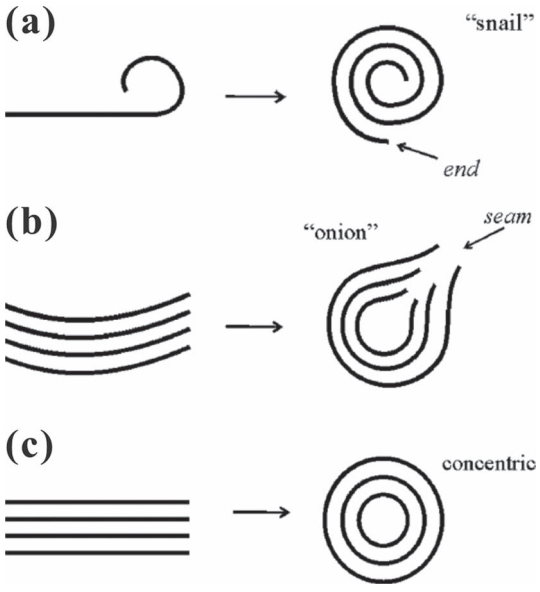

Figure 23. Three growth mechanisms: a) scrolling or wrapping single-layer nanosheets, b) curving and c) enclosing multilayer nanosheets. Reproduced with permission.[197] Copyright 2004, Royal Society of Chemistry.

single-layer TiO_2 nanosheets, the curving of multilayer nanosheets, and the enclosing of multilayer nanosheets. The schematic diagrams in **Figure 23** show the three growth mechanisms. Figure 23a displays the scrolling growth mechanism for TiO_2 nanotubes, as has been proposed for the formation of carbon nanotubes[216] and all layered-structure compounds.[180,196] When a single nanosheet is scrolled, a helical tubular nanostructure is formed similar to a "snail" structure with two ends. The TEM results reported in ref. [215] verify the helical tubular nanostructure. Figure 23b demonstrates the curving growth mechanism of the TiO_2 nanotubes. As multilayer nanosheets are curved, a seamy tubular nanostructure creates an "onion" structure. The TEM results reported in ref. [215] verify the seamy tubular nanostructure. Figure 23c illustrates the enclosing growth mechanism of the TiO_2 nanotubes. As multilayer nanosheets are enclosed, a concentric tubular nanostructure shaped like a "concentric-circle" structure forms. The TEM results reported in ref. [215] verify the concentric tubular nanostructure. According to the three growth mechanisms, we can figure out that the interactions between atoms in neighboring layers are less than those between atoms in the same layer in a layered-structure compound. During rapid growth the multilayers predominately grow at the edges, so that atomic mismatch and separations may occur between the multilayers. Also, the width and thickness of each individual single layer in the multilayers spontaneously varies from the others. The atomic mismatch, separations, and varying widths and thickness cause the tension imbalance in each individual single layer to decrease the layer tension energies. This induces the growth of the three kinds of tubular nanostructures.

4.7. Nickel Oxide Nanostructures

Nickel oxides with molecular formulas of NiO,[217–221] NiO_2,[222,223] and Ni_2O_3,[224,225] can be fabricated to have crystalline phases, such as cubic, monoclinic, rhombohedral, and hexagonal crystals. However, most nickel oxides form stoichiometric NiO. In fact, NiO is a rock-salt crystal (NaCl) with an antiferromagnetic structure with a six-fold octahedral coordination, and is an important *p*-type semiconductor with a wide bandgap of 3.6–4.0 eV.[226,227] As a consequence of their antiferromagnetic, p-type and wide-range properties, nickel oxides are excellent for use in Li-batteries,[217] antibacterial materials,[218,220] gas sensors,[221] memory devices,[228] supercapacitors,[229] etc. Varying techniques can be exploited to synthesize 1D nanorods,[220,226,230] nanowires,[219,221,228–231] nanotubes,[217–219,227,230] and nanofibers[232] of nickel oxides.

Manifold NiO hierarchical nanostructures, including mesoporous nanotubes, bundled nanowires, nanodandelions, and hollow nanospheres can be synthesized by an ambient simple hydrothermal and thermal decomposition process,[230] but it is still a challenge to control the morphologies of the hierarchical nanostructures by simply changing experimental parameters. FESEM and TEM images show the manifold NiO hierarchical nanostructures mentioned above. **Figure 24**a displays large-scale 1D NiO wire-like hierarchical nanostructures a few micrometers long and ≈100 nm wide. However, the TEM images in Figure 24b show the 1D wire-like hierarchical nanostructures to be uniform and ≈60 nm wide. The high-magnification TEM image in the inset to Figure 24b demonstrates one single 1D wire-like hierarchical nanostructure, verified to be composed of nanoparticles 5–15 nm wide. The TEM contrast between nanoparticles clearly reveals that the 1D wire-like hierarchical nanostructures possess quasi-tubular characteristic. The high-resolution TEM image in Figure 24c shows one individual NiO 15 nm wide nanoparticle. The interplanar separations between the lattice fringes are 0.21 nm, with the lattice fringes on the (200) planes of the face-centered cubic NiO crystals.

Large-scale 1D NiO nanotubes can be synthesized using a wet chemistry templating method.[218,227] As the Ni complex precursors undergo calcination in air, they are decomposed and formed into large-scale 1D NiO nanotubes. The FESEM images in **Figure 25**a show 1D NiO tubes a few micrometers long and ≈300 nm wide.[227] The surface morphology of the 1D NiO tubes is very rough, suggesting that the 1D NiO tubes are composed of NiO nanoparticles. The inner diameters of the 1D NiO tubes are ≈200 nm and the wall thickness is ≈50 nm thick. The TEM images in Figure 25b display the 1D NiO tubes exhibiting various appearances, such as branched, forked, capped, and uncapped features. However, the surface morphology is much smoother than that of the rough NiO tubes shown in Figure 25a. It can be seen in the high-magnification TEM image in the inset to Figure 25b that the diameter and wall thickness of a single NiO tube are ≈240 and 60 nm, respectively. The high-resolution TEM image in Figure 25c reveals that the NiO tubes are polycrystalline and that the walls of the NiO tubes are composed of NiO nanocrystals. The diameters of the NiO nanocrystals are 5–20 nm wide.

4.8. Zinc Oxide Nanostructures

Zinc oxides can be fabricated with the molecular formulas of ZnO[41,233–235] and ZnO_2,[236–238] with only two crystalline

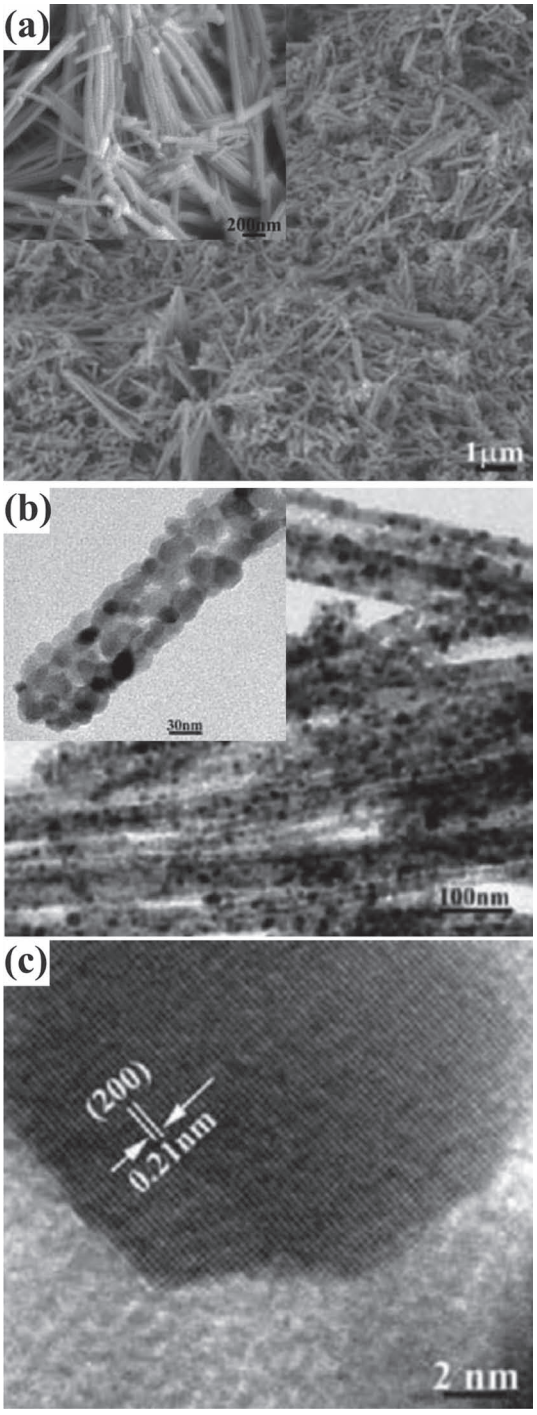

Figure 24. a) FESEM images of the large-scale 1D NiO nanowire-like hierarchical nanostructures. b) TEM images of the single 1D NiO nanowire-like hierarchical nanostructures. The inset to (b) shows nanowire-like nanostrcutures consisting of small nanoparticles. c) TEM image of a single nanoparticle. Reproduced with permission.[230] Copyright 2010, Royal Society of Chemistry.

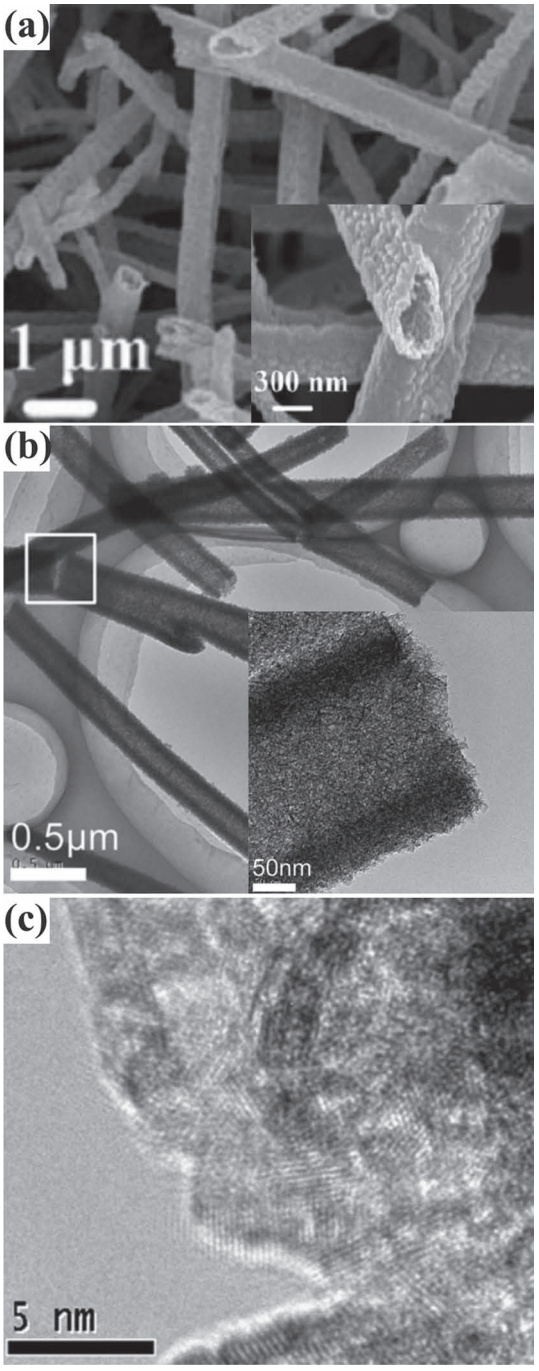

Figure 25. a) SEM images of the NiO nanotubes. Reproduced with permission.[218] Copyright 2009, Royal Society of Chemistry. b) TEM images of the NiO nanotubes. c) High-resolution TEM image of the polycrystalline structures of the NiO nanotubes. Reproduced with permission.[227] Copyright 2008, Elsevier.

phases, hexagonal and cubic crystals. However, ZnO shares three major crystalline structures of wurtzite, zinc-blende and rock-salt, respectively. Among the metal oxides, zinc oxides are the most functional materials used for many applications including in biosensors,[233] solar cells,[234] photocatalysis,[235,237] light-emitting diodes,[239,240] gas sensing,[241] and field-emission.[41,71] As known, the 1D nanostructures may enhance the functional properties for practical applications. In the quest for 1D nanostructures, zinc oxides can be formed into nanorods,[71,242] nanowires,[71,242–244] nanonails,[245] nanopencils,[245]

nanobullets,[246] nanotubes,[235,247,248] nanocomb-like structure,[234,249–251] nanoribbons,[250] nanobelts,[39,41,252] nanohelices,[252] nanopins,[253] nanoneedles,[249,254] etc.

The most distinctive feature among all kinds of nanostructures is the one with a belt-like morphology, called the nanobelt. The growth mechanism of the nanobelts is anisotropic but different from that of the nanowires, nanorods, and nanotubes. The nanobelts are an ideal material for fully comprehending the confinement effects on transport phenomena in functional metal oxides and building functional devices due to the reduction of size and dimensionality. In 2001, ultralong ZnO nanobelts were first successfully synthesized by simply evaporating ZnO powders at high temperatures.[39] The SEM and TEM images in **Figure 26**a show large-scale 1D ZnO nanobelts several hundreds of micrometers in length; some of them are even a few millimeters long. They have a rectangle-like cross section with widths of 30–300 nm and width-to-thickness ratios of 5–10. The as-synthesized ZnO nanobelts are pure, uniform, single crystalline structures almost free from defects and dislocations. The TEM image in the upper inset to Figure 26a reveals a single 1D ZnO nanobelt with a uniform width along its entire length. Note that the widths of the 1D ZnO nanobelts typically range from 50 to 300 nm, with no particles observed at the nanobelt ends. The body of the 1D ZnO nanobelt has a ripple-like contrast, which is caused by the strain resulting from the bending of the nanobelt. Electron diffraction shows that the 1D ZnO nanobelts are structurally uniform and single crystalline and grow along the [0001] direction. The other TEM image in the bottom inset to Figure 26a verifies that the typical thickness and width-to-thickness ratios of the ZnO nanobelts are in the range of 10 to 30 nm and ≈5 to 10, respectively. The TEM image in Figure 26b shows a single nanobelt, with ripple-like contrast resulting from the strain and thickness variations. The SAED pattern in the inset to Figure 26b reveals that the ZnO nanobelt is a hexagonal crystal that consists of the (0001) lattice planes and grows along the [0110] direction. The high-resolution TEM image in Figure 26c shows the lattice fringes of the (0001) plane. The lattice spacing is 0.52 nm. The clear atomic resolution image indicates that the ZnO nanobelts are highly crystallized without defects and dislocations.

The 1D ZnO nanobelts can be curled (or wound) to form uniform helix nanostructures, known as nanohelices. The 1D ZnO nanohelices were grown by a simple thermal evaporation method.[252] The TEM images in **Figure 27**a show various left- and right-handed freestanding 1D ZnO nanohelices on the substrate surface. These highly uniform 1D nanohelices are about 100 μm long and 100–500 nm wide with diameters and pitch distances of 300–700 nm and 500–2500 nm, respectively. The high-resolution TEM image in Figure 27b reveals the superlattices of the nanohelices to have a uniform periodic alternating arrangement of stripes with a periodicity of ≈3.5 nm. The stripes are nearly parallel to the growth direction and follow the length of the nanohelix with a 5° offset. The enlarged high-resolution TEM image in Figure 27c demonstrates the interface between the two adjacent stripes, here called Stripe I and II, of the superlattices of the nanohelices. The original imaging resolution is not very good, but can be simulated and improved using dynamic electron diffraction theory. The simulated image in the green dotted-line box in Figure 27c has better resolution.

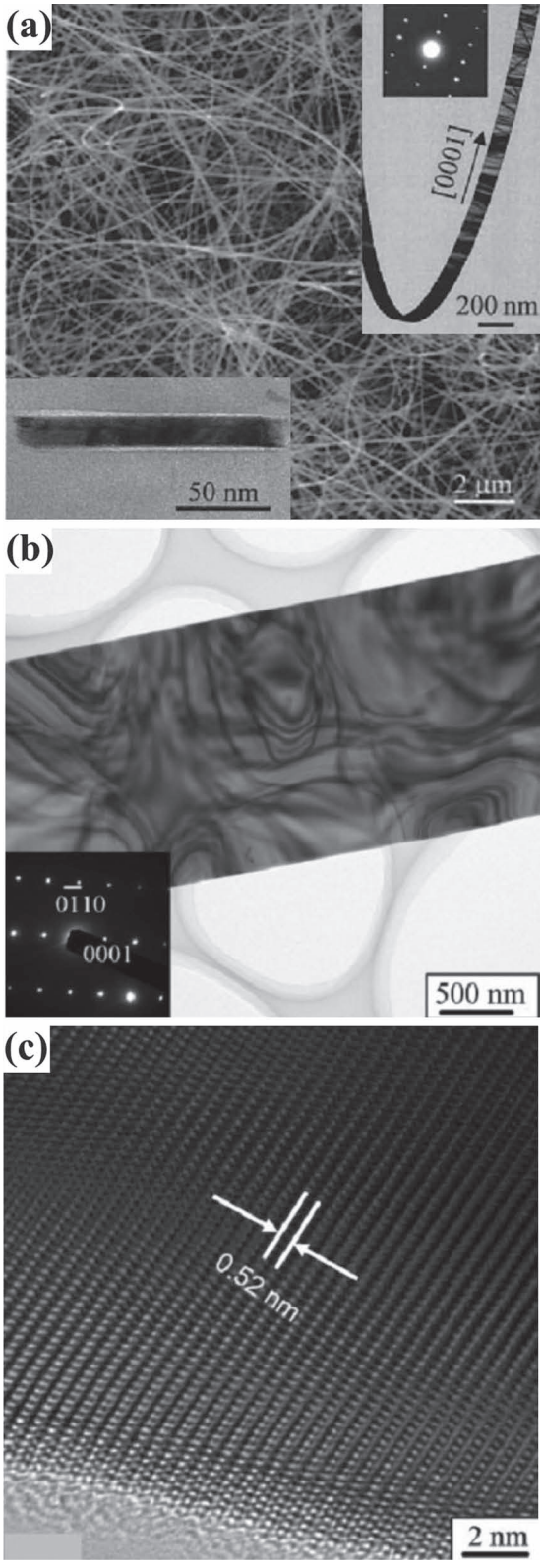

Figure 26. a) SEM and TEM images of ultralong 1D ZnO nanobelts. Reproduced with permission.[39] Copyright 2001, American Association for the Advancement of Science. b) TEM images of s single 1D ZnO nanobelt and c) high-resolution TEM images of the 1D ZnO nanoblts. Reproduced with permission.[41] Copyright 2006.

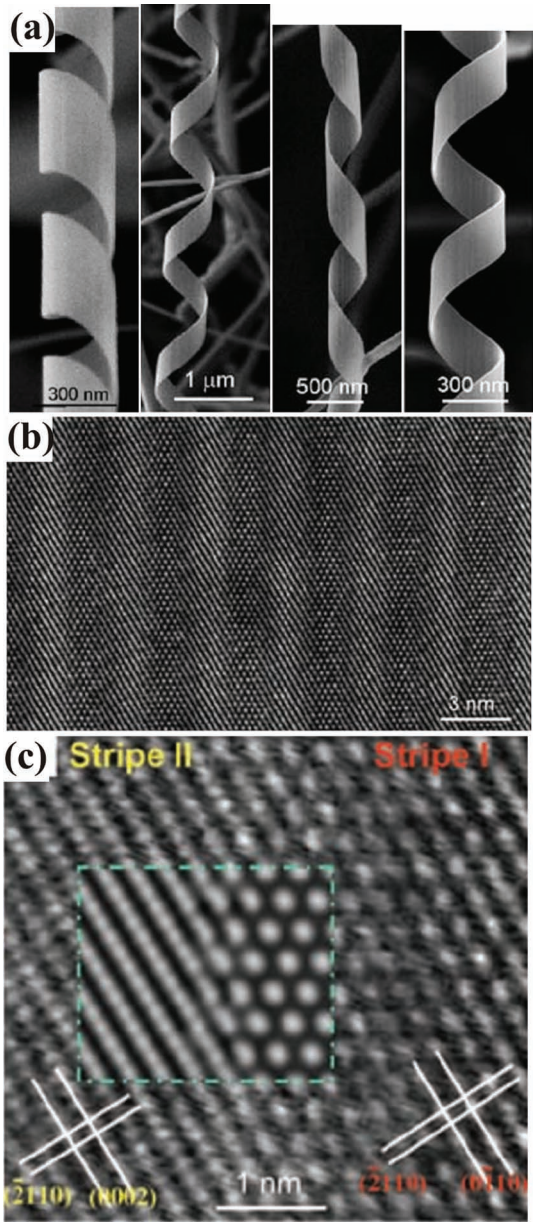

Figure 27. a) TEM images of ultralong left- and right-handed 1D ZnO nanohelices. b) High-resolution TEM image of two periodic alternating stripes of the superlattices of the nanohelices. c) Enlarged high-resolution TEM image of the interface between the two adjacent stripes. The simulated image is shown in the green dotted-line box. Reproduced with permission.[252] Copyright 2005, American Academy for the Advancement of Science.

The interface is inclined with respect to the incident electron beam at an angle of 32°.

4.9. Bismuth Oxide Nanostructures

Synthesized bismuth oxides can have varying chemical forms, including stoichiometric Bi_2O_3[42,99,255,256] and Bi_2O_4,[257,258] and non-stoichiometric Bi_4O_7[257] and $Bi_2O_{2.33}$,[259] and possess a variety of crystalline phases, including monoclinic, tetragonal, cubic, triclinic, and hexagonal crystals. The bismuth oxides are also one of the most attractive functional materials among the metal-oxides due to their unique physical and chemical properties such as supercapacitance,[260] intense photoluminescence,[42,99] and wide bandgap (2.58-3.9 eV).[261,262] In the quest for a 1D morphology, various synthesis techniques can be used to form nanohooks,[42] nanobelts,[260] nanotubes,[261–264] and nanowires[99,255,265,266] of bismuth oxides.

Large-scale 1D Bi_2O_3 nanowires can be synthesized at low temperature using a simple oxidation method, the HFMOVD technique.[99] The FESEM images in **Figure 28**a show a large-scale array of 1D Bi_2O_3 nanowires. These nanowires are highly entangled and stacked with spherical and tadpole-head-like nanoparticles at the ends. These 1D Bi_2O_3 nanowires are several tens of micrometers long and 13–42 nm wide. The high-magnification FESEM in the inset to Figure 28a demonstrates the clear features of the spherical and tadpole-head-like nanoparticles. The spherical and tadpole-like nanoparticles are about 45–140 nm in diameter. Large-scale 1D Bi_2O_3 nanohooks can be also synthesized by the HFMOVD technique.[42] The FESEM images in Figure 28b show a random arrangement of large-scale 1D Bi_2O_3 nanohooks. The high-magnification FESEM image in the inset to Figure 28b reveals four distinct growth regions: i) nanoparticles 20–100 nm in diameter at the tip (marked by 1); ii) hook-like nanostructures (marked by 2); iii) cone-like structures (marked by 3); and iv) uniform nanowires (marked by 4). There are also two joints, one between the cone-like and nanowire-like region (marked by A), and the other between the two nanowire-like regions of different widths (marked by B). The TEM images and SAED pattern in Figure 28c display three single nanohooks, with widths ranging from 160 to 440 nm. There are clear lattice fringes separated by 0.322 nm, which agrees with the interplanar spacing corresponding to the (201) lattice plane, indicating the 1D Bi_2O_3 nanohooks to be crystalline and to grow along the (101) direction.

Arrays of 1D bismuth nanowires can be converted into 1D bismuth and bismuth-oxide core-shell nanowires and bismuth nanotubes by using a template-based heat-treatment method.[262] The FESEM and TEM images in **Figure 29**a show the 1D Bi nanowires arranged in large-scale arrays to be ≈60 nm wide. The high-magnification TEM image and SAED pattern reveal that the 1D Bi nanowires are single crystalline and grow along the [110] direction. The FESEM and TEM images in Figure 29b display 1D Bi-Bi_2O_3 core-shell nanowires arranged in large-scale arrays. The high-magnification TEM image and SAED pattern clearly reveal the single 1D Bi-Bi_2O_3 core-shell structure grow along the [110] direction. Obviously, the core of the single nanowire is still only composed of Bi, indicating the Bi nanowires are preserved in the cores after thermal oxidation. The FESEM and TEM images in Figure 29c show the 1D Bi_2O_3 nanotubes arranged in the large-scale arrays to be ≈75 nm wide. It can be seen in the high-magnification TEM image that the Bi nanowires in the cores are easily etched in a NaOH solution by a two-step oxidation process. The results provide the possibility of synthesizing 1D solid and core-shell nanowires and tubular nanostructures spontaneously with the same deposition technique, which has potential for use in many nanodevices.

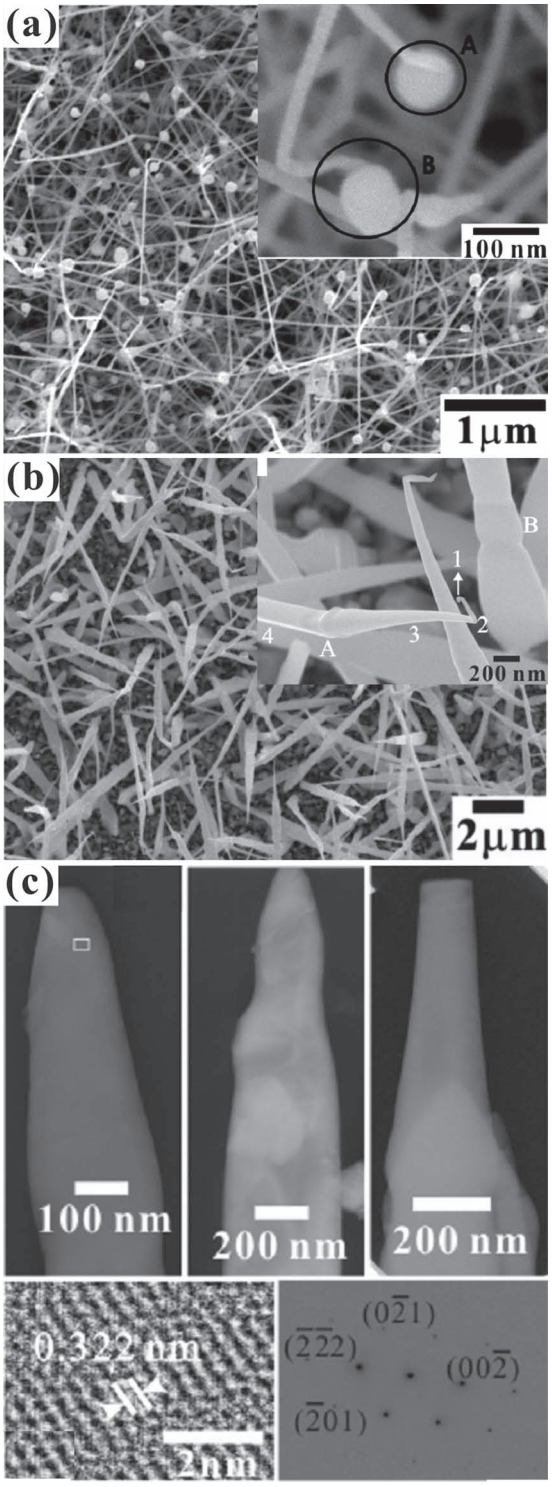

Figure 28. a) FESEM images of large-scale array of the 1D Bi_2O_3 nanowires with spherical and tadpole-head-like nanoparticles at the ends. The inset clearly shows the spherical and tadpole-head-like nanoparticles, which are marked by A and B. Reproduced with permission.[99] Copyright 2007, Institute of Physics. b) FESEM images of the 1D Bi_2O_3 nanohooks. c) TEM images and SAED pattern of the 1D Bi_2O_3 nanohooks. Reproduced with permission.[42] Copyright 2007, Institute of Physics.

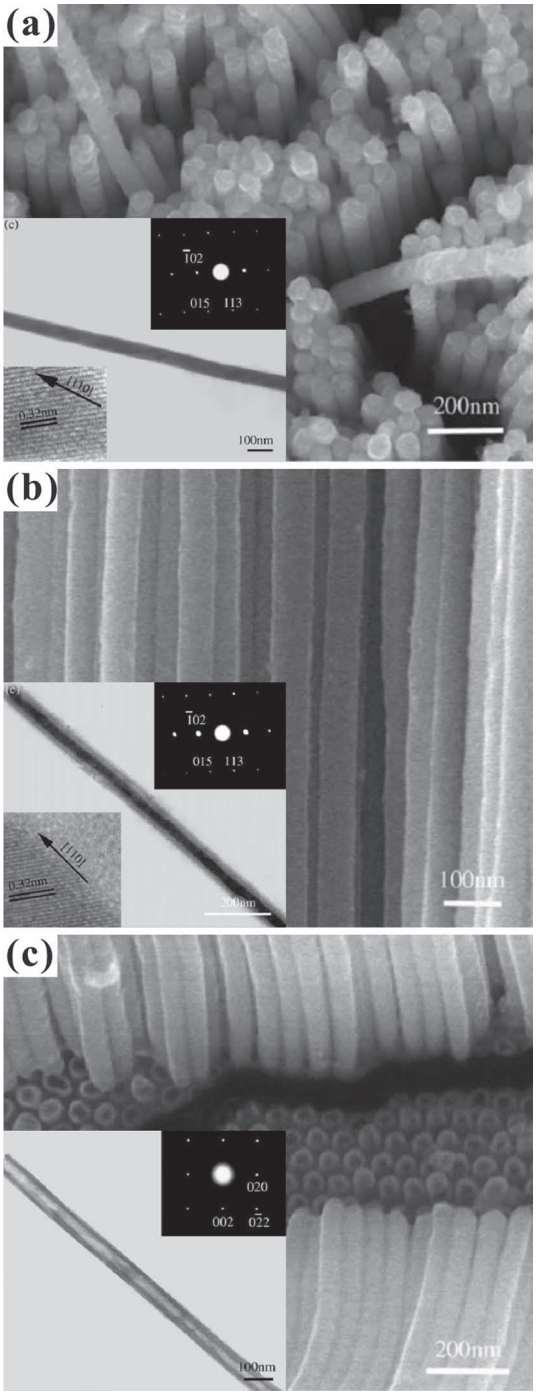

Figure 29. FESEM and TEM images and SAED patterns of a) the Bi_2O_3 nanowires, b) Bi- Bi_2O_3 core-shell nanowires, and c) Bi_2O_3 nanotubes. Reproduced with permission.[262] Copyright 2006.

4.10. Tin Oxide

Tin oxides with various chemical forms can be synthesized, including SnO_2,[267–271] SnO,[272–274] Sn_2O_3[275] and Sn_3O_4,[275] with a variety of crystalline phases, such as orthorhombic, tetragonal, cubic, and triclinic crystals. Among the metal-oxides, tin oxide has attracted the most scientific attention because of

its excellent properties, which make it suitable for use in optoelectronic devices,[271] field emitters[276] and gas sensors.[277] SnO_2 doped with indium is used to make the renowned conductive transparent glass, indium tin oxide (ITO), which can be utilized for many applications, such as in optoelectronic and electrochromic devices. In quest for a 1D morphology, tin oxides are synthesized in the form of nanorods,[267,276–278] nanowires,[270,279] nanobelts,[280] zigzag nanobelts,[268,281] nanoribbons,[282,283] nanotubes,[269,284] etc.

Large-scale 1D SnO_2 nanorods/nanowires can be synthesized by the vapor-liquid-solid process with an Au catalyst at high temperatures.[278] The FESEM images in **Figure 30**a show large-scale arrays of 1D SnO_2 nanorods ≈20 μm long. The high-magnification FESEM in the inset to Figure 30a clearly shows the beaklike nanostructures at the ends of the 1D SnO_2 nanorods. The 1D SnO_2 nanorods are uniform in size and 85–400 nm wide. The beaklike nanostructures are 100–700 nm long, indicating a change in the growth direction. The TEM images and SAED pattern in Figure 30b illustrates a single 1D SnO_2 nanorod that is 85 nm wide with a beaklike nanostructure at the end. The SAED pattern verifies that the beaklike nanostructure is the tetragonal rutile structure. The high-resolution TEM image discloses that the nanorods are single crystalline and free of defects. The two *d*-spacings of 0.33 and 0.23 nm can be clearly seen, suggesting the two growth directions. The FESEM images in Figure 30c show 1D SnO_2 nanorods with no beaklike nanostructures, but rather Au catalyst nanoparticles. The inset to Figure 30c reveals a single 1D SnO_2 nanorod with an Au catalyst nanoparticle at the end. The Au catalyst nanoparticle is obviously larger in size than the width of the 1D SnO_2 nanorod. The different nanomaterials and morphologies at the ends imply the Au catalyst may be deposited at the ends of the nanorods or on the substrate surface. When the Au catalyst is at the ends of the nanorods, they form into nanoparticles. However, when the Au catalyst is on the substrate surface, beaklike nanostructures form at the ends of the nanorods which are the beginning of growth for the 1D SnO_2 nanorods.

Much effort has been made for the preparation[39,280] and application[40,69] of SnO_2 nanobelt-based structures. Peculiar 1D nanobelt-based SnO_2 nanozigzags can be synthesized by oxidizing Sn grains in an ambient atmosphere at high temperature.[268] The SEM images in **Figure 31**a show the morphology of the 1D SnO_2 nanozigzags consisting of periodic nanobelts arranged in a zigzag structure. The widths and thickness of the 1D SnO_2 nanozigzags are 100–1000 and 30–80 nm, respectively. The longest SnO_2 nanozigzag can be larger than 0.5 mm and the repeating lengths are 2–8 μm. The SnO_2 nanobelts form the SnO_2 zigzag nanostructure by alternate growth along two different equivalent directions. The high-magnification SEM images in the inset to Figure 31a clearly display a single 1D SnO_2 zigzag nanostructure with a periodic nanobelt arrangement. There are alternate growth directions with a periodic length between two adjacent nanobelts of ≈2.5 μm. The 1D SnO_2 zigzag nanostructure is quite uniform and stable because the width, thickness, and the angle of the SnO_2 nanobelts are almost invariable throughout. However, the periods of the 1D SnO_2 zigzag nanostructures vary as the lengths of the nanobelts increase or decrease. The TEM image in Figure 31b displays a single 1D SnO_2 zigzag nanostructure with a ripple-like contrast

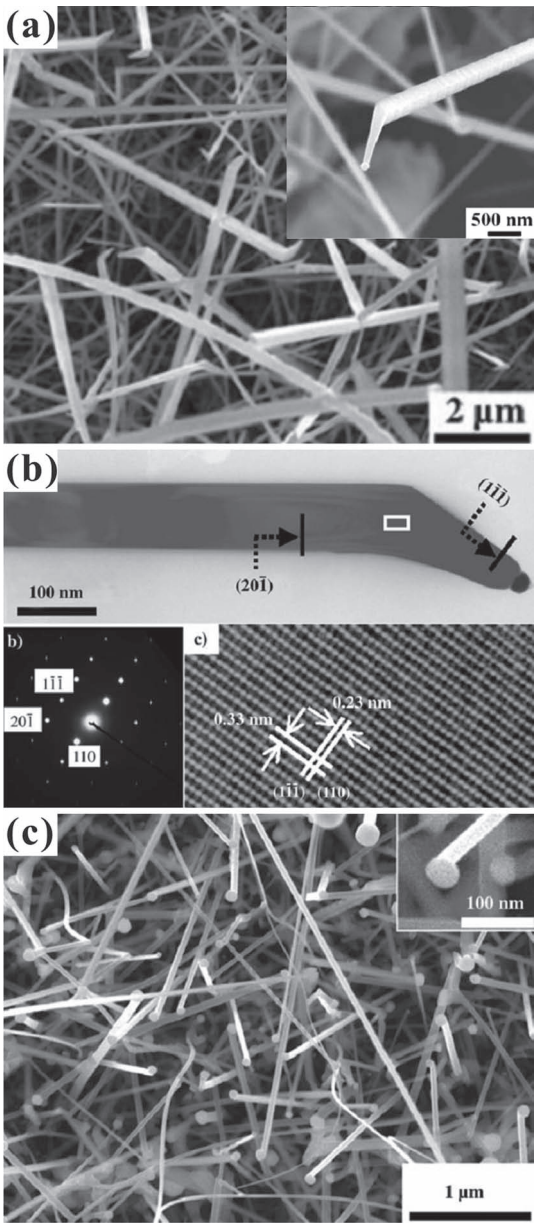

Figure 30. a) FESEM images of the large-scale array of the 1D SnO_2 nanorods with beaklike nanostructures at the ends. b) TEM images and SAED pattern of a single 1D SnO_2 nanorod with a beaklike nanostructure. c) FESEM images of the large-scale array of the 1D SnO_2 nanorods with the Au catalyst nanoparticles. Reproduced with permission.[276] Copyright 2006.

through the whole body. The nanobelts are less than 100 nm thick. The two growth directions are revealed in the SAED pattern (see the white box) in the inset to Figure 31b. The angle between the growth directions is 68.43 °. The high-resolution TEM image in Figure 31c illustrates the clear lattices fringes of the 1D SnO_2 zigzag nanostructure and two *d*-spacings of 0.267 and 0.235 nm, which reflect the (101) and (200) lattice planes of the tetragonal SnO_2 crystals, respectively. The SAED pattern and high-resolution TEM image verify the two growth directions (see Figure 31c).

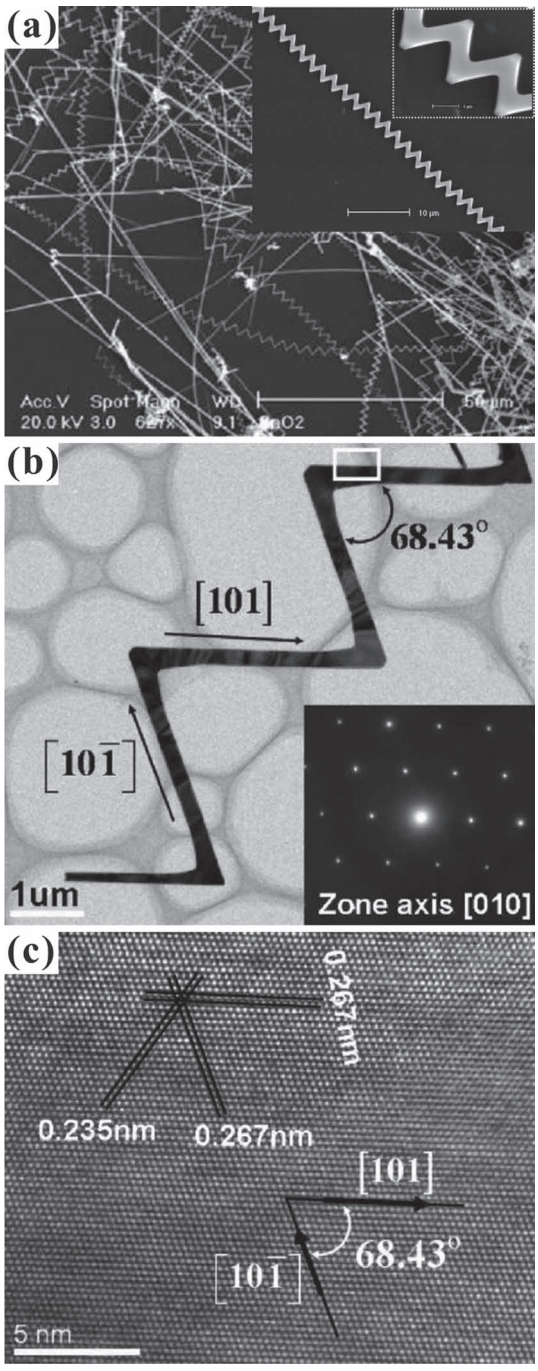

Figure 31. a) SEM images of the 1D SnO_2 zigzag nanostructures consisting nanobelts. b) TEM image and SAED pattern of a single 1D SnO_2 zigzag nanostructure. c) High-resolution TEM image of 1D SnO_2 zigzag nanostructure. Reproduced with permission.[268] Copyright 2005, American Chemical Society.

5. Various 1D Metal-Oxide Nanostructure-Based Applications

Various 1D metal-oxide nanostructures have been used as building blocks for many applications in nanoscience and nanotechnology because they have fascinating properties that are better than those of bulk metal-oxides. In this section, we introduce some recent work on 1D metal-oxide nanostructure-based devices.

5.1. Gas Sensors

A gas sensor is a mechanism for detecting gases in the atmosphere. Since many gases are harmful to human being or animals, methods of gas sensing are developed as a part of a safety system. The mechanism involves the adsorption of active gases on the surfaces of the functional materials that cause change in the electrical conductivity. The functional materials for gas sensing are mainly metal-oxides because the oxygen sites in their surfaces provide the possibility of gas adsorption. Gas sensors are used to detect combustible, flammable and toxic gases, and to monitor oxygen depletion. The 1D metal-oxide nanostructures have a high surface-to-volume ratio, meaning they can provide a much larger surface area than the 2D metal-oxide thin films, which makes them more sensitive for gas sensing. Up to the present time, 1D metal-oxide nanostructures of $W_{18}O_{49}$,[285] W_2O_5,[285] SnO_2,[40] VO_2,[286] ZnO,[287] MoO_3,[146] and In_2O_3[288] have been widely used for gas sensing. Many gas species such as hydrocarbon liquefied petroleum gas,[285] O_2,[40,289] H_2,[40,286] D_2,[286] ethanol,[243,287,290,291] NH_3,[146] NO_2,[146,292,293] CH_4,[289] CO,[291,294] and isobutane[295] can be detected. Measurement techniques commonly involve changes in the conductivity and resistivity of the materials due to the presence of gas. However, the gas sensitivity can be enhanced because of the large surface area and the morphology of the 1D metal-oxide nanostructures.[291,296] The smaller the size of the 1D metal-oxide nanostructures, the higher the gas sensitivity will be. Below, we display significant results obtained with 1D metal-oxide nanostructure-based gas sensors.

Gas sensors fabricated with ZnO nanorod arrays possess high gas sensitivity to H_2 at a variety of temperatures from room temperature to 250 °C with a detection limit of 20 ppm.[296] The 200-ppm-H_2 gas sensitivity of 1D ZnO nanorods ≈50 and 500 nm in diameter can reach values of 8.5 and 1.9, respectively, at 250 °C, indicating the higher gas sensitivity of the smaller 1D ZnO nanorods. Very small SnO_2 nanorods ≈3 nm in diameter can give ultrahigh gas sensitivity for detection of ethanol, a sensitivity of up to 83.8 at 300 ppm ethanol vapor in air.[297] In addition, the gas sensing results[295] show that gas sensitivity is strongly dependent on the diameters of the ZnO nanowires, as shown in **Figure 32**. As discussed above, the smaller the sizes of the 1D metal-oxide nanostructures, the higher the gas sensitivity. Similarly, for light gases, such as H_2, the smaller 1D ZnO nanowires have higher gas sensitivity. For the heavy isobutene gas, higher gas sensitivity is obtained with larger 1D ZnO nanowires. In addition, many metal-oxide nanostructure-based gas sensors, such as the ZnO nanowire-based gas sensors[295] (for detecting H_2, NH_3, isobutene, and CH_4 gases) and the $W_{18}O_{49}$ nanorod-based gas sensors[298] (for ethanol, NH_3, and NO_2 gases), operate well at room temperature with high gas sensitivity. In fact, to acquire optimal sensitivity, most gas sensors are normally operated at high temperatures above room temperature. External heating systems are needed to increase the working temperatures of the gas sensors. However,

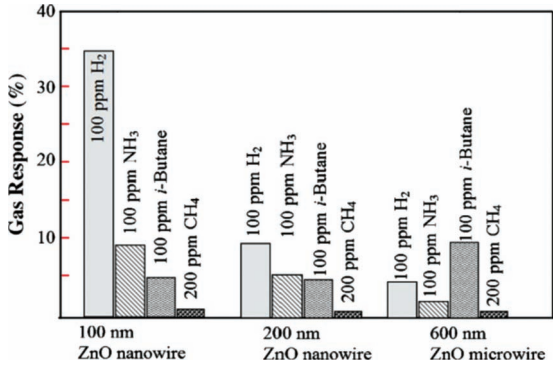

Figure 32. Gas responses of various diameter ZnO nanowire-based gas sensors for H_2, NH_3, isobutene, and CH_4 gases. Reproduced with permission.[295] Copyright 2010, Elsevier.

gas sensors based on the 1D SnO_2 nanowires can operate at high temperatures without external heating systems.[292] This is because the 1D SnO_2 nanowires are self-heated by a dc power applied to the two terminals of the nanowires. The two-terminal method[286,292] involves the metal-insulator transition for the gas sensing of the 1D metal-oxide nanostructures.

A gas sensor device comprised of a single SnO_2 nanowire and two Pt-SnO_2 Schottky contacts is shown in **Figure 33**a. The nanowire and the two Schottky contacts dissipate the applied electrical power to generate heat. Obviously, the more power applied, the higher the temperature. The graphs in Figure 33b show that the self-heating SnO_2 nanowire-based gas sensors behave the same as the SnO_2 nanowire-based gas sensors with external heaters for NO_2 gas of 0.5 ppm. It is important that gas sensors perform well, not only with self-heating but also in humid atmospheres. The single SnO_2 nanowire-based gas sensor can be operated to obtain high gas sensitivity in various humid atmospheres.[299] The responses and recovery times of this SnO_2 humidity sensor are only 120–170 and 20–60 s when the relative humidity of the air is 5 and 85%, respectively. The resistance of the single SnO_2 nanowire promptly decreases as the relative humidity of the air increases. The resistance of the SnO_2 NW in dry air (5%) is calculated to be ≈14 times greater than that when the relative humidity is 48%, and ≈32 times greater than that when the relative humidity is 85%. Obviously, water vapor in the air has a strong influence on the conductivity of a single SnO_2 nanowire. In addition, a bundle of 1D $W_{18}O_{49}$ nanowires can be fabricated for gas sensors.[293] They can also be operated in humid air and the gas sensitivity for 50 ppb of NO_2 can reach ≈9 at room temperature in humid air. The advantages of the single-nanowire gas sensors include self-heating, working at room temperature, and operating in humid atmospheres.

Nanobelts offer larger surface areas than other nanostructures such as nanorods and nanowires because of their higher surface-to-volume ratios. The 1D SnO_2[294] and V_2O_5[175] nanobelt-based gas sensors are highly sensitive and stable for environmental polluting gases such as CO and NO_2, as well as for ethanol for exhalation analyzers. For example, the sensor responses are 41.6 for 250 ppm for ethanol and –15.5 for 0.5 ppm NO_2 at 400 °C.[294] In addition, the gas sensitivity of the metal-oxide nanostructure-based gas sensors can be improved

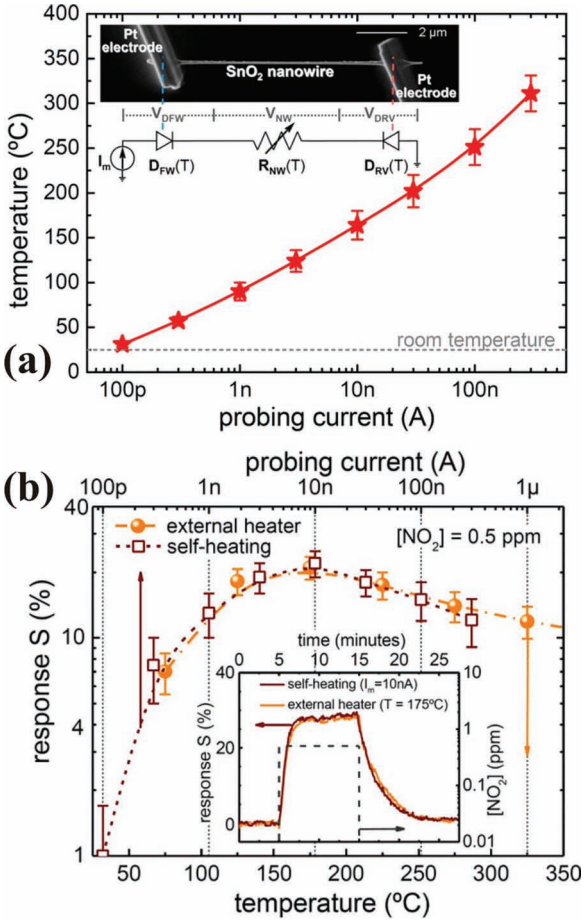

Figure 33. a) Probing current versus working temperature of the single SnO_2 nanowire gas sensors. The SEM image in the inset shows a single SnO_2 nanowire connected to two Pt microelectrodes. The equivalent circuit corresponds to two Pt/SnO_2 contacts connected in series with a single nanowire. These three components dissipate electrical power and contribute to the self-heating of the device. b) The responses of the single SnO_2 nanowire-based gas sensor operated in self-heating mode with an external heater for 0.5 ppm NO_2. The inset shows the response versus time. Reproduced with permission.[292] Copyright 2008, American Institute of Physics.

with extrinsic Pd nanoparticles.[40,286,300] This is because the Pd nanoparticles on the nanowire surface create Schottky barrier-type junctions between the Pd nanoparticles and the metal-oxide nanostructures. These junctions result in the formation of electron depletion regions within the metal-oxide nanostructures so that the the effective conduction channel and the conductance are constricted and reduced, respectively. There is a dramatic improvement in the gas sensitivity due to the enhancement of the catalytic dissociation of the molecular adsorbate on the surfaces of the Pd nanoparticles and the subsequent diffusion of the resultant atomic species to the oxide surface.[40] The catalytic activities of the Pd nanoparticles greatly increase the quantity of oxygen to repopulate the oxygen vacancies on the surface of the 1D metal-oxide nanostructures. In brief, the 1D metal-oxide nanostructures offer many advantages for their use in gas sensors as mentioned above, so that in future, gas sensors will

be fabricated with 1D metal-oxide nanostructures rather than thin films.

5.2. Electrochromic Devices

Metal-oxides have attracted considerable attention due to their electrochromic characteristics. Many of these metal-oxides, such as WO_3, V_2O_5, and NiO, are excellent electrochromic materials. Their optical properties reversibly and persistently change with the intercalation and deintercalation of cations, such as H^+, Li^+, Na^+, and K^+, due to the application of an external electric field. It is known that H^+ ions are smaller than Li^+ ions and the chemical diffusion coefficient of H^+ ions is an order of magnitude larger than that of Li^+ ions. This suggests that the switching response in acidic electrolytes will be faster than that in lithium-based electrolytes. The metal oxides are good for electrochromic materials because they can endure acidic electrolytes without degradation. As the cations are intercalated or deintercalated into the surfaces of the electrochromic materials, the surfaces become colored or bleached (or vice versa). If more cations remain on the surface, the color changes more. In other words, greater surface area provides more space for cations, so in contrast with thin films, the 1D metal-oxide nanostructures are a good candidate for electrochromic applications. The 1D nanostructures offer the advantages of larger surface area and more capillary pathways for ion intercalation and deintercalation. In fact, 1D metal-oxide nanostructures, including Ta_2O_5,[58] WO_3,[57,301,302] NiO,[303] MoO_3,[304] V_2O_5,[305,306] and TiO_2,[214,307] have already been used in electrochromic devices. These electrochromic devices are based on three-electrode cells composed of a working electrode, a counter electrode, and an independent saturated calomel electrode. **Figure 34** shows a schematic representation of a typical 1D metal-oxide nanostructure-based electrochromic device, which is composed of transparent 1D metal-oxide nanostrcuture arrays fabricated on a conducting ITO-thin-film-coated glass, an electrolyte, and another conducting ITO-thin-film-coated glass.

WO_3 is one of the electrochromic materials that which has been extensively studied. However, amorphous WO_3 can only be exploited in lithium-based electrolytes because the structure is not compact and the dissolution rate is not high in acidic electrolyte solutions. Crystalline WO_3 can be used in acidic electrolytes due to the comparable coloration efficiency and high stability compared to amorphous WO_3.[308] 1D crystalline WO_3 nanorods can be synthesized by a facile wet-chemical process without sulfates as capping agents[57,301] to construct WO_3 nanorod-based electrochromic devices consisting of cation electrolytes and conducting ITO-thin-film-coated glass. The cation electrolytes can be composed of a Li^+ aqueous solution of 1.0 M lithium perchlorate ($LiClO_4$) in propylene carbonate (PC),[57] or an H^+ aqueous solution of 0.5 M H_2SO_4.[301] The photographs in **Figure 35**a show the electrochromic phenomena of the WO_3 nanorod-based electrochromic devices with an Li^+ ion electrolyte and conducting ITO-thin-film-coated glass.[57] The WO_3 nanorod-based electrochromic device is transparent, suggesting that the WO_3 nanorods are also transparent. When a voltage of –1.0 V was applied, the WO_3 nanorod-based electrochromic device immediately turned green. The WO_3 nanorod-based electrochromic device first became blue and then deep blue, as the voltage decreased to –2 and –3 V. The deep blue color could remain for several days after the applied voltage was removed. A voltage of 3 V was applied to bleach out the deep blue color, after which the WO_3 nanorod-based electrochromic device became transparent again.

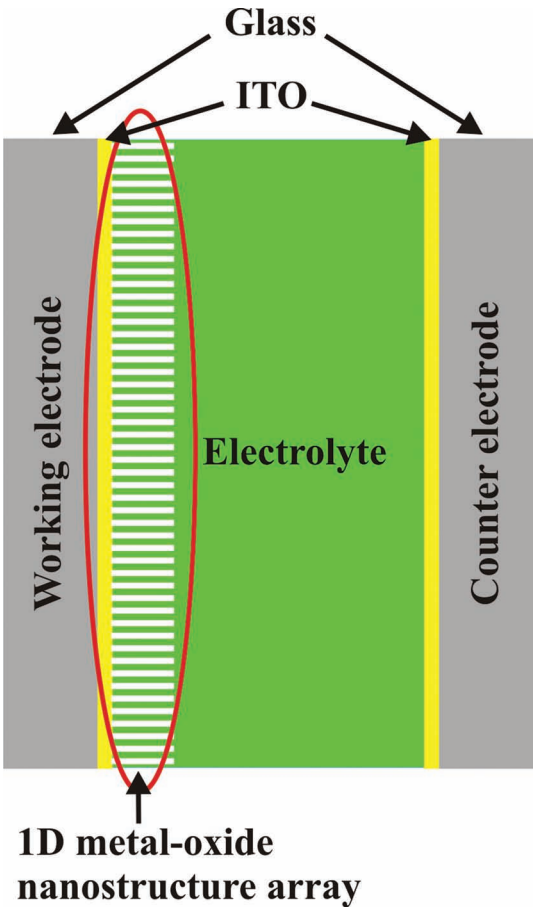

Figure 34. Schematic diagram of the 1D metal-oxide nanostructure-based electrochromic device. Reproduced with permission.[58] Copyright 2011, American Institute of Physics.

The transmittance spectra shown in Figure 35b display the optical transmittance of The WO_3 nanorod-based electrochromic device at applied voltages of 0, –1, –2, –3 and 3 V, respectively. The transmittances obtained at applied voltages of –1, –2, and –3 V are obviously lower than those obtained at 0 and 3 V. The maximum transmittances of the spectra taken at applied voltages –1, –2, and –3 V are located at ≈533, 512, 228 nm, respectively, verifying that the WO_3 nanorod-based electrochromic devices become green, blue, and deep blue at these applied voltages. All the transmittances at 632.8 nm were selected to characterize the electrochromic properties of the WO_3 nanorod-based electrochromic devices. The optical transmittance difference ($\Delta T \equiv T_{bleached} - T_{colored}$) between the colored-state (applied voltage of –3 V) and bleached-state (applied voltage of +3 V) at the wavelength of 632.8 nm are ≈66%, which is a relatively large value. Obviously, the large ΔT gives the WO_3-nanorods/ITO thin-film the potential for use in electrochromic devices. The $T_{colored}$ and

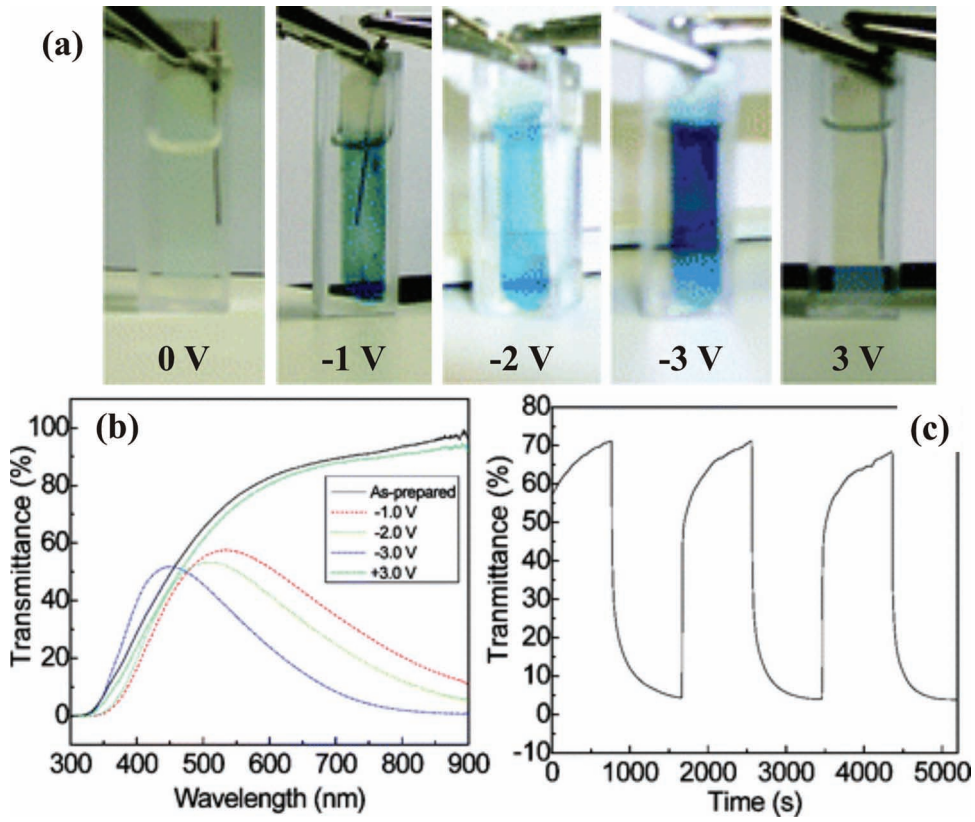

Figure 35. a) Photographs of electrochromic properties of the 1D WO_3 nanorods in the $LiClO_4$ electrolyte at 0, –1, –2, –3, and 3 V. b) Transmittance spectra recorded for applied voltages of 0, –1, –2, –3, and 3 V. c) The colored-bleaching cycles. Reproduced with permission.[57] Copyright 2008, American Chemical Society.

$T_{bleached}$ are selected as the transmittance references for the coloration-bleaching cycles. The transmittance graph in Figure 35c shows three coloration-bleaching cycles, which vary as a function of time within 5000 s for the WO_3-nanorods/ITO thin-film. The transmittance curves are repeated and alternate between the $T_{colored}$ and $T_{bleached}$. The switching responses, including the coloration (t_c) and bleaching (t_b) times, are very crucial to the performance of the electrochromic devices. Shorter switching responses represent better performance in the electrochromic devices. The switching response can be determined as the time required for 50, 70, and 90% changes in ΔT. In this study, the $t_{c(50\%)}$ and $t_{b(50\%)}$, $t_{c(70\%)}$ and $t_{b(70\%)}$, and $t_{c(90\%)}$ and $t_{b(90\%)}$ of the electrochromic WO_3-nanorods/ITO thin-film are 13 and 8 s, 38 and 42 s, and 272 and 364 s, respectively.

The FESEM image in **Figure 36**a illustrates a portion of the large-area high-density 1D Ta_2O_5 nanorods on the conducting ITO thin film, verifying that the high-density 1D Ta_2O_5 nanorods are homogeneously fabricated in a large-area array. The photograph inset to Figure 36a shows the transparency of large-scale 1D Ta_2O_5 nanorods synthesized on the conducting ITO thin film coated on glass. The 1D Ta_2O_5 nanorods are very compact, but the textural boundaries are clearly visible. The array contains ≈1900 Ta_2O_5 nanorods per square micrometer. Cyclic voltammogram (CV) measurement is an excellent method to examine the electrochromic effect with the double-charge (protons and electrons). Figure 36b shows a CV graph of the 1D Ta_2O_5 nanorods on the ITO thin-film (Ta_2O_5-nanorods/ITO thin-film). The forward scan is from 900 to –1000 mV, while the reverse scan is from –1000 to 900 mV. The arrows represent the forward and reverse scans, respectively. During the forward scan, Li^+ ions become intercalated in the 1D Ta_2O_5 nanorods. The transparent Ta_2O_5-nanorods/ITO thin films become somewhat yellowish at –200 mV, but turn a deep blue color at –550 mV. The larger the negative potential applied across the Ta_2O_5-nanorods/ITO thin film, the more Li^+ ions are easily intercalated into the Ta_2O_5 nanorods. However, the Ta_2O_5-nanorods/ITO thin-film retains consistently deep blue in color until the end of the coloration process. As the reverse scan begins, the deep blue color of the Ta_2O_5-nanorods/ITO thin-film gradually bleaches out. The Ta_2O_5-nanorods/ITO thin-film becomes completely transparent again at negative potentials of –100 mV, implying that the smaller the negative potential that is applied, the greater the number Li^+ ions that are deintercalated in the β-Ta_2O_5 nanorods. The two photographs inset to Figure 36b illustrate the colored and bleached states of the Ta_2O_5-nanorods/ITO thin-films. The large diffusion coefficient for the Li^+ ion diffusion in the large-area high-density 1D Ta_2O_5 nanorod arrays is ≈2.35×10^{-8} cm^2 s^{-1}, as calculated by the Randles–Servick equation,[309] indicating that the large-area high-density 1D Ta_2O_5 nanorod arrays are fast enough for electrochromic devices.

The reversibility of the coloration and bleaching corresponds to the change in the number of Li^+ ions in the electrolyte.

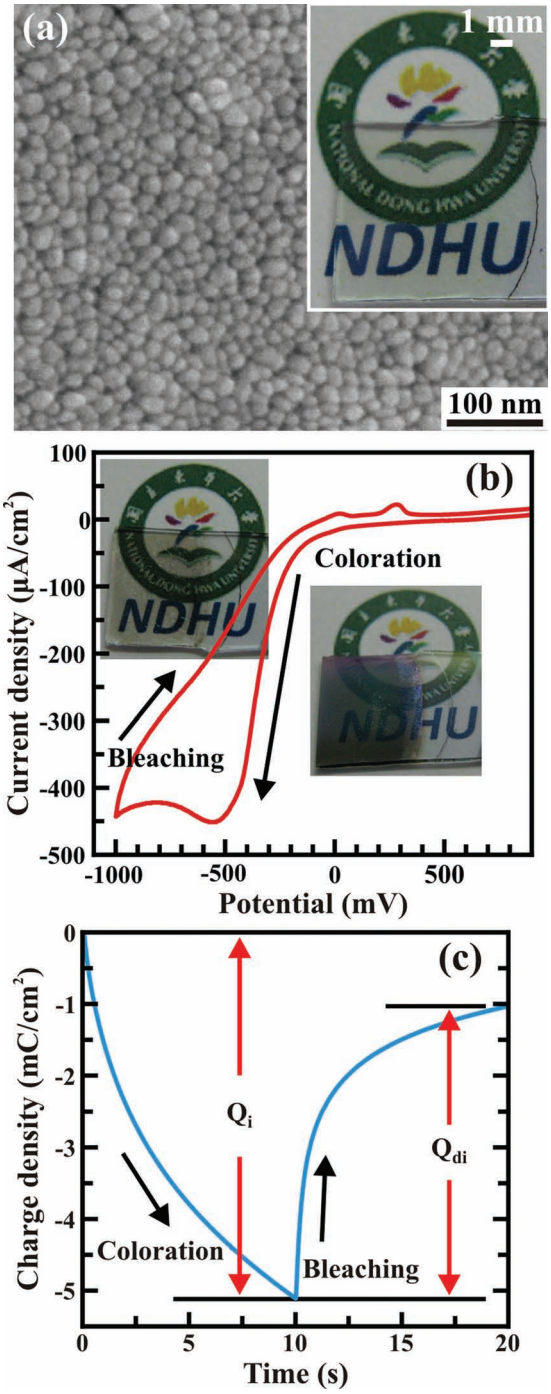

Figure 36. a) FESEM image of a portion of the large-area and high-density array showing the 1D Ta_2O_5 nanorods on the transparent and conducting ITO thin-film. The photograph inset to (a) shows a transparent large-area high-density 1D Ta_2O_5 nanorod array on a conducting ITO thin-film coated on glass. b) CV graph of the Ta_2O_5-nanorods/ITO thin-film for the coloration and bleaching cycles. The photographs insets to (b) shows the coloration (deep blue) and bleaching (yellowish) states of the Ta_2O_5-nanorods/ITO thin-film. c) The CC graph of the Ta_2O_5-nanorods/ITO thin-film showing the reversibility where the arrows signify the forward (coloration) and reverse (bleaching) scans. Reproduced with permission.[58] Copyright 2011, American Institute of Physics.

Chronocoulometry (CC) measurements are a good method to study the changes in the charge density of Li^+ ions during the intercalation and deintercalation. The CC graph in Figure 36c shows the charge density of Li^+ ions as a function of time. When a negative potential of –1 V is applied, the charge density of the electrolyte drops to –5.11 mC cm^{-2} in 10 s. When the negative potential of –1 V is switched to a positive potential of 0.9 V, the charge density rises to –1.3 mC cm^{-2} in 10 s. The charge densities for the intercalation and deintercalation routes are 5.11 mC cm^{-2} ($\equiv Q_i$) and 4.08 mC cm^{-2} ($\equiv Q_{di}$), respectively. The reversibility of the Ta_2O_5-nanorods/ITO thin film that can be determined with (Q_{di}/Q_i)[309] is ≈79.8%. The large-area high-density 1D Ta_2O_5 nanorod array can strongly enhance the Li^+ intercalation and deintercalation routes. Many factors, such as the 1D features, large-area, high-density, thickness and textural boundaries, can cause a great improvement in the ion pathways in the large-area high-density 1D Ta_2O_5 nanorod array, which significantly assists in the transport or migration of Li^+ ions to and from the sample surface. The large diffusion coefficient and high reversibility make the large-area high-density 1D Ta_2O_5 nanorod arrays excellent for electrochromic devices or smart windows.

5.3. Light-Emitting Diodes

Light-emitting diodes (LEDs) are a typical p–n junction device that can generate visible light emission simply by the application of electrical power. In short, excited electrons in the conduction band drop back to the valence band and recombine with holes. Visible light is then emitted to release energy. This phenomenon is called electroluminescence (EL). Metal oxides are good semiconducting materials and therefore can be used for LED applications. There are more advantages to the use of 1D nanostructures of metal oxides for this purpose than the bulk material or thin films because of their large bandgap (3.37 eV) and enhanced emission efficiency. Many 1D nanostructures of metal oxides, including ZnO,[239,240,310–315] NiO,[313,316] SnO,[317,318] and Ta_2O_5,[149,150] are utilized for LEDs. 1D ZnO nanostructures are the best choice for the fabrication of LEDs. The light emissions from the ZnO nanostructures are strongly dependent on the growth methods and conditions and they can emit various colors of light, including ultraviolet,[313,319] violet-blue,[240,314] blue-white,[315] blue,[311,312,320,321] white,[322] yellow-green,[313] orange-red,[323] green,[323] violet,[323] etc.

ZnO has the potential for use in LEDs and optoelectronic devices that operate at room temperature because of the wide ≈3.36 eV bandgap, which allows it to operate in harsh environments, such as outer space and high radiation facilities.[324,325] Light has a better chance to escape from nanostructure-based LED devices and heat is easily released. **Figure 37**a shows an FESM image of vertically aligned ZnO nanorod arrays capped by a ZnO thin film.[312] The ZnO nanorods are ≈700 nm long and ≈80 nm wide, and the ZnO film is ≈200 μm thick. The vertically aligned ZnO nanorod arrays and the ZnO thin film are prepared by a catalyst-free metal-organic chemical vapor deposition (MOCVD) procedure on Al_2O_3 substrates with p-type GaN interlayers. Figure 37b displays the room temperature *IV* curves obtained from the n-ZnO nanorods/p-GaN heterostructures.

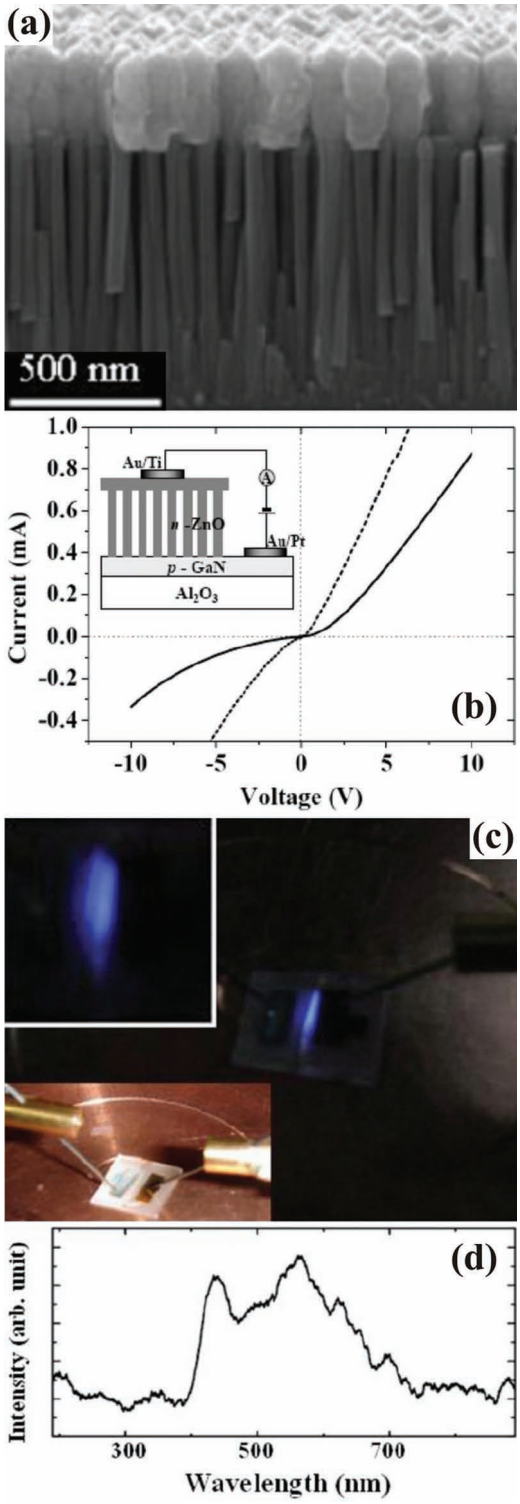

Figure 37. a) FESEM images showing vertically aligned ZnO nanorod arrays are capped by a ZnO thin film. b) Room temperature *IV* curves of the n-ZnO nanorods/p-GaN heterostructures. The inset to (b) shows a schematic diagram of the nanorod-array-based LED device, which consists of the n-ZnO nanorods/p-GaN heterostructures. c) Photographs showing blue light emissions, or EL, from the nanorod-array-based LED device at the forward bias. d) EL spectra of the nanorod-array-based LED device. Reproduced with permission.[312] Copyright 2007, Institute of Physics.

The schematic diagram in the inset to Figure 37b shows the nanorod-array-based LED device, which consists of the n-ZnO nanorods/p-GaN heterostructures. The *IV* curves are obviously asymmetrical, indicating the rectifying behavior of the n-ZnO nanorods/p-GaN heterostructures in nanorod-array-based LED devices. There is no current delay at the forward bias because both the metal/n-ZnO and metal/p-GaN interfaces have good ohmic contacts with a negligible Schottky barrier. When the n-ZnO nanorods/p-GaN heterostructures are exposed to UV light emission of 365 nm, the current is enhanced. The *IV*-curve results verify that the n-ZnO nanorods/p-GaN heterostructures are very sensitive to UV and therefore the heterostructures can be used as UV sensors. The photographs in Figure 37c demonstrate the EL of the blue light emitted from the nanorod-array-based LED device at the forward bias. The blue light emissions are intensive and thus can be seen by the naked eye. Figure 37d shows the EL spectra obtained from the nanorod-based LED device. The wavelengths mainly range between 440 and 600 nm. However, at the backward bias, no light emission is observed. The blue light emission supposedly comes from the p-GaN layer, so the excited electrons originate from the n-ZnO nanorods. Thus, the electrons from the n-ZnO nanorods are injected into the p-GaN layer at the forward bias, while no electrons can be injected into the p-GaN layer at the backward bias. This is what gives the n-ZnO nanorods/p-GaN heterostructures promise for optoelectronic applications.

Reliable electrical injection into a single 1D ZnO nanowire can be described for LEDs and laser diodes. **Figure 38**a shows a schematic diagram of the procedure for the preparation of a metallic contact on the top surface of a single ZnO nanowire.[310] 1D ZnO nanowires are randomly dispersed on a heavily doped p-Si substrate (resistivity is 0.001 Ω cm). A poly(methyl methacrylate) (PMMA) thin film of ≈120 nm is then spin-coated onto the substrate. The PMMA surface area (highlighted by the red box) is exposed to the electron beam. The unexposed PMMA area can be removed by acetone and the exposed area is shrunk and crosslinked with PMMA thin film. Ti/Au layers are then deposited by electron-beam evaporation to prepare the top contact, to completely form the single ZnO nanowire-based LED device. Figure 38b displays the EL and PL spectra of the single ZnO nanowire-based LED devices. The EL is taken at different voltages, and the PL is excited by a 325 nm He-Cd laser. All EL behaviors are similar and the spectral characteristics are reproducible for various devices. The short wavelength emissions can be enhanced for the single ZnO nanowire-based LED devices at elevated bias voltages. The light emissions range from 350 nm to 850 nm. The broad spectral peaks corresponding to the PL and EL emissions are contributed due to the defects and surface states. The weak luminescence centered at ≈380 nm is attributed to excitonic recombination. The PL is centered at 556 nm and has a full-width at half maximum (FWHM) of ≈170 nm.

An examination of Figure 37 shows that ZnO nanorod-array-based LED devices have to develop into the next generation of blue/near-UV light sources. Although the blue/near-UV light emissions do come from the ZnO nanorods, they are uncontrolled and randomly scattered. Also, the blue/near-UV light emissions cannot be distinguished. In other words it is important to control and enhance the spatial distribution of the EL from ZnO nanorod-array-based LED devices. The schematic

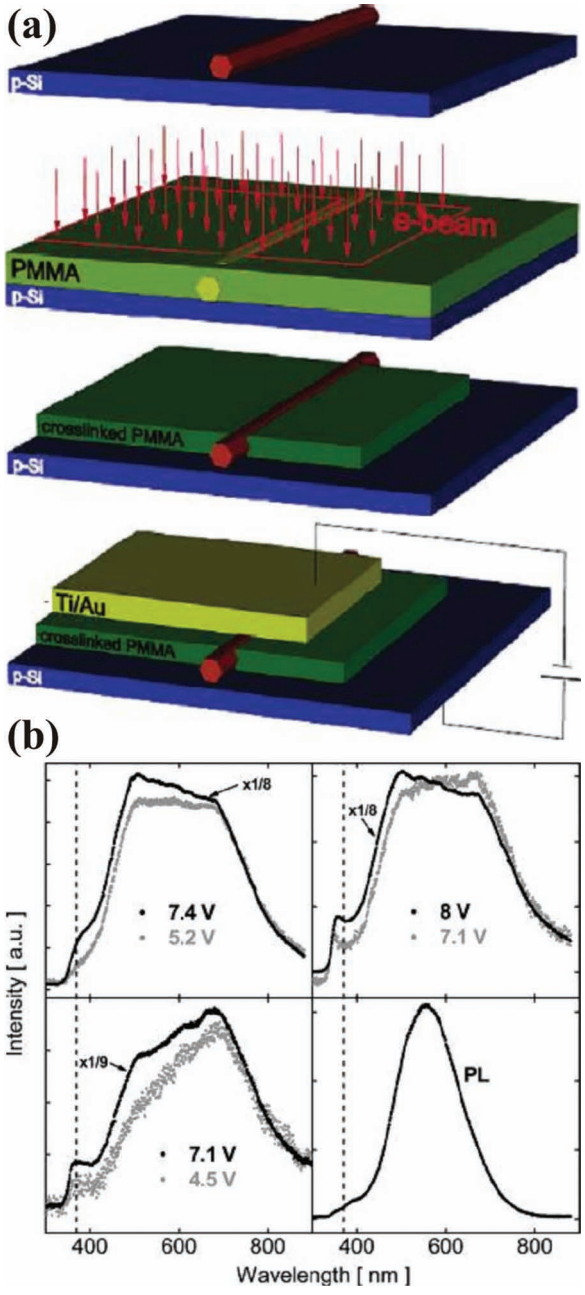

Figure 38. a) Schematic diagrams showing the procedure for preparation of a metallic contact on the top surface of a single ZnO nanowire. b) Room temperature EL and PL spectra of single ZnO nanowire-based LED devices. Reproduced with permission.[310] Copyright 2006, American Chemical Society.

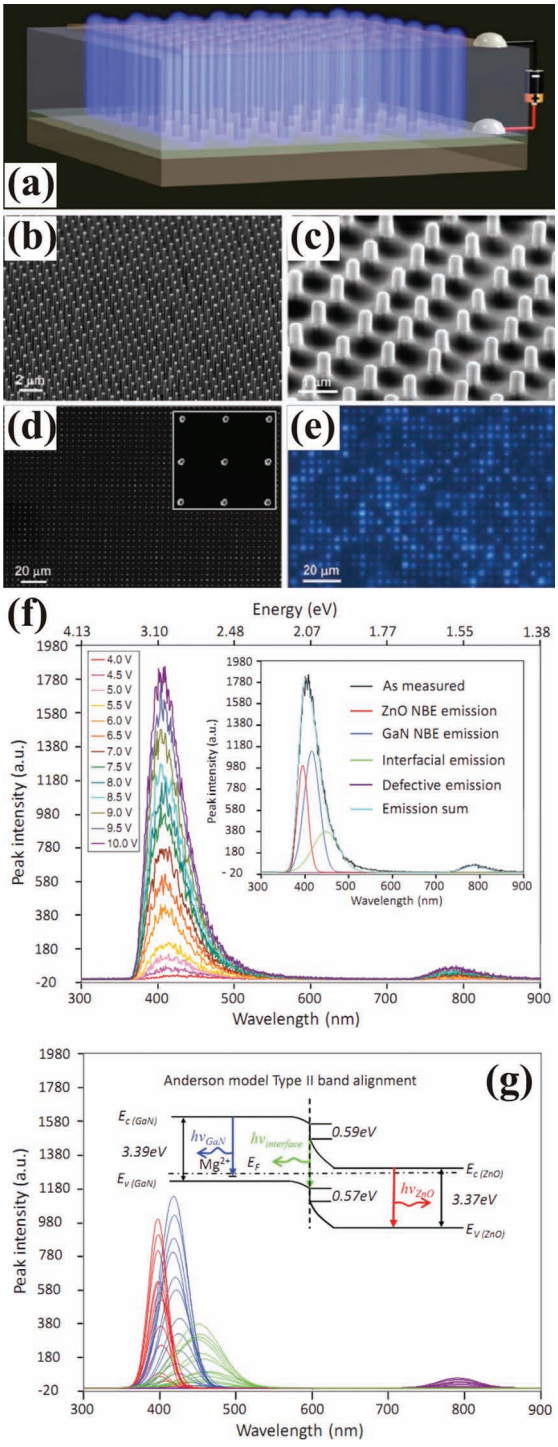

Figure 39. a) Schematic diagram of the ordered ZnO nanorod-array-based LED device. b–d) SEM images showing the side and top views of a portion of the controllable ordered ZnO nanorod arrays. e) Optical image showing the lit-up ZnO nanorod-array-based LED at an applied voltage of 10 V. f) EL spectra obtained from the ZnO nanorod-array-based LED devices. Inset to (f) showing three distinct decomposed EL peaks obtained with Gaussian functions. g) Evolution of the three distinct decomposed EL peaks at various applied voltages. The inset to (g) shows a schematic diagram of the n-ZnO/p-GaN heterojunction and three recombination processes. Reproduced with permission.[321] Copyright 2010.

diagram in **Figure 39**a displays an ordered ZnO nanorod-array-based LED device that is capable of controlling the positions of the ZnO nanorods on the p-GaN substrate.[321] The ZnO nanorods arranged in a controllable array pattern appear as ordered light spots. The SEM images in Figure 39b–d show the side and top views of a portion of the ordered ZnO nanorod arrays. The ZnO nanorods that are ≈30 nm wide are coated with SiO_2 and wrapped by PMMA. The ohmic contacts at the

interfaces between the bottom p-GaN and top n-ZnO nanorods can provide EL. Figure 39e shows an optical image of a lit-up ZnO nanorod-array-based LED for an applied voltage of 10 V. In the LED device, all of the ZnO nanorods are connected in parallel and each single nanorod behaves as a light emitter. The pitch between each lighting spot is 4 μm and the resolution is 6350 dpi. The brightness of the ordered ZnO nanorods is dissimilar, probably because of the current crowding effect, different serial contact resistances, and different injection currents moving through the individual nanorods. Figure 39f shows the EL spectra obtained from the ZnO nanorod-array-based LED devices. The light emissions are monitored at various applied voltages, from 4 to 10 V, at room temperature. The larger the applied voltage, the higher the intensity of the EL emission is. The main EL emission peaks show a slight blue shift in the range of 400–420 nm with a FWHM of ≈60 nm. The inset to Figure 39f shows the decomposition of an EL peak into three distinct EL peaks fit using Gaussian functions. Figure 39g displays the evolution of the three decomposed EL peaks at various applied voltages. The three EL peaks, centered in the ranges of 395–415, 420–440, and 450–510 nm, respectively, correspond to the three recombination processes. The inset to Figure 39g shows a band diagram of the n-ZnO/p-GaN heterojunction and three recombination processes, which are i) the near band edge (NBE) transitions in ZnO nanowires, ii) the transitions from the conduction band (or shallow donors) to deep Mg acceptor levels in the p-GaN thin film, and iii) the radiative interfacial transition of the electrons from n-ZnO and holes from p-GaN.

5.4. Field Emitters

A field emission is a physical phenomenon where electrons are emitted into a vacuum from sharp features when negative voltages are applied to the samples. This occurs with a strong electric field because electrons can easily tunnel through the potential barrier between sharp-tip features and metallic electrodes. The sharp-tip features can enhance the field emission properties, as the field emitters. The transition metal-oxides are good potential field emitters because of their thermal and chemical stability[1,2] so 1D metal oxide nanostructures should be excellent for field emitters in commercially produced flat displays. The 1D metal oxide nanostructures have very sharp-tip features at the ends. At the present time, many types of 1D metal oxide nanostructures have been used for field emission, including ZnO,[71,246,247,249,326,327] V_2O_5,[328,329] WO_3,[123] $WO_{2.9}$,[330] WO_2,[330] TiO_2,[331,332] SnO_2,[276,333,334] MoO_3,[335,336] and MoO_2.[337] Here, we introduce three significant examples[330,338,339] demonstrating the field emission of 1D metal oxide nanostructures.

The schematic diagram in **Figure 40**a shows the setup for an in situ measuring system.[338] The 1D ZnO nanowire (NW) sample is mounted perpendicular to the side of a triangular-shaped sample holder. A tungsten needle with a flat top is used as the counter electrode, and attached to an *x-y* mechanical stage (≈20 nm moving resolution). The *x-y* stage is controlled by a stage controller and the nanowire sample and the tungsten needle are connected to the negative and positive electrodes in a DC circuit source. The voltage and current are read by the

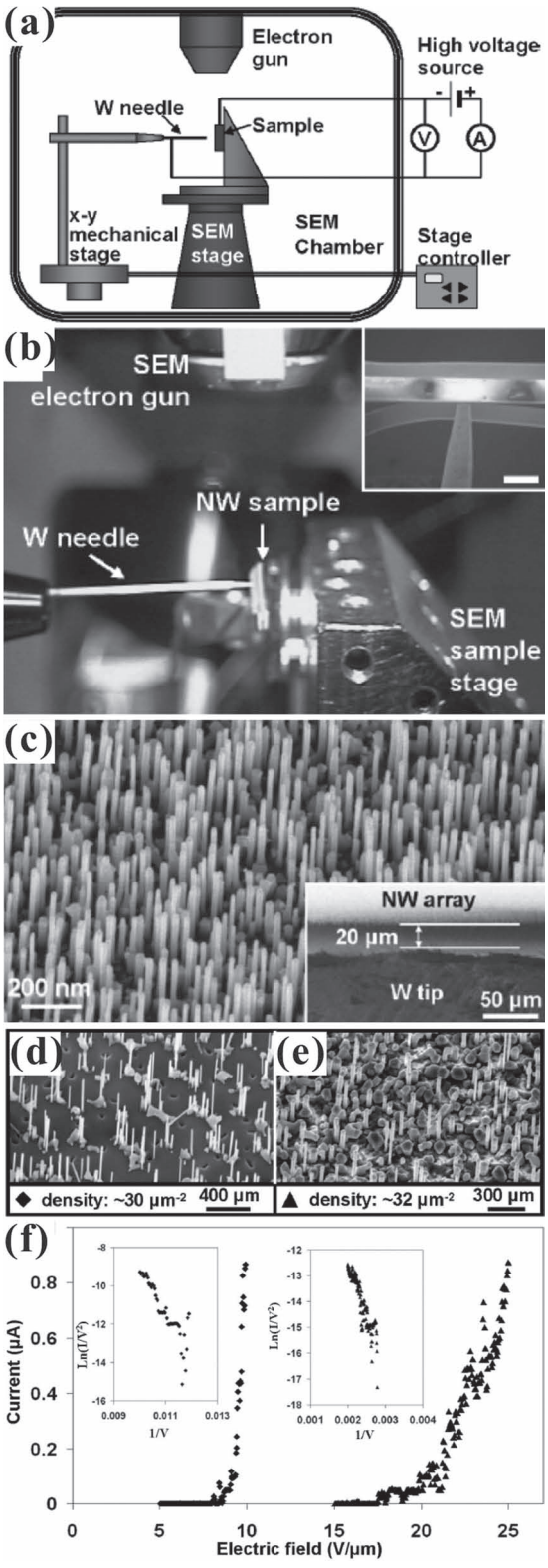

Figure 40. a) Schematic diagram and b) photograph of the setup of the in situ measuring system. c) SEM image showing a typical morphology of the high-density ZnO nanowires arranged in an array. d,e) SEM images showing the controlled and random ZnO nanowire arrays with similar densities. f) Corresponding *I–E* and F-N curves of field emission. Reproduced with permission.[338] Copyright 2007.

meter on the voltage source and picoampere meter, respectively. The photograph in Figure 40b shows an SEM chamber equipped with an in situ measuring system. The inset to Figure 40b shows the tungsten tip aligned to the nanowire sample at the same height. The SEM image in Figure 40c shows the typical morphology of the high-density ZnO nanowires arranged in an array. The ZnO nanowire array can have a density as high as ≈110 nanowires per square micrometers. Every single nanowire is self-aligned perpendicular to the substrate, and none is bent or interconnected with the other nanowires. These vertical self-aligned ZnO nanowires are perfect for field emission. The lengths and widths of the nanowires vary from ≈0.7 to 1 μm and from 30 to 40 nm, respectively. The SEM images in Figure 40d,e show ZnO nanowires that are controllably and randomly distributed in two arrays but with similar densities. Obviously, the separations between the ZnO nanowires in the controlled array are much more uniform than those in the random array. The current versus electric field (*I–E)* and Fowler–Nordheim (F-N) curves are shown in Figure 40f. The turn-on fields of the controlled and random arrays are only ≈9 and 21 V μm^{-1}, respectively. Both F-N curves are almost linear. The field-enhancement factors (β) obtained for the controlled and random arrays are 716 and 417, respectively. A larger β represents a higher field emitting efficiency, meaning the controlled array has a better field emission than the random array. This is because some ZnO nanowires grow closer together in the random array and the screen effect reduces the field-emitting efficiency.

Tungsten oxides may also be promising candidate materials for electron emitters. The TEM image in **Figure 41**a shows the setup for an in situ field-emission measurement system.[339] Large-area quasi-aligned $W_{18}O_{49}$ nanowires 10–50 nm wide and 100–500 long are grown on a tungsten surface. Field-emission measurements can be performed in a vacuum system with a background pressure of 2.0×10^{-6} Pa. The large-area quasi-aligned $W_{18}O_{49}$ nanowires are positioned at the cathode opposite to the metal anode, where the separation between anode and cathode is 250 μm. The graphs of the current density versus electric field (*J–E*) are shown in Figure 41b for large-area quasi-aligned $W_{18}O_{49}$ nanowires before and after ageing tests. The threshold fields are 14.9 and ≈12 V μm^{-1}, respectively at 1 mA cm^{-2}. The emission currents are 112 and 758 μA at 3.55 V for $W_{18}O_{49}$ nanowires before and after ageing tests, indicating that the $W_{18}O_{49}$ nanowires have improved after the ageing test to have better field emission properties. The improvement in field emission may be due to the fact that the tips of the $W_{18}O_{49}$ nanowires have been reconditioned after the ageing test. The graph of current versus time in Figure 41c) is obtained during an ageing test. It is found that the ageing current of 225 μA is larger than the 112 μA (see Figure 41b) at 3.55 kV measured before an ageing test. After an ageing test for 130 min, the emission current gradually increased to 860 μA, verifying that the ageing of the $W_{18}O_{49}$ nanowires led to improvement and better field emission properties.

The SEM images in **Figure 42**a–c show various 1D tungsten oxide nanorods grown at varying temperatures. These figures display large-area vertically aligned $WO_{2.9}$ and WO_2 nanorods and vertically aligned mixed nanorods of $WO_{2.9}$ and WO_2 grown at temperatures of 850 and 1550 °C, and in between 850 and 1550 °C, respectively. The diameters are slightly dependent on the temperature. The higher temperatures lead to thicker diameters. $WO_{2.9}$ and WO_2 nanorods have the smallest and

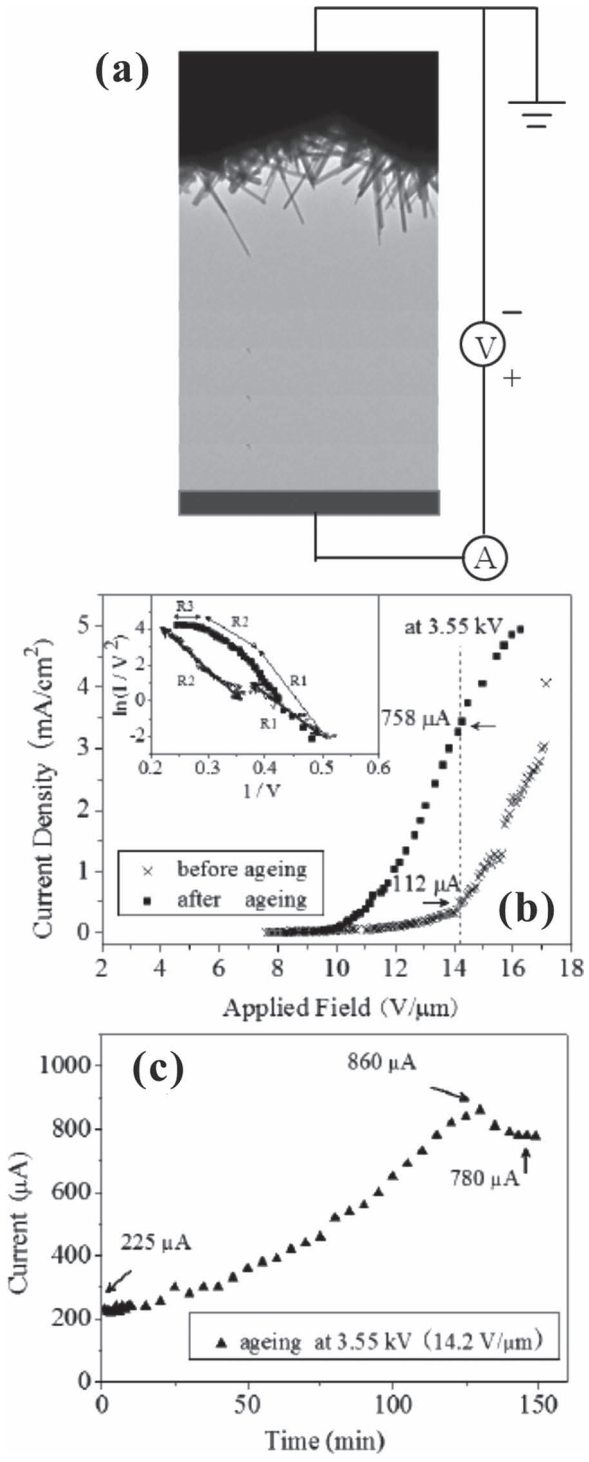

Figure 41. a) TEM image showing the setup of the in situ field-emission measurement system. b) Graphs showing the current versus electric field and c) current versus time for the tungsten oxide nanowire before and after ageing tests. Reproduced with permission.[339] Copyright 2011, Institute of Physics.

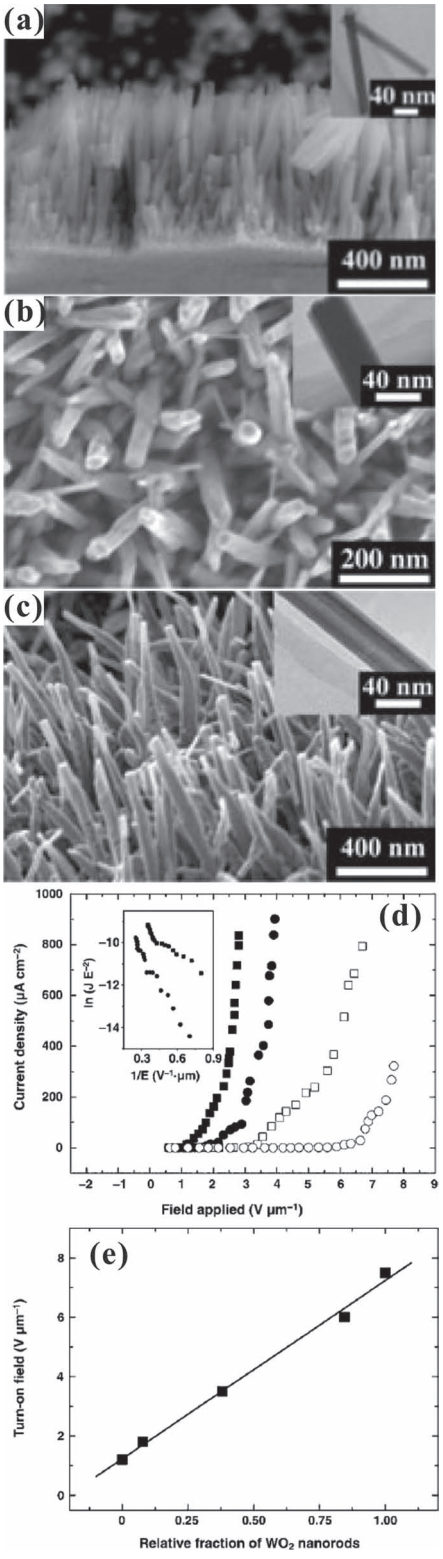

Figure 42. a–c) SEM images showing various $WO_{2.9}$ and WO_2 nanorods and mixtures of $WO_{2.9}$ and WO_2 nanorods grown at varying temperatures. d) Field-emission graphs of $WO_{2.9}$ and WO_2 nanorods and mixtures of $WO_{2.9}$ and WO_2 nanorods prepared at elevated temperatures of 850, 1050, 1150 and 1350 °C (from left to right). e) Linear graph of the turn-on field as a function of the relative content of WO_2 nanorods. Reproduced with permission.[330] Copyright 2005.

largest diameters while the mixed nanorods have diameters somewhere in between. The field emission graphs of *J–E* in Figure 42d illustrate the field-emission properties of $WO_{2.9}$ and WO_2 nanorods, and mixtures of $WO_{2.9}$ and WO_2 nanorods prepared at elevated temperatures of 850, 1050, 1150 and 1350 °C (from left to right). The turn-on fields of the $WO_{2.9}$ and WO_2 nanorods and the mixed $WO_{2.9}$ and WO_2 nanorods are 1.2, 1.8, 3.5, and 6.0 V μm^{-1}, respectively, at a current density of 10 $\mu A\ cm^{-2}$. The linear graph in Figure 42e shows the turn-on field as a function of the relative content of WO_2 nanorods. The function is perfectly linear so the smaller relative content of WO_2 nanorods gives a lower turn-on field.

5.5. Supercapacitors

Supercapacitors have recently been attracting more attention for purposes of energy storage than either regular batteries or the typical types of capacitors due to their high power density, moderate energy density, safe operation, and long cycle life. Supercapacitors are essentially an electrochemical double layer capacitor. The electrochemical performance of the supercapacitors is strongly associated with the intercalation and deintercalation of cations, such as H^+, Li^+, Na^+, and K^+ in electrolyte solutions at applied electric fields. Various electrolyte solutions, such as KOH,[340,341] KCl,[342] K_2SO_4,[343] $HClO_4$,[344] H_3PO_4+PVA,[345] HCl,[346,347] H_2SO_4,[342] Na_2SO_4,[260,348] Li_2SO_4,[343] $LiClO_4$,[342] $LiNO_3$,[349] LiOH,[349] $LiCoO_2$,[350] $LiFePO_4$,[350] and $LiPF_6$,[351] are utilized to provide cation sources for the supercapacitors. The supercapacitors are classified into the two kinds according to the charge storage mechanism of the capacitors: electrical double-layer capacitors (EDLCs) and Faradic pseudo-capacitors (or redox supercapacitors). In the EDLCs an electrical charge is built up at the electrode/electrolyte interface. They also usually have a high power density. However, the EDLCs suffer from low capacitance and low rate capability. The pseudo-capacitors have fast and reversible surfaces or near-surface reactions for charge storage. In comparison with the EDLCs, the active materials in the Faradic pseudo-capacitors provide higher specific capacitance, but they suffer from higher cost, poor rate capability, and low conductivity. It is known that 1D metal-oxide nanostructures are excellent candidates for supercapacitors, because of their large surface area and prominent capillary pathways, which gives them good charge storage ability and high specific capacitance. 1D metal-oxide nanostructures of RuO_2,[345] TiO_2,[345,346,351,352] V_2O_5,[342–344] NiO,[340,341] Bi_2O_3,[260] VO_2,[349] SnO_2,[348,350] MnO_2,[65,348] ZnO,[65,353] MoO_3,[353,354] and MoO_2,[354] have been used for the fabrication of supercapacitors. The schematic diagram in **Figure 43** shows a metal-oxide nanostructure-based supercapacitor, which consists of 1D metal-oxide nanostructures, an electrolyte solution, a separator, and two ITO thin-film electrodes. The electrolyte solution definitely contains anions and cations, whose charges are opposite to each other. The cations and anions in the n-type metal-oxide nanostructures intercalate at the surface of the nanostructures and the opposite electrode, respectively. However, in the p-type metal-oxide nanostructures, the anions and cations intercalate at the surface of the nanostructures and the opposite electrode.

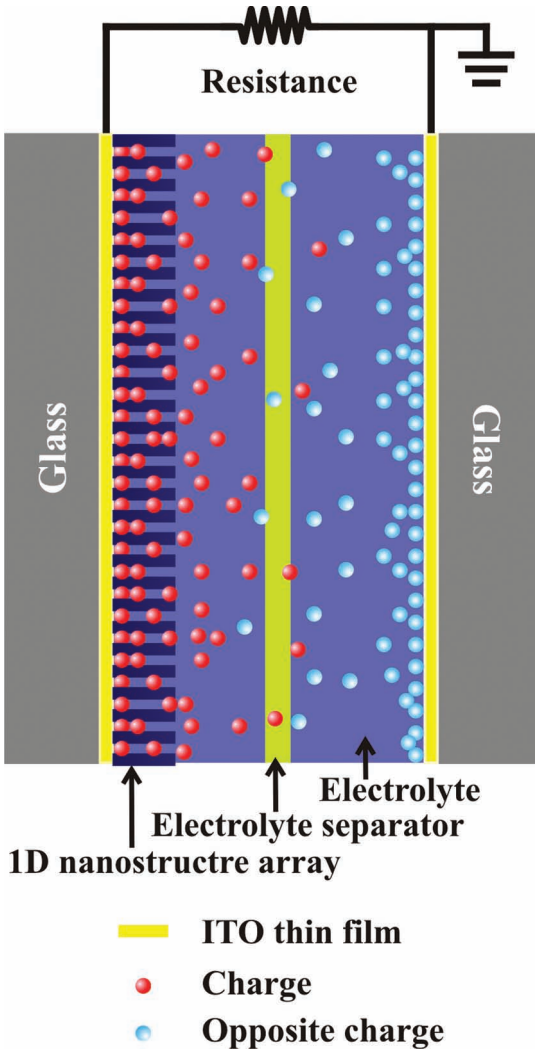

Figure 43. Schematic diagram of a 1D metal-oxide nanostructure-based supercapacitor.

It is important to understand the processes for the development of high power, high energy density, high specific surface area, high electronic conductivity, and fast cation intercalation/deintercalation high-performance supercapacitors. Among the transition metal oxides, MnO_2 is a very promising material for use in supercapacitors due to its low cost, environmentally friendly characteristics, and excellent capacitive performance. A facile synthesis method is employed to coat amorphous SnO_2/MnO_2 core/shell nanowires grown onto a stainless steel (SS) substrate, as shown in the schematic representation in **Figure 44**a.[348] The MnO_2 shells of the core/shell nanowires allow for fast and reversible faradic reactions, and facilitate a short ion diffusion path. The SnO_2 cores of the core/shell nanowires possess a high conductivity and provide a direct path for electron transport. The SnO_2/MnO_2 core/shell nanowires create channels for effective transport within the electrolyte. Figure 44b displays the CV curves of SnO_2/MnO_2 core/shell nanowires at various scanning rates of 2, 5, 10, 20, 50, and 100 mV s^{-1} in a 1 M Na_2SO_4 aqueous solution. It should be noted that the core SnO_2

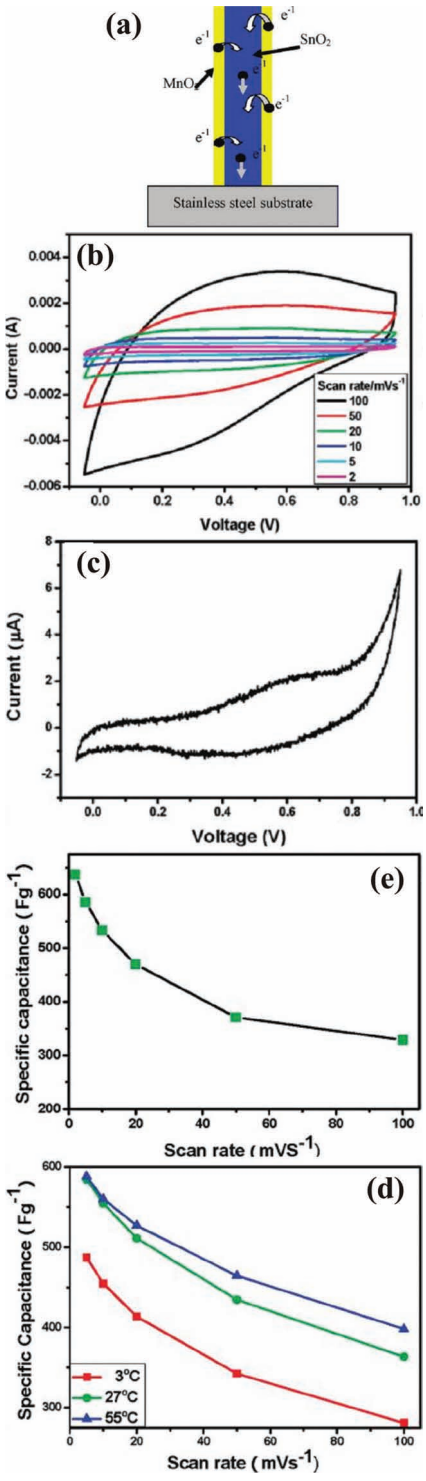

Figure 44. a) Schematic diagram showing the SnO_2/MnO_2 core/shell nanowires grown on a SS substrate. b) CV curves of the SnO_2/MnO_2 core/shell nanowires at scanning rates of 2, 5, 10, 20, 50, and 100 mV s^{-1} in a 1 M Na_2SO_4 aqueous solution. c) CV graph of the specific capacitance of the core SnO_2 nanowires grown on the SS substrate at a scanning rate of 2 mV s^{-1}. d) Graph showing the variation in the specific capacitance as a function of the scanning rate. e) Graph showing the specific capacitance obtained at various temperatures and scanning rates. Reproduced with permission.[348] Copyright 2010, American Chemical Society.

nanowires make no contribution to the capacitance because they are coated with MnO_2. The charge-storing process that occurs through faradic reactions is inhibited when the charge is stored at the surface or near the surface of the MnO_2 shells. The CV graph in Figure 44c shows the specific capacitance of the core SnO_2 nanowires grown on the SS substrate, which is 0.5 F g^{-1} at a scanning rate of 2 mV s^{-1}. Figure 44d shows the variation in the specific capacitance of the SnO_2/MnO_2 core/shell nanowires as a function of the scanning rate. Obviously, at a high scanning rate, there is a rapid decrease in the ions but an increase in the current. The specific capacitance values are 637 and 329 F g^{-1} at scanning rates of 2 and 100 mV s^{-1}, respectively. However, the SnO_2/MnO_2 core/shell nanowires still retain a high specific capacitance at a high scanning rate. The core/shell nanowire-based supercapacitors are strongly influenced by temperature. Figure 44e shows the specific capacitance obtained at various temperatures and scanning rates. Evidently the specific capacitance increases with elevated temperatures because of the decrease in the effective internal resistance.

In addition to metal oxides, conducting polymers are also considered for use in the fabrication of supercapacitors. Polyaniline (PANI) has been extensively studied for this purpose because of its relatively high conductivity, low cost, facile synthesis method and fast doping/dedoping rate.[347] A simple and cheap method is used to electropolymerize a disordered PANI nanowire array into an anodic TiO_2 nanotube array.[347] It is found that the PANI nanowire–titania nanotube arrays exhibit not only the superior capacitive property but also excellent cyclability, giving them promise for use in supercapacitors. The schematic diagram in **Figure 45**a shows a PANI-TiO_2/Ti nanocomposite electrode that has been strategically fabricated for a supercapacitor. Figure 45b shows CV graphs of the PANI-TiO_2/Ti and TiO_2/Ti nanocomposite electrodes. The CV graph of the PANI-TiO_2/Ti nanocomposite electrode is noticeably different from that of the TiO_2/Ti nanocomposite electrode. The CV curve of the former demonstrates two double redox peaks, suggestive of the large pseudocapacitance of that the PANI-TiO_2/Ti nanocomposite electrode. However, the CV curve (see inset to Figure 45b) of the TiO_2/Ti nanocomposite electrode indicates that it is a typical EDLC, and the corresponding capacitance is slightly smaller than that of the PANI-TiO_2/Ti nanocomposite electrode. Figure 45c shows the CV curves of the PANI-TiO_2/Ti nanocomposite electrode obtained at scanning rates of 5, 10, 20, 50, and 100 mV s^{-1}. All the CV profiles have similar spectral features in terms of anodic and cathodic peaks. It can be seen in the inset to Figure 45c that there is a linear increase in the peak currents of the nanocomposite electrode with the scanning rate. The results reveal excellent kinetic performance and high-power characteristics of the PANI-TiO_2/Ti nanocomposite electrode making it a good candidate for supercapacitors. Figure 45d shows the galvanostatic charge-discharge curves for the PANI-TiO_2/Ti nanocomposite electrode measured between 0 and 0.6 V at various current densities of 1, 2.5, 5, 7.5, 10, and 20 A g^{-1}. The specific capacitance of the PANI-TiO_2/Ti nanocomposite electrode can be calculated to be 732, 647, 603, 581, 568, and 543 F g^{-1}. The specific capacitance versus current density is shown in Figure 45e. Obviously, there is a slight decrease in the specific capacitance at elevated current densities. At a high current density of 20 A g^{-1}, the measured specific capacitance is around 74% that at 1 A g^{-1}, indicating the good rate capability of the PANI-TiO_2/Ti nanocomposite electrode. The results verify again that the PANI-TiO_2/Ti nanocomposite electrode is an excellent candidate for supercapacitors because it can provide high power density with little loss in energy density.

5.6. Nanoelectronics

The miniaturization of electronics has led to the development of nanodevices based on nanoscale building blocks, but it is expected that we will reach some fundamental physical limitations. The large aspect ratios of length to width of 1D metal-oxide nanostructures has made them promising candidates for diverse applications in nanoelectronics, including in field-effect transistors (FETs)[72,355–364] and logic circuits.[75,365–369] The 1D metal-oxide nanostructures utilized for nanoelectronics are mainly nanowires and nanorods, and the metal-oxides used for their fabrication include ZnO,[72,75,355,359–369] $WO_{2.72}$,[355] WO_3,[356] SnO_2,[357] and VO_x.[358] It should be noted that the characteristics of metal-oxide nanostructure-based electronics may be significantly different from those of the traditional bulk ones. Some of the special characteristics of metal-oxide nanostructure-based electronics are discussed below.

Nanowire-based electronics or devices can be constructed from the bottom up of innovative electronic building blocks. The reduced area of the nanocontact may enhance the contact's electrical properties. The properties of two-contact nanowire-based electronics have already been demonstrated in many studies, but it is still an important issue whether these arise from the nanocontacts or from the nanowires. The schematic diagrams in **Figure 46**a illustrate the conventional n-channel metal-oxide-semiconductor (MOS) FET and metal-oxide nanowire-based devices.[363] The source and drain electrodes of the conventional MOS FET devices are connected by a 2D conducting channel in a surface inversion layer. However, the source and drain electrodes of the nanowire-based device are conjoined through a single 1D metal-oxide nanowire that acts as a 1D conducting channel. The schematic diagrams in Figure 46b illustrate the corresponding contact areas of a conventional MOS FET and a nanowire-based device. A comparison of the two devices shows the significance of the nanocontact resistance gained for nanowire-based devices. Since the cross sectional area of a single nanowire is on the same order of magnitude as the de Broglie wavelength of the electron, ballistic quantum transport may occur in the 1D metal-oxide nanowire. The contact resistance (R_C) is proportional and inversely proportional to the specific contact resistivity (ρ_C) and contact area (A_C), respectively. The general rule for the contact resistance is formulated as $R_C = \rho_C/A_C$. As shown in Figure 46b, the nanocontact area is apparently 2 or 3 orders of magnitude larger than the conventional contact area, which means that the nanocontact resistance (R_C) in the nanowire-based device is a hundred or a thousand times higher than that of the conventional MOS FET device at the same specific contact resistivity (ρ_C). Consequently, the distinctive attribute of the tiny contact area in the nanowire-based device greatly intensifies the nanocontact resistance, which has a strong influence on the electrical properties

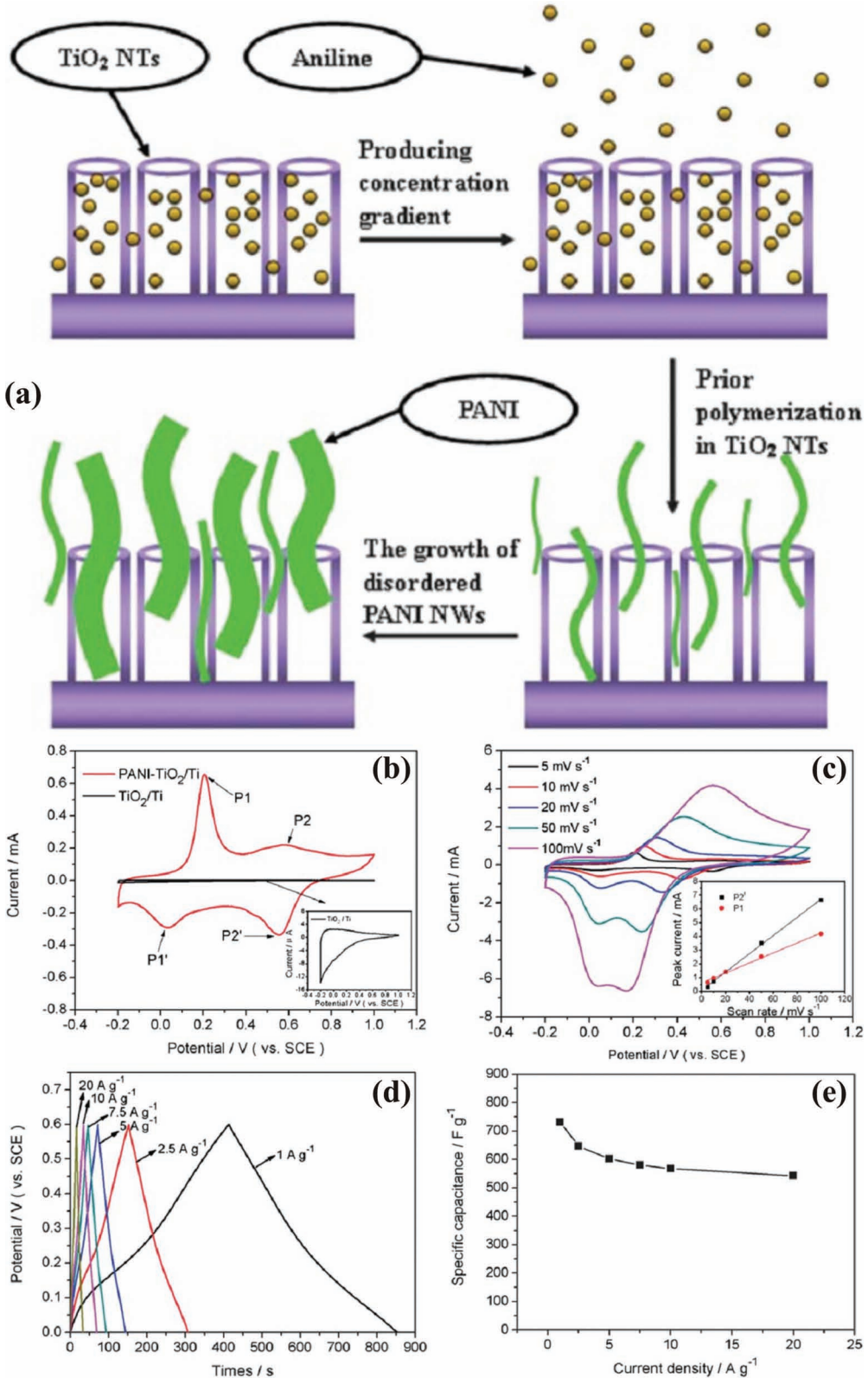

Figure 45. a) Schematic diagram showing the PANI-TiO_2/Ti nanocomposite electrode. b) CV graphs of the PANI-TiO_2/Ti and TiO_2/Ti nanocomposite electrodes, respectively. c) CV curves of the PANI-TiO_2/Ti nanocomposite electrode obtained at scanning rates of 5, 10, 20, 50, and 100 mV s^{-1}, respectively. It can be seen in the inset to (c) that the peak currents increase linearly with the scanning rate. d) Galvanostatic charge-discharge curves of the PANI-TiO_2/Ti nanocomposite electrode. e) Specific capacitance of the PANI-TiO_2/Ti nanocomposite electrode as a function of current density. Reproduced with permission.[347] Copyright 2011, Royal Society of Chemistry.

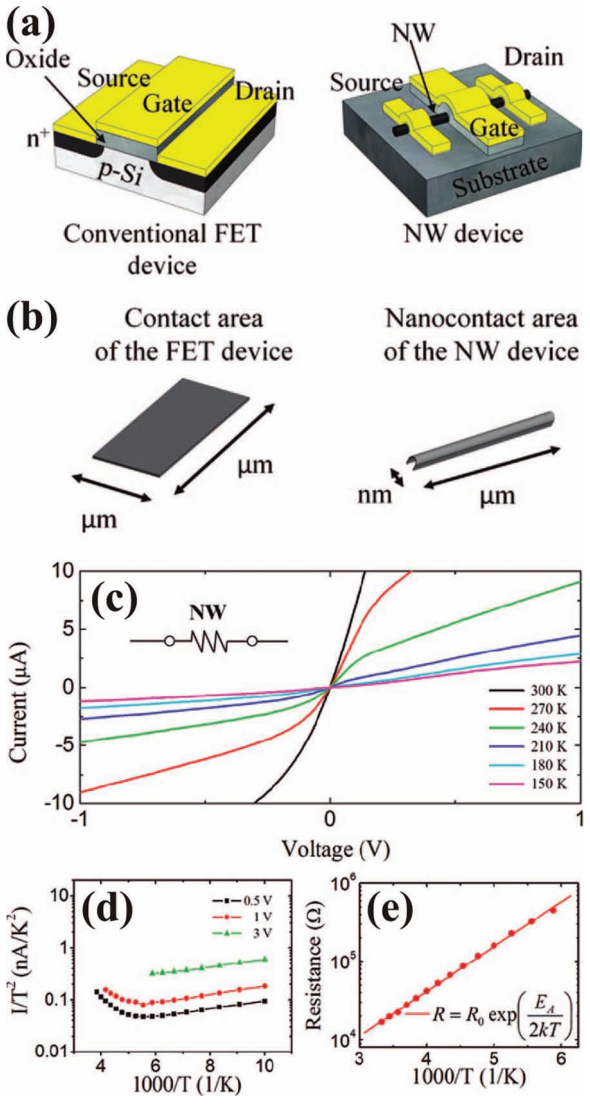

Figure 46. a) Schematic diagrams of the conventional n-channel MOS FET and metal-oxide nanowire-based devices. b) Schematic diagrams of the corresponding contact areas of a conventional MOS FET and a nanowire-based device. c) Graph showing various *IV* curves obtained from 150° to RT for the ZnO nanowire-based device. The inset to (c) shows the circuit with the two Ohmic nanocontacts (indicated by circles) at either end of the single ZnO nanowire (resistance symbol). d) Graph showing the different temperature behaviors of the ZnO nanowire-based device at various bias voltages. e) Graph of the zero-voltage resistances as a function of temperature. Reproduced with permission.[363] Copyright 2008, American Chemical Society.

of the nanowire-based electronics. The *IV* graph in Figure 46c shows various *IV* curves obtained from 150° to room temperature (RT) for the ZnO nanowire-based device. At small voltages, the *IV* curves are linear and bent downward symmetrically with descending temperature. The ZnO nanowire-based device possesses the characteristics of linear *IV* curves and lower RT resistances, implying that both of the nanocontacts are of the Ohmic type. The inset to Figure 46c shows a schematic representation of a circuit diagram of the two Ohmic nanocontacts (indicated by circles) at either end of the single ZnO nanowire (resistance symbol). The two Ohmic nanocontacts indicate that the main contribution to resistance in the ZnO nanowire-based device is from the intrinsic ZnO nanowire. The graph in Figure 46d shows the different temperature behaviors of the ZnO nanowire-based device at various bias voltages. The graph in Figure 46e displays the zero-voltage resistances as a function of temperature, verifying the intrinsic ZnO nanowire resistance and the thermally activated transport of conduction through the single nanowire.

ZnO nanowire-based logic inverters play a key role in logic circuits. Simple logic circuits with a high gain and robust noise margin normally consist of n-channel depletion-mode (D-mode) ZnO-nanowire-based FETs as the load device, and n-channel enhancement-mode (E-mode) ZnO-nanowire-based FETs as the driver device.[367] The D- and E-mode ZnO nanowire-based transistors are respectively controlled by smooth and corrugated ZnO nanowires grown on an Au-coated *c*-plane sapphire (denoted as Au-sapphire) and an Au-coated gallium-doped ZnO film (denoted as Au-GZO film). The TEM images and SAED patterns in **Figure 47**a,b show the single smooth and corrugated ZnO nanowires, respectively. The lattice-resolved images and SAED patterns in these figures indicate that both types of ZnO nanowires are single crystalline with the preferred growth direction being [0001]. Figure 47c shows a schematic representation of a ZnO nanowire-based logic inverter comprised of D- and E-mode ZnO nanowire-based transistors functioning as the driver and load devices, respectively. The smooth and corrugated ZnO nanowires operate as D- and E-mode transistors, respectively. The optical images in Figure 47d show actual inverters composed of D-mode and E-mode ZnO nanowire-based FET devices. The SEM image in Figure 47e shows a ZnO nanowire-based FET device (before being coated with cPVP) that functions as a component in the logic inverters.

The graphs in Figure 47f,g show *IV* curves of the smooth and corrugated ZnO nanowires grown on the Au-sapphire and the Au-GZO film indicating the output characteristics and the transfer characteristics. As can be seen in Figure 47f, the *IV* curves ($I_{DS}V_{DS}$, source-drain current versus drain voltage) of both ZnO nanowire-based FETs exhibit well-defined linear regimes at low bias, and saturation regimes at high bias, indicating that both demonstrate the typical n-type FET electrical behavior. However, the *IV* behavior of the smooth ZnO nanowires grown on the Au-sapphire (left-hand panel) is different from that of the corrugated ZnO nanowires grown on the Au-sapphire and the Au-GZO film (right-hand panel). It can be seen that the electrical conductance and threshold voltage can be controlled by the surface roughness of the ZnO nanowires. Figure 47g displays the *IV* curves ($I_{DS}V_{GS}$, source-drain current versus gate voltage) of both ZnO nanowire-based FETs. The smooth ZnO nanowire-based FET device fabricated on the Au-coated sapphire substrate operates as the on-type n-channel D-mode (blue symbols). The *IV* characteristics of the smooth ZnO nanowire-based FET device exhibit nonzero current at a zero gate bias and a negative threshold voltage, indicating that the smooth ZnO nanowire-based FETs exhibit a negative threshold voltage (D-mode behavior). On the other hand, the corrugated ZnO nanowire FET device fabricated on the Au-GZO film operates as an off-type device in the n-channel E-mode (red symbols). The *IV* characteristics of the corrugated

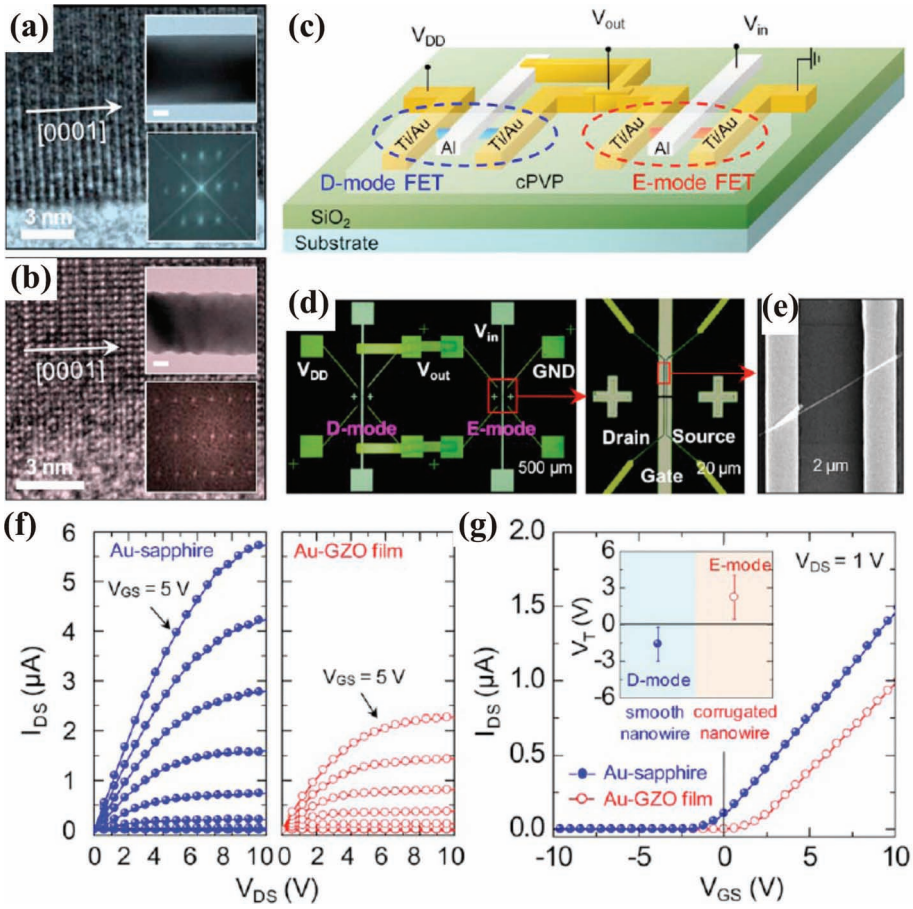

Figure 47. TEM images and SAED patterns showing the single a) smooth and b) corrugated ZnO nanowires. c) Schematic diagram of the ZnO nanowire-based logic inverters comprised of the D- and E-mode ZnO nanowire-based transistors for the driver and load, respectively. d) Optical images of the actual inverters composed of D-mode and E-mode ZnO nanowire-based FET devices. e) SEM image of a ZnO nanowire-based FET device. *IV* curves for the smooth and corrugated ZnO nanowires grown on the Au-sapphire and the Au-GZO film for (f) show the output characteristics and (g) transfer characteristics. Reproduced with permission.[367] Copyright 2009, American Institute of Physics.

ZnO nanowire-based FET device exhibit off-current status at a zero gate bias and a positive threshold voltage, implying that the corrugated ZnO nanowire-based FETs exhibit a positive threshold voltage (E-mode behavior). The threshold voltages of the D-mode and E-mode ZnO nanowire-based FETs are found to be –0.5 and 1.8 V, respectively. The inset to Figure 47g shows the statistical distribution of the threshold voltage positions of the D-mode and E-mode ZnO nanowire-based FETs. It can be seen that the D-mode and E-mode ZnO nanowire FETs can be well controlled by the nanowire surface morphology.

5.7. Nanogenerators

Harvesting of unexploited mechanical energy to power and drive electronic or nanodevices is increasingly attracting scientific attention. Nanoscale materials and nanotechnology could play important roles in the development of very small volume nanogenerators for self-powered electronics and nanodevices.[34,370–381] Using the piezoelectric effect, nanogenerators can convert external mechanical energy to electrical energy. Of the 1D nanomaterials, only 1D ZnO nanostructures possess the potential for use in these nanogenerators. ZnO has three advantages for this purpose: i) excellent semiconducting and piezoelectric properties; ii) little toxicity which makes it good for biosafe, biocompatible biomedical applications; and iii) having the most diverse and abundant types of nanostructures, which can include nanowires,[34,371,373,375–378,381] nanorods,[370] nanocones,[371] and nanotubes,[372] most of which are almost exclusively n-type ZnO[34,370–372,374–381] but some p-type ZnO.[373] Under external mechanical forces these structures can be elastically deformed to create a piezoelectric potential that can induce a through current. The power generated by the 1D nanostructure-based nanogenerators is influenced by many factors such as the i) number of active nanostructures; ii) the magnitude of the external forces that control the deflections; iii) the contact resistance between the electrodes and the nanostructures, which dissipates the voltage; iv) the optimal conductivity of the nanostructures; and v) the size of the electrodes.

As mentioned above, nanoscale mechanical energy can be converted into electrical energy by means of piezoelectric ZnO nanowire arrays.[34] **Figure 48**a shows an SEM image of large-area

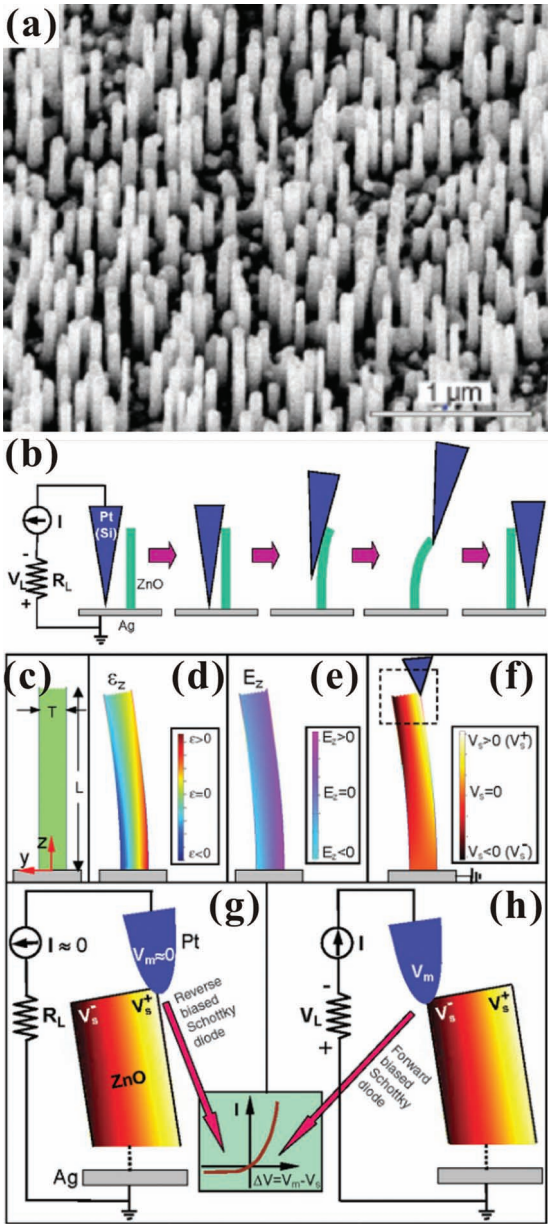

Figure 48. a) SEM image of the large-area aligned ZnO nanowires grown on an Al_2O_3 substrate. b) Schematic diagram of a coated Pt AFM tip scanning a ZnO nanowire in the contact mode. c–h) Schematic diagrams showing the physical principle for inducing current from the tip-nanowire interface at the forward bias. The stretching and compression of the nanowires creates the strain that can cause the electrical fields and voltages across the nanowires and finally induce a useful current. Reproduced with permission.[34] Copyright 2006, American Association for the Advancement of Science.

aligned ZnO nanowires grown on an Al_2O_3 substrate. A thin and continuous ZnO layer that first forms at the substrate serves as a large electrode connecting the ZnO nanowires to a metal electrode for transport measurement. For the purpose of nanogeneration, 0.2–0.5 mm long ZnO nanaowires are grown in a large-area but low density array, where the atomic force microscopy (AFM) tip can connect every single nanowire without touching the neighboring nanowires. Figure 48b shows a schematic diagram of a Pt-coated AFM tip for the scanning of individual ZnO nanowires in contact mode. The tip scans over the top of the ZnO nanowires and the height is adjusted according to the surface morphology and local contact force. Note that the force maintained between the AFM tip and the surface is always constant and perpendicular to the surface throughout the scan. The thermal vibration of the ZnO nanowires at room temperature is negligible.

The schematic diagrams in Figure 48c–h show the physical principle for creating the piezoelectric discharge energy that arises from the coupled piezoelectric and semiconducting properties of ZnO. A vertical, straight ZnO nanowire is displayed in Figure 48c. When the vertical, straight ZnO nanowire is deflected by an AFM tip, a strain field is created, as shown in Figure 48d. The outer and inner surfaces are stretched and compressed, undergoing positive ($\varepsilon > 0$) and negative ($\varepsilon < 0$) strains. An electric field is induced along the ZnO nanowire due to the piezoelectric effect, as shown in Figure 48e. Positive ($E_Z = \varepsilon_z/d > 0$) and negative ($E_Z = \varepsilon_z/d < 0$) electric fields are obtained along the stretched (outer) and compressed (inner) surfaces, where d is the piezoelectric coefficient. The electric potential follows the electrical fields, as demonstrated in Figure 48f. When a Pt-coated AFM tip comes into contact and deflects the nanowire, the induced electric potentials (V_s) are distributed as a gradient across the top end of the nanowire, as shown in Figure 48g. The V_s at the compressed and stretched side surfaces have a voltage of greater or less than zero, denoted by V_s^- and V_s^+, respectively. In fact, the potential is induced by the relative displacement of the Zn^{2+} cations with respect to the O^{2-} anions. These ionic charges cannot move freely and recombine without releasing the strain. The potential difference is maintained as long as the deformation is present. When the Pt-coated AFM tip comes into contact with the stretched surface, the potential (V_m) of the Pt-coated AFM tip is ≈0 V. The ZnO nanowires act as an n-type semiconductor, so the tip/nanowire interface is a reverse-biased Schottky diode. Little current is induced at the interface to flow through the nanowire and the circuit. When the Pt-coated AFM tip comes into contact with the compressed surface, the tip/nanowire interface becomes a forward-biased Schottky diode, as shown in Figure 48h. A large current is induced at the interface to flow through the nanowire and the circuit. This design gives a strong possibility for fabricating self-powered nanodevices that could be used in every type of electronic device, which would allow us to charge wireless devices outdoors.

6. Conclusion and Outlook

We reviewed the recent advances in the synthesis, characterization, and applications of 1D metal-oxide nanostructures. Using the direct physical deposition techniques, such as thermal evaporation, molecular beam epitaxial, sputtering, laser ablation, confinement growth, and lithography, atoms and molecules of the metal-oxides or compounds can grow in a preferential direction with or without external physical forces to form the 1D morphology. Similarly, the direct chemical deposition techniques, including CVD, HFMOVD, thermal oxidation,

solvothermal and sol-gel syntheses, can be used to synthesize 1D metal-oxide nanostructures with chemical reactions. The growth mechanisms of the 1D metal-oxide nanostructures mainly involve physical or chemical reactions, nucleation, assemblies, and crystallization. Based on the reactions, nucleation, assemblies, and crystallization, the growth mechanisms can be categorized into three types, including: VLS, VS, and SLS growth mechanisms.

The 1D metal-oxide nanostructures, including tungsten oxides, molybdenum oxides, tantalum oxides, vanadium oxides, niobium oxides, titanium oxides, nickel oxides, zinc oxides, bismuth oxides, and tin oxides, are characterized using microscopic analytic techniques, such as SEM, FESEM, and TEM. The microscopic analysis demonstrates the unique properties to be different from the bulk materials. Therefore, various 1D metal-oxide nanostructures are widely exploited as building blocks for appliactions in nanostructure-based devices because they have fascinating properties better than those of bulk metal-oxides. The nanostructure-based devices include gas sensors, electrochromic devices, LEDs, field-emission devices, supercapacitors, nanoelectronics, and nanogenerators.

Acknowledgements

The authors thank the National Science Council of the Republic of China for financial support of this research under Contract Nos. NSC-99-2112-M-259-004-MY2, NSC-99-2738-M-259-001, and NSC-101-2811-M-259-002.

Received: April 10, 2012
Published online: June 13, 2012

[1] J. Lee, M. C. Orilall, S. C. Warren, M. Kamperman, F. J. DiSalvo, U. Wiesner, *Nat. Mater.* **2008**, *7*, 222–228.
[2] H. J. Bolink, E. Coronado, J. Orozco, M. Sessolo, *Adv. Mater.* **2009**, *21*, 79–82.
[3] A. V. Emeline, G. V. Kataeva, A. V. Panasuk, V. K. Ryabchuk, N. V. Sheremetyeva, N. Serpone, *J. Phys. Chem. B* **2005**, *109*, 5175–5185.
[4] M. Kroger, S. Hamwi, J. Meyer, T. Riedl, W. Kowalsky, A. Kahn, *Org. Electron.* **2009**, *10*, 932–938.
[5] M. Gutowski, J. E. Jaffe, C. L. Liu, M. Stoker, R. I. Hegde, R. S. Rai, P. J. Tobin, *Appl. Phys. Lett.* **2002**, *80*, 1897–1899.
[6] G.-M. Rignanese, *J. Phys.: Condens. Matter* **2005**, *17*, R357–R379.
[7] J. Robertson, *Rep. Prog. Phys.* **2006**, *69*, 327–396.
[8] K. Chen, A. T. Bell, E. Iglesia1, *J. Catal.* **2002**, *209*, 35–42.
[9] V. V. Sysoev, B. K. Button, K. Wepsiec, S. Dmitriev, A. Kolmakov, *Nano Lett.* **2006**, *6*, 1584–1588.
[10] G. Mavrou, S. Galata, P. Tsipas, A. Sotiropoulos, Y. Panayiotatos, A. Dimoulas, E. K. Evangelou, J. W. Seo, Ch. Dieker, *J. Appl. Phys.* **2008**, *103*, 014506.
[11] M.-J. Lee, S. Han, S. H. Jeon, B. H. Park, B. S. Kang, S.-E. Ahn, K. H. Kim, C. B. Lee, C. J. Kim, I.-K. Yoo, D. H. Seo, X.-S. Li, J.-B. Park, J.-H. Lee, Y. Park, *Nano Lett.* **2009**, *9*, 1476–1481.
[12] X. Su, Z. Zhang, M. Zhu, *Appl. Phys. Lett.* **2006**, *88*, 061913.
[13] A. Dev, J. P. Richters, J. Sartor, H. Kalt, J. Gutowski, T. Voss, *Appl. Phys. Lett.* **2011**, *98*, 131111.
[14] D. R. Rosseinsky, R. J. Mortimer, *Adv. Mater.* **2001**, *13*, 783–793.
[15] C. G. Granqvist, *Sol. Energy Mater. Sol. Cells* **2008**, *92*, 203–208.
[16] K. Takada, H. Sakurai, E. Takayama-Muromachi, F. Izumi, R. A. Dilanian, T. Sasaki, *Nature* **2003**, *422*, 53–55.
[17] Z.-A. Ren, G.-C. Che, X.-L. Dong, J. Yang, W. Lu, W. Yi, X.-L. Shen, Z.-C. Li, L.-L. Sun, F. Zhou, Z.-X. Zhao, *EPL* **2008**, *83*, 17002.
[18] A. P. Alivisatos, *Science* **1996**, *271*, 933–937.
[19] F. W. Wise, *Acc. Chem. Res.* **2000**, *33*, 773–780.
[20] M. Haruta, M. Daté, *Appl. Catal. A: Gen.* **2001**, *222*, 427–437.
[21] B. Wu, A. Heidelberg, J. J. Boland, *Nat. Mater.* **2005**, *4*, 525–529.
[22] X. Duan, Y. Huang, Y. Cui, J. Wang, C. M. Lieber, *Nature* **2001**, *409*, 66–69.
[23] Y. Cui1, C. M. Lieber, *Science* **2001**, *291*, 851–853.
[24] Y. Huang, X. Duan, Y. Cui, L. J. Lauhon, K.-H. Kim, C. M. Lieber, *Science* **2001**, *294*, 1313–1317.
[25] J. Andzane, N. Petkov, A. I. Livshits, J. J. Boland, J. D. Holmes, D. Erts, *Nano Lett.* **2009**, *9*, 1824–1829.
[26] C. Ke, H. D. Espinosa, *Small* **2006**, *2*, 1484–1489.
[27] X. D. Wang, C. J. Summers, Z. L. Wang, *Nano Lett.* **2004**, *4*, 423–426.
[28] Y.-R. Ma, C.-M. Lin, C.-L. Yeh, R.-T. Huang, *J. Vac. Sci. Technol. B* **2005**, *23*, 2141–2145.
[29] Y.-R. Ma, C.-C. Tsai, S. F. Lee, K.-W. Cheng, Y. Liou, Y. D. Yao, *J. Magn. Magn. Mater.* **2006**, *304*, E13–E15.
[30] R. S. Devan, W.-D. Ho, J.-H. Lin, S. Y. Wu, Y.-R. Ma, P.-C. Lee, Y. Liou, *Cryst. Growth Des.* **2008**, *8*, 4465–4468.
[31] L. Kumari, Y.-R. Ma, C.-C. Tsai, Y.-W. Lin, S. Y. Wu, K.-W. Cheng, Y. Liou, *Nanotechnology* **2007**, *18*, 115717.
[32] Y. W. Heo, D. P. Norton, L. C. Tien, Y. Kwon, B. S. Kang, F. Ren, S. J. Pearton, J. R. LaRoche, *Mater. Sci. Eng. R* **2004**, *47*, 1–47.
[33] J. Zhou, Y. Ding, S. Z. Deng, L. Gong, N. S. Xu, Z. L. Wang, *Adv. Mater.* **2005**, *17*, 2107–2110.
[34] Z. L. Wang, J. Song, *Science* **2006**, *312*, 242–246.
[35] C. J. Park, D.-K. Choi, J. Yoo, G.-C. Yi, C. J. Lee, *Appl. Phys. Lett.* **2007**, *90*, 083107.
[36] P. M. Rao, X. Zheng, *Nano Lett.* **2009**, *9*, 3001–3006.
[37] S. M. Liu, L. M. Gan, L. H. Liu, W. D. Zhang, H. C. Zeng, *Chem. Mater.* **2002**, *14*, 1391–1397.
[38] H. E. Prakasam, K. Shankar, M. Paulose, O. K. Varghese, C. A. Grimes, *J. Phys. Chem. C* **2007**, *111*, 7235–7241.
[39] Z. W. Pan, Z. R. Dai, Z. L. Wang, *Science* **2001**, *291*, 1947–1949.
[40] A. Kolmakov, D. O. Klenov, Y. Lilach, S. Stemmer, M. Moskovits, *Nano Lett.* **2005**, *5*, 667–673.
[41] W. Wang, B. Zeng, J. Yang, B. Poudel, J. Huang, M. J. Naughton, Z. Ren, *Adv. Mater.* **2006**, *18*, 3275–3278.
[42] L. Kumari, J.-H. Lin, Y.-R. Ma, *J. Phys.-Condens. Matter* **2007**, *19*, 406204.
[43] B. Wang, Y. H. Yang, G. W. Yang, *Nanotechnology* **2006**, *17*, 4682–4688.
[44] O. Kazakova, B. Daly, J. D. Holmes, *Phys. Rev. B* **2006**, *74*, 184413.
[45] K. Matsui, B. K. Pradhan, T. Kyotani, A. Tomita, *J. Phys. Chem. B* **2001**, *105*, 5682–5688.
[46] M. Law, X. F. Zhang, R. Yu, T. Kuykendall, P. Yang, *Small* **2005**, *1*, 858–865.
[47] I.-D. Kim, A. Rothschild, B. H. Lee, D. Y. Kim, S. M. Jo, H. L. Tuller, *Nano Lett.* **2006**, *6*, 2009–2013.
[48] Z. Yang, T. Xu, Y. Ito, U. Welp, W. K. Kwok, *J. Phys. Chem. C* **2009**, *113*, 20521–20526.
[49] X. Y. Kong, Z. L. Wang, *Nano Lett.* **2003**, *3*, 1625–1631.
[50] S. Tsoi, E. Fok, J. C. Sit, J. G. C. Veinot, *Chem. Mater.* **2006**, *18*, 5260–5266.
[51] W. Zheng, Y. F. Zheng, K. W. Jin, N. Wang, *Talanta* **2008**, *74*, 1414–1419.
[52] M. A. Kumar, S. Jung, T. Ji, *Sensors* **2011**, *11*, 5087–5111.
[53] Y. L. Wang, X. C. Jiang, Y. N. Xia, *J. Am. Chem. Soc.* **2003**, *125*, 16176–16177.
[54] G. X. Wang, J. S. Park, M. S. Park, X. L. Gou, *Sens. Actuators B* **2008**, *131*, 313–317.

[55] V. T. Le, T. N. L. Le, V. H. Nguyen, *Sens. Actuators B* **2010**, *150*, 112–119.
[56] R. Rosario, D. Gust, A. A. Garcia, M. Hayes, J. L. Taraci, T. Clement, J. W. Dailey, S. T. Picraux, *J. Phys. Chem. B* **2004**, *108*, 12640–12642.
[57] J. Wang, E. Khoo, P. S. Lee, J. Ma, *J. Phys. Chem. C* **2008**, *112*, 14306–14312.
[58] R. S. Devan, S. Y. Gao, W. D. Ho, J. H. Lin, Y.-R. Ma, P. S. Patil, Y. Liou, *Appl. Phys. Lett.* **2011**, *98*, 133117.
[59] L. E. Greene, B. D. Yuhas, M. Law, D. Zitoun, P. Yang, *Inorg. Chem.* **2006**, *45*, 7535–7543.
[60] A. M. Peiró, P. Ravirajan, K. Govender, D. S. Boyle, P. O'Brien, D. D. C. Bradley, J. Nelson, J. R. Durranta, *J. Mater. Chem.* **2006**, *16*, 2088–2096.
[61] K. Zhu, T. B. Vinzant, N. R. Neale, A. J. Frank, *Nano Lett.* **2007**, *7*, 3739–3746.
[62] D. J. Yang, H. Park, S. J. Cho, H. G. Kim, W. Y. Choi, *J. Phys. Chem. Solids* **2008**, *69*, 1272–1275.
[63] D. K. Roh, R. Patel, S. H. Ahn, D. J. Kim, J. H. Kim, *Nanoscale* **2011**, *3*, 4162–4169.
[64] P.-C. Chen, G. Shen, S. Sukcharoenchoke, C. Zhou, *Appl. Phys. Lett.* **2009**, *94*, 043113.
[65] Y.-B. He, G.-R. Li, Z.-L. Wang, C.-Y. Su, Y.-X. Tong, *Energy Environ. Sci.* **2011**, *4*, 1288-1292.
[66] J. D. Prades, R. Jimenez-Diaz, F. Hernandez-Ramirez, L. Fernandez-Romero, T. Andreu, A. Cirera, A. Romano-Rodriguez, A. Cornet, J. R. Morante, S. Barth, S. Mathur, *J. Phys. Chem. C* **2008**, *112*, 14639–14644.
[67] N. Liu, G. Fang, W. Zeng, H. Zhou, F. Cheng, Q. Zheng, L. Yuan, X. Zou, X. Zhao, *ACS Appl. Mater. Interfaces* **2007**, *2*, 1973–1979.
[68] J. Kim, J.-H. Yun, C. H. Kim, Y. C. Park, J. Y. Woo, J. Park, J.-H. Lee, J. Yi, C.-S. Han, *Nanotechnology* **2010**, *21*, 115205.
[69] B. Ling, X. W. Sun, J. L. Zhao, C. Ke, S. T. Tan, R. Chen, H. D. Sun, Z. L. Dong, *J. Phys. Chem. C* **2010**, *114*, 18390–18395.
[70] S. Y. Li, P. Lin, C. Y. Lee, T. Y. Tseng, *J. Appl. Phys.* **2004**, *95*, 3711–3716.
[71] H. Zeng, X. Xu, Y. Bando, U. K. Gautam, T. Zhai, X. Fang, B. Liu, D. Golberg, *Adv. Funct. Mater.* **2009**, *19*, 3165–3172.
[72] Y. W. Heo, L. C. Tien, Y. Kwon, D. P. Norton, S. J. Pearton, B. S. Kang, F. Ren, *Appl. Phys. Lett.* **2004**, *85*, 2274–2276.
[73] P. Nguyen, H. T. Ng, T. Yamada, M. K. Smith, J. Li, J. Han, M. Meyyappan, *Nano Lett.* **2004**, *4*, 651–657.
[74] H.-J. Kim, C.-H. Lee, D.-W. Kim, G.-C. Yi, *Nanotechnology* **2006**, *17*, S327-S331.
[75] W. I. Park, J. S. Kim, G.-C. Yi, H.-J. Lee, *Adv. Mater.* **2005**, *17*, 1393–1397.
[76] Z. W. Pan, Z. R. Dai, Z. L. Wang, *Appl. Phys. Lett.* **2002**, *80*, 309–311.
[77] C. Li, G. Fang, S. Xu, D. Zhao, X. Zhao, *Nanotechnology* **2006**, *17*, 5367–5372.
[78] H. Zheng, J. Zhong, W. Wang, Y. Zheng, C. Ma, *Thin Solid Films* **2008**, *516*, 4983–4987.
[79] K. Nagashima, T. Yanagida, H. Tanaka, T. Kawai, *J. Appl. Phys.* **2007**, *101*, 124304.
[80] M. Tchernycheva, J. C. Harmand, G. Patriarche, L. Travers, *Nanotechnology* **2006**, *17*, 4025–4030.
[81] Z. Mia, Y.-L. Chang, *J. Nanophotonics* **2009**, *3*, 031602.
[82] J. C. Hulteen, C. R. Martin, *J. Mater. Chem.* **1997**, *7*, 1075–1087.
[83] A. Huczko, *Appl. Phys. A* **2000**, *70*, 365–376.
[84] H. W. Liang, S. Liu, S. H. Yu, *Adv. Mater.* **2010**, *22*, 3925–3937.
[85] Y. C. Choi, J. Kim, S. D. Bu, *Mater. Sci. Eng. B* **2006**, *133*, 245–249.
[86] J. G. Lu, P. Chang, Z. Fan, *Mater. Sci. Eng. R* **2006**, *52*, 49–91.
[87] X.-J. Wu, F. Zhu, C. Mu, Y. Liang, L. Xu, Q. Chen, R. Chen, D. Xu, *Coord. Chem. Rev.* **2010**, *254*, 1135–1150.
[88] K. Gerasopoulos, M. McCarthy, P. Banerjee, X. Fan, J. N. Culver, R. Ghodssi, *Nanotechnology* **2010**, *21*, 055304.
[89] X.-M. Yan, S. Kwon, A. M. Contreras, J. Bokor, G. A. Somorjai, *Nano Lett.* **2005**, *5*, 745–748.
[90] J. Jorritsma, J. A. Mydosh, *J. Appl. Phys.* **1998**, *84*, 901–906.
[91] E. Uccelli, M. Bichler, S. Nürnberger, G. Abstreiter, A. F. Morral, *Nanotechnology* **2008**, *19*, 045303.
[92] M. P. Zach, K. H. Ng, R. M. Penner, *Science* **2000**, *290*, 2120–2123.
[93] A. C. van Popta, M. M. Hawkeye, J. C. Sit, M. J. Brett, *Opt. Lett.* **2004**, *29*, 2545–2547.
[94] Y.-P. Zhao, D.-X. Ye, G.-C. Wang, T.-M. Lu, *Proc. SPIE* **2003**, *5219*, 59–73.
[95] C. N. R. Rao, S. R. C. Vivekchand, K. Biswasa, A. Govindaraj, *Dalton Trans.* **2007**, 3728–3749.
[96] D. A. Boyd, L. Greengard, M. Brongersma, M. Y. El-Naggar, D G. Goodwin, *Nano Lett.* **2006**, *6*, 2592–2597.
[97] E. Alarcón-Lladó, S. Estradé, J. D. Prades, F. Hernandez-Ramírez, J. Arbiol, F. Peiró, J. Ibáñez, L. Artúsa, J. R. Morante, *CrystEngComm* **2011**, *13*, 656–662.
[98] W. I. Park, D. H. Kim, S.-W. Jung, and G.-C. Yi, *Appl. Phys. Lett.* **2002**, *80*, 4232–4234.
[99] L. Kumari, J.-H. Lin, Y.-R. Ma, *Nanotechnology* **2007**, *18*, 295605.
[100] R. S. Devan, W.-D. Ho, S. Y. Wu, Y.-R. Ma, *J. Appl. Crystallogr.* **2010**, *43*, 498–503.
[101] R. S. Devan, J.-H. Lin, W.-D. Ho, S. Y. Wu, Y. Liou, Y.-R. Ma, *J. Appl. Crystallogr.* **2010**, *43*, 1062–1067.
[102] S. J. Limmer, G. Cao, *Adv. Mater.* **2003**, *15*, 427–431.
[103] C. W. Sun, H. Li, H. R. Zhang, Z. X. Wang, L. Q. Chen, *Nanotechnology* **2005**, *16*, 1454–1463.
[104] J. Z. Su, X. J. Feng, J. D. Sloppy, L. J. Guo, C. A. Grimes, *Nano Lett.* **2011**, *11*, 203–208.
[105] R. S. Wanger, W. C. Ellis, *Appl. Phys. Lett.* **1964**, *4*, 89–90.
[106] B. Wang, Y. H. Yang, N. S. Xu, G. W. Yang, *Phys. Rev. B* **2006**, *74*, 235305.
[107] Y. G. Yan, L. X. Zhou, J. Zhang, H. B. Zeng, Y. Zhang, L. D. Zhang, *J. Phys. Chem. C* **2008**, *112*, 10412–10417.
[108] T. J. Trentler, K. M. Hickman, S. C. Goel, A. M. Viano, P. C. Gibbons, W. E. Buhro, *Science* **1995**, *270*, 1791–1794.
[109] Z. W. Chen, J. K. L. Lai, C. H. Shek, *Appl. Phys. Lett.* **2005**, *86*, 181911.
[110] A. C. Santulli, M. Feygenson, F. E. Camino, M. C. Aronson, S. S. Wong, *Chem. Mater.* **2011**, *23*, 1000–1008.
[111] P. A. Sedach, T. J. Gordon, S. Y. Sayed, T. Furstenhaupt, R. H. Sui, T. Baumgartner, C. P. Berlinguette, *J. Mater. Chem.* **2010**, *20*, 5063–5069.
[112] P. M. Woodward, A. W. Sleight, T. Vogt, *J. Solid State Chem.* **1997**, *131*, 9–17.
[113] W. B. Hu, Y. Q. Zhu, W. K. Hsu, B. H. Chang, M. Terrones, N. Grobert, H. Terrones, J. P. Hare, H. W. Kroto, D. R. M. Walton, *Appl. Phys. A.* **2000**, *70*, 231–233.
[114] Y. Z. Jin, Y. Q. Zhu, R. L. D. Whitby, N. Yao, R. Ma, P. C. P. Watts, H. W. Kroto, D. R. M. Walton, *J. Phys. Chem. B* **2004**, *108*, 15572–15577.
[115] H. G. Choi, Y. H. Jung, D. K. Kim, *J. Am. Ceram. Soc.* **2005**, *88*, 1684–1686.
[116] R. Hu, H. S. Wu, K. Q. Hong, *J. Cryst. Growth* **2007**, *306*, 395–399.
[117] M. Žumer, V. Nemanič, B. Zajec, M. Wang, J. Wang, Y. Liu, L.-M. Peng, *J. Phys. Chem. C* **2008**, *112*, 5250–5253.
[118] Y. M. Zhao, Y. H. Li, I. Ahmad, D. G. McCartney, Y. Q. Zhu, W. B. Hu, *Appl. Phys. Lett.* **2006**, *89*, 133116.
[119] Z. J. Gu, H. Q. Li, T. Y. Zhai, W. S. Yang, Y. Y. Xia, Y. Ma, J. N. Yao, *J. Solid State Chem.* **2007**, *180*, 98–105.
[120] Z. G. Zhao, M. Miyauchi, *Angew. Chem. Int. Ed.* **2008**, *47*, 7051–7055.

[121] H. Wang, X. Quan, Y. Zhang, S. Chen, *Nanotechnology* **2008**, *19*, 065704.
[122] Z. Gu, T. Zhai, B. Gao, X. Sheng, Y. Wang, H. Fu, Y. Ma, J. Yao, *J. Phys. Chem. B* **2006**, *110*, 23829–23836.
[123] J. Zhou, L. Gong, S. Z. Deng, J. Chen, J. C. She, N. S. Xu, R. S. Yang, Z. L. Wang, *Appl. Phys. Lett.* **2005**, *87*, 223108.
[124] M. Shibuya, M. Miyauchi, *Chem. Phys. Lett.* **2009**, *473*, 126–130.
[125] X. Liu, J. Zhang, T. Yang, X. Guo, S. Wu, S. Wang, *Sens. Actuators B* **2011**, *156*, 918–923.
[126] K. Huang, Q. Pan, F. Yang, S. Ni, X. Wei, D. He, *J. Phys. D: Appl. Phys.* **2008**, *41*, 155417.
[127] K. Lee, W. S. Seo, J. T. Park, *J. Am. Chem. Soc.* **2003**, *125*, 3408–3409.
[128] D. Y. Lu, J. Chen, H. J. Chen, L. Gong, S. Z. Deng, N. S. Xu, Y. L. Liu, *Appl. Phys. Lett.* **2007**, *90*, 041919.
[129] Z. D. Xiao, L. D. Zhang, X. K. Tian, X. S. Fang, *Nanotechnology* **2005**, *16*, 2647–2650.
[130] P. A. Spevack, N. S. McIntyre, *J. Phys. Chem.* **1993**, *97*, 11020–11030.
[131] L. Q. Mai, B. Hu, W. Chen, Y. Y. Qi, C. S. Lao, R. S. Yang, Y. Dai, Z. L. Wang, *Adv. Mater.* **2007**, *19*, 3712–3716.
[132] J. Zhou, N. S. Xu, S. Z. Deng, J. Chen, J. C. She, Z. L. Wang, *Adv. Mater.* **2003**, *15*, 1835–1840.
[133] R. L. Smith, G. S. Rohrer, *J. Solid State Chem.* **1996**, *124*, 104–115.
[134] M. Dieterle, G. Mestl, *Phys. Chem. Chem. Phys.* **2002**, *4*, 822–826.
[135] D. Wang, D. Su, R. Schlögl, *Cryst. Res. Technol.* **2003**, *38*, 153–159.
[136] X. W. Lou, H. C. Zeng, *Chem. Mater.* **2002**, *14*, 4781–4789.
[137] R.-Q. Song, A.-W. Xu, B. Deng, Y.-P. Fang, *J. Phys. Chem. B* **2005**, *109*, 22758–22766.
[138] T. A. Xia, Q. Li, X. D. Liu, J. A. Meng, X. Q. Cao, *J. Phys. Chem. B* **2006**, *110*, 2006–2012.
[139] G. A. Camacho-Bragado, M. Jose-Yacaman, *Appl. Phys. A* **2006**, *82*, 19–22.
[140] X.-L. Li, J.-F. Liu, Y.-D. Li, *Appl. Phys. Lett.* **2002**, *81*, 4832–4834.
[141] Y. Li, Y. Bando, *Chem. Phys. Lett.* **2002**, *364*, 484–488.
[142] S. Hu, X. Wang, *J. Am. Chem. Soc.* **2008**, *130*, 8126–8127.
[143] M. Suemitsu, T. Abe, in *Inorganic and Metallic Nanotubular Materials: Recent Technologies and Applications*, (Ed: T. Kijima), Springer Verlag GmbH, Berlin **2010**, p. 83–96.
[144] L. Cheng, M. W. Shao, X. H. Wang, H. B. Hu, *Chem.-Eur. J.* **2009**, *15*, 2310–2316.
[145] J. Rajeswari, P. S. Kishore, B. Viswanathan, T. K. Varadarajan, *Electrochem. Commun.* **2009**, *11*, 572–575.
[146] A. M. Taurino, A. Forleo, L. Francioso, P. Siciliano, M. Stalder, R. Nesper, *Appl. Phys. Lett.* **2006**, *88*, 152111.
[147] H. M. Romero, A. M. Villafane, J. C. Nava, P. G. Casillas, C. M. Perez, *Ann. Chim.* **2005**, *95*, 703–707.
[148] J. E. Barton, C. L. Stender, P. Li, T. W. Odom, *J. Mater. Chem.* **2009**, *19*, 4896–4898.
[149] R. S. Devan, W. D. Ho, C. H. Chen, H. W. Shiu, C. H. Ho, C. L. Cheng, S. Y. Wu, Y. Liou, Y.-R. Ma, *Nanotechnology* **2009**, *20*, 445708.
[150] R. S. Devan, C. L. Lin, S. Y. Gao, C. L. Cheng, Y. Liou, Y.-R. Ma, *Phys. Chem. Chem. Phys.* **2011**, *13*, 13441–13446.
[151] M. M. Zhu, Z. J. Zhang, W. Miao, *Appl. Phys. Lett.* **2006**, *89*, 021915.
[152] Y. Jin, J. Y. Song, S. H. Jeong, J. W. Kim, T. G. Lee, J. H. Kim, J. Hahn, *J. Mater. Res.* **2010**, *25*, 1080–1086.
[153] M. H. Chen, X. Wang, L. N. Zhang, M. Yu, Q. Z. Qin, *Chem. Phys.* **1999**, *242*, 81–90.
[154] K. Fukuda, I. Nakai, Y. Ebina, R. Z. Ma, T. Sasaki, *Inorg. Chem.* **2007**, *46*, 4787–4789.
[155] S. Gnanarajan, S. K. H. Lam, C. P. Foley, *J. Appl. Phys.* **2007**, *101*, 063535.
[156] S. M. E. Green, S. Alex, N. L. Fleischer, E. L. Millam, T. P. Marcy, D. G. Leopold, *J. Chem. Phys.* **2001**, *114*, 2653–2668.
[157] Y. L. Chueh, L. J. Chou, Z. L. Wang, *Angew. Chem. Int. Edi* **2006**, *45*, 7773–7778.
[158] N. Dharmaraj, H. C. Park, C. H. Kim, P. Viswanathamurthi, H. Y. Kim, *Mater. Res. Bull.* **2006**, *41*, 612–619.
[159] J. Lin, N. Masaaki, A. Tsukune, M. Yamada, *Appl. Phys. Lett.* **1999**, *74*, 2370–2372.
[160] M. H. Asghar, F. Placido, S. Naseem, *Eur. Phys. J. Appl. Phys* **2006**, *36*, 119–124.
[161] N. K. Allam, X. J. Feng, C. A. Grimes, *Chem. Mater.* **2008**, *20*, 6477–6481.
[162] H. A. El-Sayed, V. I. Birss, *Nano Lett.* **2009**, *9*, 1350–1355.
[163] H. A. El-Sayed, V. I. Birss, *Nanoscale* **2010**, *2*, 793–798.
[164] K. Takahashi, S. J. Limmer, Y. Wang, G. Z. Cao, *J. Phys. Chem. B* **2004**, *108*, 9795–9800.
[165] T. Y. Zhai, H. M. Liu, H. Q. Li, X. S. Fang, M. Y. Liao, L. Li, H. S. Zhou, Y. Koide, Y. Bando, D. Goberg, *Adv. Mater.* **2010**, *22*, 2547–2552.
[166] R. Andre, F. Natalio, M. Humanes, J. Leppin, K. Heinze, R. Wever, H. C. Schroder, W. E. G. Muller, W. Tremel, *Adv. Funct. Mater.* **2011**, *21*, 501–509.
[167] Y. Q. Wang, Z. J. Zhang, Y. Zhu, Z. C. Li, R. Vajtai, L. J. Ci, P. M. Ajayan, *ACS Nano* **2008**, *2*, 1492–1496.
[168] C. X. Cao, Y. F. Gao, L. T. Kang, H. J. Luo, *CrystEngComm* **2010**, *12*, 4048–4051.
[169] G. S. Zakharova, I. Hellmann, V. L. Volkov, C. Taschner, A. Bachmatiuk, A. Leonhardt, R. Klingeler, B. Buchner, *Mater. Res. Bull.* **2010**, *45*, 1118–1121.
[170] J. Mendialdua, R. Casanova, Y. Barbaux, *J. Electron Spectrosc. Relat. Phenom.* **1995**, *71*, 249–261.
[171] M. Demeter, M. Neumann, W. Reichelt, *Surf. Sci.* **2000**, *454*, 41–44.
[172] H. Qiao, X. J. Zhu, Z. Zheng, L. Liu, L. Z. Zhang, *Electrochem. Commun.* **2006**, *8*, 21–26.
[173] M. Obara, A. Sekiyama, S. Imada, J. Yamaguchi, T. Miyamachi, T. Balashov, W. Wulfhekel, M. Yabashi, K. Tamasaku, A. Higashiya, T. Ishikawa, K. Fujiwara, H. Takagi, S. Suga, *Phys. Rev. B* **2010**, *81*, 113107.
[174] L. Mai, L. Xu, C. Han, X. Xu, Y. Luo, S. Zhao, Y. Zhao, *Nano Lett.* **2010**, *10*, 4750–4755.
[175] J. Liu, X. Wang, Q. Peng, Y. Li, *Adv. Mater.* **2005**, *17*, 764–767.
[176] B. X. Li, Y. Xu, G. Rong, M. Jing, Y. Xie, *Nanotechnology* **2006**, *17*, 2560–2566.
[177] G. Li, S. Pang, L. Jiang, Z. Guo, Z. Zhang, *J. Phys. Chem. B* **2006**, *110*, 9383–9386.
[178] S. Shi, M. Cao, X. He, H. Xie, *Cryst. Growth Des.* **2007**, *7*, 1893–1897.
[179] M. E. Spahr, P. Bitterli, R. Nesper, M. Muller, F. Krumeich, H. U. Nissen, *Angew. Chem. Int. Ed.* **1998**, *37*, 1263–1265.
[180] H.-J. Muhr, F. Krumeich, U. P. Schonholzer, F. Bieri, M. Niederberger, L. J. Gauckler, R. Nesper, *Adv. Mater.* **2000**, *12*, 231–234.
[181] A. Gloskovskii, S. A. Nepijko, G. Schonhense, H. A. Therese, A. Reiber, H. C. Kandpal, G. H. Fecher, C. Felser, W. Tremel, M. Klimenkov, *J. Appl. Phys.* **2007**, *101*, 084301.
[182] A. I. Popa, E. Vavilova, C. Taschner, V. Kataev, B. Buchner, R. Klingeler, *J. Phys. Chem. C* **2011**, *115*, 5265–5270.
[183] D. Bach, H. Stormer, R. Schneider, D. Gerthsen, J. Verbeeck, *Microsc. Microanal.* **2006**, *12*, 416–423.
[184] U. Cvelbar, M. Mozetic, *J. Phys. D: Appl. Phys.* **2007**, *40*, 2300–2303.
[185] B. Varghese, S. C. Haur, C. T. Lim, *J. Phys. Chem. C* **2008**, *112*, 10008–10012.

[186] M. Wei, Z.-M. Qi, M. Ichihara, H. Zhou, *Acta Mater.* **2008**, *56*, 2488–2494.
[187] H. Luo, M. Wei, K. Wei, *J. Nanomater.* **2009**, 758353.
[188] H. Wen, Z. Liu, J. Wang, Q. Yang, Y. Li, J. Yu, *Appl. Surf. Sci.* **2011**, *257*, 10084–10088.
[189] Y. Zhao, Z. J. Zhang, Y. H. Lin, *J. Phys. D-Appl. Phys.* **2004**, *37*, 3392–3395.
[190] M. J. Sayagues, J. L. Hutchison, *J. Solid State Chem.* **2002**, *163*, 137–143.
[191] M. J. Sayagues, J. L. Hutchison, *J. Solid State Chem.* **1996**, *124*, 116–122.
[192] H. J. Sayagues, J. L. Hutchison, *J. Solid State Chem.* **1999**, *146*, 202–210.
[193] M. Mozetic, U. Cvelbar, M. K. Sunkara, S. Vaddiraju, *Adv. Mater.* **2005**, *17*, 2138–2146.
[194] J. H. Lim, J. Choi, *J. Ind. Eng. Chem.* **2009**, *15*, 860–864.
[195] Y. Lin, Y. J. Yang, C. C. Hsu, *Thin Solid Films* **2011**, *519*, 3043–3049.
[196] Y. Kobayashi, H. Hata, M. Salama, T. E. Mallouk, *Nano Lett.* **2007**, *7*, 2142–2145.
[197] D. V. Bavykin, V. N. Parmon, A. A. Lapkin, F. C. Walsh, *J. Mater. Chem.* **2004**, *14*, 3370–3377.
[198] J. M. Macak, H. Tsuchiya, L. Taveira, S. Aldabergerova, P. Schmuki, *Angew. Chem. Int. Ed.* **2005**, *44*, 7463–7465.
[199] G. K. Mor, K. Shankar, M. Paulose, O. K. Varghese, C. A. Grimes, *Nano Lett.* **2006**, *6*, 215–218.
[200] M. Paulose, K. Shankar, O. K. Varghese, G. K. Mor, C. A. Grimes, *J. Phys. D-Appl. Phys.* **2006**, *39*, 2498–2503.
[201] S. Q. Li, G. M. Zhang, D. Z. Guo, L. G. Yu, W. Zhang, *J. Phys. Chem. C* **2009**, *113*, 12759–12765.
[202] J. Wang, L. Zhao, V. S. Y. Lin, Z. Q. Lin, *J. Mater. Chem.* **2009**, *19*, 3682–3687.
[203] G. S. Chen, C. C. Lee, H. Niu, W. Huang, R. Jann, T. Schutte, *Thin Solid Films* **2008**, *516*, 8473–8478.
[204] M. A. Afifi, M. M. Abdel-Aziz, I. S. Yahia, M. Fadel, L. A. Wahab, *J. Alloys Compd.* **2008**, *455*, 92–97.
[205] L. Y. Zheng, *Sens. Actuators B* **2003**, *88*, 115–119.
[206] T. Ioroi, H. Senoh, S. I. Yamazaki, Z. Siroma, N. Fujiwara, K. Yasuda, *J. Electrochem. Soc.* **2008**, *155*, B321-B326.
[207] Y. Wang, Y. Qin, G. C. Li, Z. L. Cui, Z. K. Zhang, *J. Cryst. Growth* **2005**, *282*, 402–406.
[208] J. Piekoszewski, A. Krajewski, F. Prokert, J. Senkara, J. Stanislawski, L. Walis, Z. Werner, W. Wlosinski, *Vacuum* **2003**, *70*, 307–312.
[209] A. Wolcott, W. A. Smith, T. R. Kuykendall, Y. P. Zhao, J. Z. Zhang, *Small* **2009**, *5*, 104–111.
[210] M. H. Seo, M. Yuasa, T. Kida, J. S. Huh, K. Shimanoe, N. Yamazoe, *Sens. Actuators B* **2009**, *137*, 513–520.
[211] A. Ghicov, H. Tsuchiya, R. Hahn, J. M. Macak, A. G. Munoz, P. Schmuki, *Electrochem. Commun.* **2006**, *8*, 528–532.
[212] S. Berger, A. Ghicov, Y. C. Nah, P. Schmuki, *Langmuir* **2009**, *25*, 4841–4844.
[213] Y. Lan, X. P. Gao, H. Y. Zhu, Z. F. Zheng, T. Y. Yan, F. Wu, S. P. Ringer, D. Y. Song, *Adv. Funct. Mater.* **2005**, *15*, 1310–1318.
[214] Z. Y. Yuan, B. L. Su, *Colloid Surf. A* **2004**, *241*, 173–183.
[215] D. Wu, J. Liu, X. N. Zhao, A. D. Li, Y. F. Chen, N. B. Ming, *Chem. Mater.* **2006**, *18*, 547–553.
[216] S. Iijima, *Nature* **1991**, *354*, 56–58.
[217] S. A. Needham, G. X. Wang, H. K. Liu, *J. Power Sources* **2006**, *159*, 254–257.
[218] H. Pang, Q. Lu, Y. Lia, F. Gao, *Chem. Commun.* **2009**, 7542–7544.
[219] Y. Ren, W. K. Chim, S. Y. Chiam, J. Q. Huang, C. Pi, J. S. Pan, *Adv. Funct. Mater.* **2010**, *20*, 3336–3342.
[220] T. Kavitha, H. Yuvaraj, *J. Mater. Chem.* **2011**, *21*, 15686–15691.
[221] B. Liu, H. Q. Yang, H. Zhao, L. J. An, L. H. Zhang, R. Y. Shi, L. Wang, L. Bao, Y. Chen, *Sens. Actuators B* **2011**, *156*, 251–262.
[222] L. Croguennec, C. Pouillerie, C. Delmas, *J. Electrochem. Soc.* **2000**, *147*, 1314–1321.
[223] H. B. Ji, T. T. Wang, M. Y. Zhang, Y. B. She, L. F. Wang, *Appl. Catal. A* **2005**, *282*, 25–30.
[224] W. Zhao, W. H. Ma, C. C. Chen, J. C. Zhao, Z. G. Shuai, *J. Am. Chem. Soc.* **2004**, *126*, 4782–4783.
[225] B. Sasi, K. G. Gopchandran, *Nanotechnology* **2007**, *18*, 115613.
[226] Z. J. Zhang, Y. Zhao, M. M. Zhu, *Appl. Phys. Lett.* **2006**, *88*, 033101.
[227] C. S. Shi, G. Q. Wang, N. Q. Zhao, X. W. Du, J. J. Li, *Chem. Phys. Lett.* **2008**, *454*, 75–79.
[228] S. I. Kim, J. H. Lee, Y. W. Chang, S. S. Hwang, K. H. Yoo, *Appl. Phys. Lett.* **2008**, *93*, 033503.
[229] H. Pang, Q. Lu, Y. Zhang, Y. Li, F. Gao, *Nanoscale* **2010**, *2*, 920–922.
[230] S. Xiong, C. Yuan, X. Zhang, Y. Qian, *CrystEngComm* **2011**, *13*, 626–636.
[231] Z. P. Wei, M. Arredondo, H. Y. Peng, Z. Zhang, D. L. Guo, G. Z. Xing, Y. F. Li, L. M. Wong, S. J. Wang, N. Valanoor, T. Wu, *ACS Nano* **2010**, *4*, 4785–4791.
[232] H. Y. Guan, C. L. Shao, S. B. Wen, B. Chen, J. Gong, X. H. Yang, *Inorg. Chem. Commun.* **2003**, *6*, 1302–1303.
[233] T. Kong, Y. Chen, Y. P. Ye, K. Zhang, Z. X. Wang, X. P. Wang, *Sens. Actuators B* **2009**, *138*, 344–350.
[234] A. Umar, *Nanoscale Res. Lett.* **2009**, *4*, 1004–1008.
[235] D. W. Chu, Y. Masuda, T. Ohji, K. Kato, *Langmuir* **2010**, *26*, 2811–2815.
[236] S. Lindroos, M. Leskela, *Int. J. Inorg. Mater.* **2000**, *2*, 197–201.
[237] C. C. Hsu, N. L. Wu, *J. Photochem. Photobiol. A* **2005**, *172*, 269–274.
[238] M. Sun, W. C. Hao, C. Z. Wang, T. M. Wang, *Chem. Phys. Lett.* **2007**, *443*, 342–346.
[239] M. A. Zimmler, T. Voss, C. Ronning, F. Capasso, *Appl. Phys. Lett.* **2009**, *94*, 241120.
[240] O. Lupan, T. Pauporte, T. Le Bahers, B. Viana, I. Ciofini, *Adv. Funct. Mater.* **2011**, *21*, 3564–3572.
[241] C. S. Rout, S. H. Krishna, S. R. C. Vivekchand, A. Govindaraj, C. N. R. Rao, *Chem. Phys. Lett.* **2006**, *418*, 586–590.
[242] L. Vayssieres, *Adv. Mater.* **2003**, *15*, 464–466.
[243] M. H. Huang, S. Mao, H. Feick, H. Q. Yan, Y. Y. Wu, H. Kind, E. Weber, R. Russo, P. D. Yang, *Science* **2001**, *292*, 1897–1899.
[244] P. D. Yang, H. Q. Yan, S. Mao, R. Russo, J. Johnson, R. Saykally, N. Morris, J. Pham, R. R. He, H. J. Choi, *Adv. Funct. Mater.* **2002**, *12*, 323–331.
[245] G. Z. Shen, Y. Bando, B. D. Liu, D. Golberg, C. J. Lee, *Adv. Funct. Mater.* **2006**, *16*, 410–416.
[246] U. K. Gautam, L. S. Panchakarla, B. Dierre, X. S. Fang, Y. Bando, T. Sekiguchi, A. Govindaraj, D. Golberg, C. N. R. Rao, *Adv. Funct. Mater.* **2009**, *19*, 131–140.
[247] A. Wei, X. W. Sun, C. X. Xu, Z. L. Dong, M. B. Yu, W. Huang, *Appl. Phys. Lett.* **2006**, *88*, 213102.
[248] N. Wang, X. Cao, L. Guo, *J. Phys. Chem. C* **2008**, *112*, 12616–12622.
[249] Y. K. Tseng, C. J. Huang, H. M. Cheng, I. N. Lin, K. S. Liu, I. C. Chen, *Adv. Funct. Mater.* **2003**, *13*, 811–814.
[250] Y. H. Leung, A. B. Djurisic, J. Gao, M. H. Xie, Z. F. Wei, S. J. Xu, W. K. Chan, *Chem. Phys. Lett.* **2004**, *394*, 452–457.
[251] U. Manzoor, D. K. Kim, *Script Mater.* **2006**, *54*, 807–811.
[252] P. X. Gao, Y. Ding, W. J. Mai, W. L. Hughes, C. S. Lao, Z. L. Wang, *Science* **2005**, *309*, 1700–1704.
[253] C. X. Xu, X. W. Sun, *Appl. Phys. Lett.* **2003**, *83*, 3806–3808.
[254] Y. W. Zhu, H. Z. Zhang, X. C. Sun, S. Q. Feng, J. Xu, Q. Zhao, B. Xiang, R. M. Wang, D. P. Yu, *Appl. Phys. Lett.* **2003**, *83*, 144–146.

[255] Y. F. Qiu, D. F. Liu, J. H. Yang, S. H. Yang, *Adv. Mater.* **2006**, *18*, 2604–2608.
[256] L. Kumari, J.-H. Lin, Y.-R. Ma, *J. Phys. D-Appl. Phys.* **2008**, *41*, 025405.
[257] A. S. Prakash, C. Shivakumara, M. S. Hegde, L. Dupont, J. M. Tarascon, *Mater. Res. Bull.* **2007**, *42*, 707–712.
[258] A. Hameed, T. Montini, V. Gombac, P. Fornasiero, *J. Am. Chem. Soc.* **2008**, *130*, 9658–9659.
[259] G. L. Fang, G. Chen, J. Q. Liu, X. Wang, *J. Phys. Chem. C* **2010**, *114*, 864–867.
[260] F. L. Zheng, G. R. Li, Y. N. Ou, Z. L. Wang, C. Y. Su, Y. X. Tong, *Chem. Commun.* **2010**, *46*, 5021–5023.
[261] B. J. Yang, M. S. Mo, H. M. Hu, C. Li, X. G. Yang, Q. W. Li, Y. T. Qian, *Eur. J. Inorg. Chem.* **2004**, 1785–1787.
[262] L. Li, Y. W. Yang, G. H. Li, L. D. Zhang, *Small* **2006**, *2*, 548–553.
[263] L. Li, Y. W. Yang, X. H. Huang, G. H. Li, R. Ang, L. D. Zhang, *Appl. Phys. Lett.* **2006**, *88*, 103119.
[264] D. C. Yang, G. W. Meng, Q. L. Xu, F. M. Han, M. G. Kong, L. D. Zhang, *J. Phys. Chem. C* **2008**, *112*, 8614–8616.
[265] J. W. Wang, X. Wang, C. Peng, Y. D. Li, *Inorg. Chem.* **2004**, *43*, 7552–7556.
[266] L. Liu, J. Jiang, S. M. Jin, Z. M. Xia, M. T. Tang, *CrystEngComm* **2011**, *13*, 2529–2532.
[267] Y. K. Liu, C. L. Zheng, W. Z. Wang, C. R. Yin, G. H. Wang, *Adv. Mater.* **2001**, *13*, 1883–1887.
[268] J. H. Duan, S. G. Yang, H. W. Liu, J. F. Gong, H. B. Huang, X. N. Zhao, R. Zhang, Y. W. Du, *J. Am. Chem. Soc.* **2005**, *127*, 6180–6181.
[269] Y. Wang, J. Y. Lee, H. C. Zeng, *Chem. Mater.* **2005**, *17*, 3899–3903.
[270] M. S. Park, G. X. Wang, Y. M. Kang, D. Wexler, S. X. Dou, H. K. Liu, *Angew. Chem. Int. Ed.* **2007**, *46*, 750–753.
[271] R. Chen, G. Z. Xing, J. Gao, Z. Zhang, T. Wu, H. D. Sun, *Appl. Phys. Lett.* **2009**, *95*, 061908.
[272] Z. R. Dai, Z. W. Pan, Z. L. Wang, *J. Am. Chem. Soc.* **2002**, *124*, 8673–8680.
[273] S. Wang, S. H. Xie, H. X. Li, S. R. Yan, K. N. Fan, M. H. Qiao, *Chem. Commun.* **2005**, 507–509.
[274] H. Uchiyama, H. Ohgi, H. Imai, *Cryst. Growth Des.* **2006**, *6*, 2186–2190.
[275] A. Martel, F. Caballero-Briones, R. Bartolo-Perez, A. Iribarren, R. Castro-Rodriguez, A. Zapata-Navarro, J. L. Pena, *Surf. Coat. Technol.* **2001**, *148*, 103–109.
[276] J. H. He, T. H. Wu, C. L. Hsin, K. M. Li, L. J. Chen, Y. L. Chueh, L. J. Chou, Z. L. Wang, *Small* **2006**, *2*, 116–120.
[277] Y. J. Chen, X. Y. Xue, Y. G. Wang, T. H. Wang, *Appl. Phys. Lett.* **2005**, *87*, 233503.
[278] D. F. Zhang, L. D. Sun, J. L. Yin, C. H. Yan, *Adv. Mater.* **2003**, *15*, 1022–1025.
[279] Z. Q. Liu, D. H. Zhang, S. Han, C. Li, T. Tang, W. Jin, X. L. Liu, B. Lei, C. W. Zhou, *Adv. Mater.* **2003**, *15*, 1754–1757.
[280] J. H. Duan, J. F. Gong, H. B. Huang, X. N. Zhao, G. X. Cheng, Z. Z. Yu, S. G. Yang, *Nanotechnology* **2007**, *18*, 055607.
[281] M. S. Arnold, P. Avouris, Z. W. Pan, Z. L. Wang, *J. Phys. Chem. B* **2003**, *107*, 659–663.
[282] J. Q. Hu, Y. Bando, Q. L. Liu, D. Golberg, *Adv. Funct. Mater.* **2003**, *13*, 493–496.
[283] R. J. Zou, J. Q. Hu, Z. Y. Zhang, Z. G. Chen, M. Y. Liao, *CrystEngComm* **2011**, *13*, 2289–2293.
[284] Z. R. Dai, J. L. Gole, J. D. Stout, Z. L. Wang, *J. Phys. Chem. B* **2002**, *106*, 1274–1279.
[285] C. S. Rout, A. Govindaraj, C. N. R. Rao, *J. Mater. Chem.* **2006**, *16*, 3936–3941.
[286] J. M. Baik, M. H. Kim, C. Larson, C. T. Yavuz, G. D. Stucky, A. M. Wodtke, M. Moskovits, *Nano Lett.* **2009**, *9*, 3980–3984.
[287] Q. Wan, Q. H. Li, Y. J. Chen, T. H. Wang, X. L. He, J. P. Li, C. L. Lin, *Appl. Phys. Lett.* **2004**, *84*, 3654–3656.
[288] D. Zhang, Z. Liu, C. Li, T. Tang, X. Liu, S. Han, B. Lei, C. Zhou, *Nano Lett.* **2004**, *4*, 1919–1924.
[289] O. Lupan, G. Chai, L. Chow, *Microelectron. Eng.* **2008**, *85*, 2220–2225.
[290] T. J. Hsueh, S. J. Chang, C. L. Hsu, Y. R. Lin, I. C. Chen, *J. Electrochem. Soc.* **2008**, *155*, K152-K155.
[291] L. Liao, H. B. Lu, J. C. Li, H. He, D. F. Wang, D. J. Fu, C. Liu, W. F. Zhang, *J. Phys. Chem. C* **2007**, *111*, 1900–1903.
[292] J. D. Prades, R. Jimenez-Diaz, F. Hernandez-Ramirez, S. Barth, A. Cirera, A. Romano-Rodriguez, S. Mathur, J. R. Morante, *Appl. Phys. Lett.* **2008**, *93*, 123110.
[293] J. Polleux, A. Gurlo, N. Barsan, U. Weimar, M. Antonietti, M. Niederberger, *Angew. Chem. Int. Ed.* **2006**, *45*, 261–265.
[294] E. Comini, G. Faglia, G. Sberveglieri, Z. Pan, Z. L. Wang, *Appl. Phys. Lett.* **2002**, *81*, 1869–1871.
[295] O. Lupan, V. V. Ursaki, G. Chai, L. Chow, G. A. Emelchenko, I. M. Tiginyanu, A. N. Gruzintsev, A. N. Redkin, *Sens. Actuators B* **2010**, *144*, 56–66.
[296] J. X. Wang, X. W. Sun, Y. Yang, H. Huang, Y. C. Lee, O. K. Tan, L. Vayssieres, *Nanotechnology* **2006**, *17*, 4995–4998.
[297] Y. J. Chen, L. Nie, X. Y. Xue, Y. G. Wang, T. H. Wang, *Appl. Phys. Lett.* **2006**, *88*, 083105.
[298] Y. S. Kim, S.-C. Ha, K. Kim, H. Yang, S.-Y. Choi, Y. T. Kim, J. T. Park, C. H. Lee, J. Choi, J. Paek, K. Lee, *Appl. Phys. Lett.* **2005**, *86*, 213105.
[299] Q. Kuang, C. S. Lao, Z. L. Wang, Z. X. Xie, L. S. Zheng, *J. Am. Chem. Soc.* **2007**, *129*, 6070–6071.
[300] H. T. Wang, B. S. Kang, F. Ren, L. C. Tien, P. W. Sadik, D. P. Norton, S. J. Pearton, J. Lin, *Appl. Phys. Lett.* **2005**, *86*, 243503.
[301] J. M. Wang, E. Khoo, P. S. Lee, J. Ma, *J. Phys. Chem. C* **2009**, *113*, 9655–9658.
[302] H. S. Shim, J. W. Kim, Y. E. Sung, W. B. Kim, *Sol. Energy Mater. Sol. Cells* **2009**, *93*, 2062–2068.
[303] K. K. Purushothaman, G. Muralidharan, *Sol. Energy Mater. Sol. Cells* **2009**, *93*, 1195–1201.
[304] L. Zheng, Y. Xu, D. Jin, Y. Xie, *Chem. Mater.* **2009**, *21*, 5681–5690.
[305] C. R. Xiong, A. E. Aliev, B. Gnade, K. J. Balkus, *ACS Nano* **2008**, *2*, 293–301.
[306] K. C. Cheng, F. R. Chen, J. J. Kai, *Sol. Energy Mater. Sol. Cells* **2006**, *90*, 1156–1165.
[307] A. Ghicov, S. P. Alba, J. M. Macak, P. Schmuki, *Small* **2008**, *4*, 1063–1066.
[308] S.-H. Lee, R. Deshpande, P. A. Parilla, K. M. Jones, B. To, A. H. Mahan, A. C. Dillon, *Adv. Mater.* **2006**, *18*, 763–766.
[309] S. R. Bathe, and P. S. Patil, *J. Phys. D: Appl. Phys.* **2007**, *40*, 7423–7431.
[310] J. M. Bao, M. A. Zimmler, F. Capasso, X. W. Wang, Z. F. Ren, *Nano Lett.* **2006**, *6*, 1719–1722.
[311] M. C. Jeong, B. Y. Oh, M. H. Ham, S. W. Lee, J. M. Myoung, *Small* **2007**, *3*, 568–572.
[312] S. H. Park, S. H. Kim, S. W. Han, *Nanotechnology* **2007**, *18*, 055608.
[313] J. Y. Wang, C. Y. Lee, Y. T. Chen, C. T. Chen, Y. L. Chen, C. F. Lin, Y. F. Chen, *Appl. Phys. Lett.* **2009**, *95*, 131117.
[314] O. Lupan, T. Pauporté, B. Viana, *Adv. Mater.* **2010**, *22*, 3298–3302.
[315] S. W. Lee, H. D. Cho, G. Panin, T. W. Kang, *Appl. Phys. Lett.* **2011**, *98*, 093110.
[316] Y. Y. Xi, Y. F. Hsu, A. B. Djurisic, A. M. C. Ng, W. K. Chan, H. L. Tam, K. W. Cheah, *Appl. Phys. Lett.* **2008**, *92*, 113505.
[317] R. Konenkamp, R. C. Word, C. Schlegel, *Appl. Phys. Lett.* **2004**, *85*, 6004–6006.

[318] R. Konenkamp, R. C. Word, M. Godinez, *Nano Lett.* **2005**, *5*, 2005–2008.
[319] X. W. Sun, J. Z. Huang, J. X. Wang, Z. Xu, *Nano Lett.* **2008**, *8*, 1219–1223.
[320] X. M. Zhang, M. Y. Lu, Y. Zhang, L. J. Chen, Z. L. Wang, *Adv. Mater.* **2009**, *21*, 2767–2770.
[321] S. Xu, C. Xu, Y. Liu, Y. F. Hu, R. S. Yang, Q. Yang, J. H. Ryou, H. J. Kim, Z. Lochner, S. Choi, R. Dupuis, Z. L. Wang, *Adv. Mater.* **2010**, *22*, 4749–4753.
[322] H. H. Guo, Z. H. Lin, Z. F. Feng, L. L. Lin, J. Z. Zhou, *J. Phys. Chem. C* **2009**, *113*, 12546–12550.
[323] C. H. Ahn, Y. Y. Kim, D. C. Kim, S. K. Mohanta, H. K. Cho, *J. Appl. Phys.* **2009**, *105*, 013502–013505.
[324] Y. R. Ryu, T. S. Lee, J. A. Lubguban, H. W. White, Y. S. Park, C. J. Youn, *Appl. Phys. Lett.* **2005**, *87*, 153504.
[325] D. J. Rogers and F. H. Teherani, A. Yasan, K. Minder, P. Kung, M. Razeghi, *Appl. Phys. Lett.* **2006**, *88*, 141918.
[326] Q. Zhao, H. Z. Zhang, Y. W. Zhu, S. Q. Feng, X. C. Sun, J. Xu, D. P. Yu, *Appl. Phys. Lett.* **2005**, *86*, 203115.
[327] J. C. She, Z. M. Xiao, Y. H. Yang, S. Z. Deng, J. Chen, G. W. Yang, N. S. Xu, *ACS Nano* **2008**, *2*, 2015–2022.
[328] C. W. Zhou, L. Q. Mai, Y. L. Liu, Y. Y. Qi, Y. Dai, W. Chen, *J. Phys. Chem. C* **2007**, *111*, 8202–8205.
[329] W. Chen, C. W. Zhou, L. Q. Mai, Y. L. Liu, Y. Y. Qi, Y. Dai, *J. Phys. Chem. C* **2008**, *112*, 2262–2265.
[330] J. G. Liu, Z. J. Zhang, Y. Zhao, X. Su, S. Liu, E. G. Wang, *Small* **2005**, *1*, 310–313.
[331] J. M. Wu, H. C. Shih, W. T. Wu, *Chem. Phys. Lett.* **2005**, *413*, 490–494.
[332] M. Miyauchi, H. Tokudome, Y. Toda, T. Kamiya, H. Hosono, *Appl. Phys. Lett.* **2006**, *89*, 043114.
[333] L. A. Ma, T. L. Guo, *Physica B* **2008**, *403*, 3410–3413.
[334] J. Wu, K. Yu, L. J. Li, J. W. Xu, D. J. Shang, Y. E. Xu, Z. Q. Zhu, *J. Phys. D: Appl. Phys.* **2008**, *41*, 185302.
[335] Y. B. Li, Y. Bando, D. Golberg, K. Kurashima, *Appl. Phys. Lett.* **2002**, *81*, 5048–5050.
[336] J. Zhou, S. Z. Deng, N. S. Xu, J. Chen, J. C. She, *Appl. Phys. Lett.* **2003**, *83*, 2653–2655.
[337] J. G. Liu, Z. J. Zhang, C. Y. Pan, Y. Zhao, X. Su, Y. Zhou, D. P. Yu, *Mater. Lett.* **2004**, *58*, 3812–3815.
[338] X. Wang, J. Zhou, C. Lao, J. Song, N. Xu, Z. L. Wang, *Adv. Mater.* **2007**, *19*, 1627–1631.
[339] S. Yue, H. Pan, Z. Ning, J. Yin, Z. Wang, G. Zhang, *Nanotechnology* **2011**, *22*, 115703.
[340] Y. G. Wang, X. G. Zhang, *J. Electrochem. Soc.* **2005**, *152*, A671-A676.
[341] J. Xu, L. Gao, J. Y. Cao, W. C. Wang, Z. D. Chen, *J. Solid State Electrochem.* **2011**, *15*, 2005–2011.
[342] G. Wee, H. Z. Soh, Y. L. Cheah, S. G. Mhaisalkar, M. Srinivasan, *J. Mater. Chem.* **2010**, *20*, 6720–6725.
[343] Q. T. Qu, Y. Shi, L. L. Li, W. L. Guo, Y. P. Wu, H. P. Zhang, S. Y. Guan, R. Holze, *Electrochem. Commun.* **2009**, *11*, 1325–1328.
[344] Y. Yang, D. Kim, M. Yang, P. Schmuki, *Chem. Commun.* **2011**, *47*, 7746–7748.
[345] Y. G. Wang, X. G. Zhang, *Electrochim. Acta* **2004**, *49*, 1957–1962.
[346] M. Salari, S. H. Aboutalebi, K. Konstantinov, H. K. Liu, *Phys. Chem. Chem. Phys.* **2011**, *13*, 5038–5041.
[347] K. Y. Xie, J. Li, Y. Q. Lai, Z. A. Zhang, Y. X. Liu, G. G. Zhang, H. T. Huang, *Nanoscale* **2011**, *3*, 2202–2207.
[348] J. A. Yan, E. Khoo, A. Sumboja, P. S. Lee, *ACS Nano* **2010**, *4*, 4247–4255.
[349] W. T. Jiang, J. A. Ni, K. Yu, Z. Q. Zhu, *Appl. Surf. Sci.* **2011**, *257*, 3253–3258.
[350] J. A. Yan, A. Sumboja, E. Khoo, P. S. Lee, *Adv. Mater.* **2011**, *23*, 746–750.
[351] Q. Wang, Z. H. Wen, J. H. Li, *Adv. Funct. Mater.* **2006**, *16*, 2141–2146.
[352] J. Lee, J. Choi, S. K. Choi, H. D. Chun, *Nanotechnology* **2005**, *16*, 1449–1453.
[353] G. R. Li, Z. L. Wang, F. L. Zheng, Y. N. Ou, Y. X. Tong, *J. Mater. Chem.* **2011**, *21*, 4217–4221.
[354] L. Zheng, Y. Xu, D. Jin, Y. Xie, *J. Mater. Chem.* **2010**, *20*, 7135–7143.
[355] C. S. Rout, G. U. Kulkarni, C. N. R. Rao, *J. Nanosci. Nanotechnol.* **2009**, *9*, 5652–5658.
[356] L. Li, Y. Zhang, X. S. Fang, T. Y. Zhai, M. Y. Liao, X. L. Sun, Y. Koide, Y. Bando, D. Golberg, *J. Mater. Chem.* **2011**, *21*, 6525–6530.
[357] E. N. Dattoli, Q. Wan, W. Guo, Y. B. Chen, X. Q. Pan, W. Lu, *Nano Lett.* **2007**, *7*, 2463–2469.
[358] Y. X. Hong, W. Kuo, K. J. Lin, *Nanotechnology* **2011**, *22*, 115501.
[359] S. M. Peng, Y. K. Su, L. W. Ji, S. J. Young, C. N. Tsai, W. C. Chao, Z. S. Chen, C. Z. Wu, *IEEE Electron Device Lett.* **2011**, *32*, 533–535.
[360] J. Goldberger, D. J. Sirbuly, M. Law, P. Yang, *J. Phys. Chem. B* **2005**, *109*, 9–14.
[361] S. N. Cha, J. E. Jang, Y. Choi, G. A. J. Amaratunga, G. W. Ho, M. E. Welland, D. G. Hasko, D. J. Kang, J. M. Kim, *Appl. Phys. Lett.* **2006**, *89*, 263102.
[362] K. Keem, D. Y. Jeong, S. Kim, M. S. Lee, I. S. Yeo, U. I. Chung, J. T. Moon, *Nano Lett.* **2006**, *6*, 1454–1458.
[363] Y.-F. Lin, W.-B. Jian, *Nano Lett.* **2008**, *8*, 3146–3150.
[364] D. Kaelblein, R. T. Weitz, H. J. Bottcher, F. Ante, U. Zschieschang, K. Kern, H. Klauk, *Nano Lett.* **2011**, *11*, 5309–5315.
[365] D. Yeom, K. Keem, J. Kang, D. Y. Jeong, C. Yoon, D. Kim, S. Kim, *Nanotechnology* **2008**, *19*, 265202.
[366] G. Jo, W. K. Hong, J. I. Sohn, M. Jo, J. Shin, M. E. Welland, H. Hwang, K. E. Geckeler, T. Lee, *Adv. Mater.* **2009**, *21*, 2156–2160.
[367] G. Jo, W. K. Hong, J. Maeng, M. Choe, W. Park, T. Lee, *Appl. Phys. Lett.* **2009**, *94*, 173118.
[368] Y. T. Lee, S. Im, R. Ha, H. J. Choi, *Appl. Phys. Lett.* **2010**, *97*, 123506.
[369] K. Sun, J. J. Qi, Q. Zhang, Y. Yang, Y. Zhang, *Nanoscale* **2011**, *3*, 2166–2168.
[370] X. D. Wang, J. H. Song, J. Liu, Z. L. Wang, *Science* **2007**, *316*, 102–105.
[371] P. X. Gao, J. H. Song, J. Liu, Z. L. Wang, *Adv. Mater.* **2007**, *19*, 67–72.
[372] Y. Xi, J. H. Song, S. Xu, R. S. Yang, Z. Y. Gao, C. G. Hu, Z. L. Wang, *J. Mater. Chem.* **2009**, *19*, 9260–9264.
[373] M. P. Lu, J. Song, M. Y. Lu, M. T. Chen, Y. Gao, L. J. Chen, Z. L. Wang, *Nano Lett.* **2009**, *9*, 1223–1227.
[374] R. Yang, Y. Qin, C. Li, G. Zhu, Z. L. Wang, *Nano Lett.* **2009**, *9*, 1201–1205.
[375] R. S. Yang, Y. Qin, L. M. Dai, Z. L. Wang, *Nat. Nanotechnol.* **2009**, *4*, 34–39.
[376] J. Liu, P. Fei, J. Zhou, R. Tummala, Z. L. Wang, *Appl. Phys. Lett.* **2008**, *92*, 173105.
[377] S. Xu, Y. Qin, C. Xu, Y. G. Wei, R. S. Yang, Z. L. Wang, *Nat. Nanotechnol.* **2010**, *5*, 366–373.
[378] G. A. Zhu, R. S. Yang, S. H. Wang, Z. L. Wang, *Nano Lett.* **2010**, *10*, 3151–3155.
[379] Y. F. Hu, L. Lin, Y. Zhang, Z. L. Wang, *Adv. Mater.* **2012**, *24*, 110–114.
[380] Y. Qin, X. D. Wang, Z. L. Wang, *Nature* **2008**, *451*, 809–813.
[381] C. Y. Chen, J. H. Huang, J. H. Song, Y. S. Zhou, L. Lin, P. C. Huang, Y. Zhang, C. P. Liu, J. H. He, Z. L. Wang, *ACS Nano* **2011**, *5*, 6707–6713.